A Kinetic and Spectroscopic Analysis of Distance-dependent Singlet Fission in TIPS-Pentacene

Alexandra N. Stuart

B.Sc. (Advanced)

A thesis submitted in partial fulfilment of the requirements for the degree of Master of Philosophy (Chemical Science)

October 2017

Department of Chemistry
The University of Adelaide
North Terrace Campus
Adelaide, South Australia 5005

Contents

Abstract

Singlet exciton fission (SF) is a process with the potential to extend the maximum theoretical efficiency of solar cells from 34% to 46%. By generating two triplet excitons from one singlet exciton, the process effectively splits the energy of a high-energy photon in two, reducing efficiency loss by thermal relaxation. While the process has a strong theoretical grounding, the mechanistic details of SF and practicalities of implementation in photovoltaic devices are insufficiently understood to exploit its full potential. In this thesis the effect of intermolecular distance on SF is studied by embedding 6,13-bis(triisopropylsilylethynyl) pentacene (TIPS-pentacene) in an amorphous polymer matrix in the form of aqueous nanoparticle dispersions. By varying the mass ratio of TIPS-pentacene to the host polymer, the average intermolecular separation between TIPS-pentacene molecules is varied systematically from approximately 1 to 5 nm, resulting in a range of SF quantum yields. We study this system using both steady-state and ultrafast time-resolved spectroscopic techniques, and fit the results to a kinetic model to decipher the observed behaviour. The quantum yield of SF is shown to decrease with intermolecular separation, which is explained by diffusion-limited SF and an increase in loss pathways through exciton trap sites. We additionally identify an intermediate species in the SF process, and show that a significant proportion of this species decays non-radiatively without dissociating to form separated triplets, revealing another major loss pathway that has important implications for future research and applications.

Declaration

I certify that this work contains no material which has been accepted for the award of any other degree or diploma in my name in any university or other tertiary institution and, to the best of my knowledge and belief, contains no material previously published or written by another person, except where due reference has been made in the text. In addition, I certify that no part of this work will, in the future, be used in a submission in my name for any other degree or diploma in any university or other tertiary institution without the prior approval of the University of Adelaide and where applicable, any partner institution responsible for the joint award of this degree.

I give consent to this copy of my thesis when deposited in the University Library, being made available for loan and photocopying, subject to the provisions of the Copyright Act 1968.

The author acknowledges that copyright of published works contained within this thesis resides with the copyright holder(s) of those works.

I also give permission for the digital version of my thesis to be made available on the web, via the University's digital research repository, the Library Search and also through web search engines, unless permission has been granted by the University to restrict access for a period of time.

Alexandra N. Stuart
October 2017

Acknowledgements

An overwhelming amount of people have helped me over the last one and a half years of my master's degree. Firstly, I am incredibly grateful to my supervisors Assoc. Prof. Tak W. Kee and Assoc. Prof. David M. Huang for their knowledge, understanding and patience. I have been granted a great deal of flexibility with my projects and many opportunities to travel and learn new skills, for all of which I am extremely appreciative.

The work in this thesis was also carried out with Dr. Patrick Tapping, whose skills and knowledge, and tolerance of my constant stream of questions has been invaluable. I have to especially acknowledge the handy LaTeX template, the TA heat plots, and all the assistance with data collection and analysis.

Lynette Waterhouse and Animesh Basak from Adelaide Microscopy provided useful assistance with SEM images, and the Sumby/Doonan/Keene group also deserve thanks for the continuous supply of distilled THF. Matthew Bull must also be acknowledged for letting me invade the teaching labs and helping with a number of problems I encountered.

A large part of the work I conducted in my masters did not make it into this thesis, but I am equally appreciative of the help I received on these projects as well. Thanks to Dr. Pejman Talemi and students in particular for helping me with DLS measurements and the polymer film coating for my OLEDs.

Thank you to both the Kee and Huang group members, past and present. Specifically, Ras Roseli for keeping me company last year, and Elisabeth Schrefl for her motivation and encouragement this year, and also for cleaning my glassware.

To my family, thank you for always being understanding and supportive, and to my dogs, Rosey and Odie: you are very good dogs.

Finally, to anyone else who has helped me over the last few years, whether through buying me food, sending me papers or theses, swapping demonstrating sessions at the last minute or just offering general words of encouragement and advice: thank you, it is very much appreciated.

Abbreviations

BBO β-barium borate

CT charge transfer

ESA excited-state absorption

FWHM full width half maximum

GSB ground-state bleach

IRF instrument response function

NP nanoparticle

OPA optical parametric amplifier

PMMA poly(methyl methacrylate)

Pn pentacene

PV photovoltaic

SE stimulated emission

SEM scanning electron microscopy

SF singlet fission

SFG sum frequency generation

SQ Shockley-Queisser

TA transient absorption

TCSPC time-correlated single photon counting

THF tetrohydrofuran

TIPS triisopropylsilylethnyl

TIPS-Pn 6,13-bis(triisopropylsilylethynyl) pentacene

TTA triplet-triplet annihilation

UC upconversion

List of Figures

List of Tables

CHAPTER 1
Introduction

1.1 Solar Photovoltaics

In the last 40 years, global energy consumption has more than doubled; an expansion which, for the most part, has been supported by fossil fuels.[1] In 1973, 87% of energy consumption was provided by fossil fuels, including coal, natural gas and oil. Today they are still the dominant source of energy, accounting for around 81% of global use in 2015,[1] and 86% in Australia.[2] While the cheap and reliable nature of fossil fuels has allowed them to support the world's growing energy needs until now, it is becoming more evident that their use has significant consequences. Most notably, the combustion of fossil fuels releases carbon dioxide, which is widely regarded as the leading source of climate change.[3,4] In addition to this, fossil fuels are a finite, non-renewable source. It has been predicted that within 50 years, the economically recoverable reserves of both oil and natural gas will have been depleted, and in a century coal as well.[5] Within this same time, global energy consumption is expected to double.[6] It is clear that to minimise the effects of climate change, and fill the void left by fossil fuels, cleaner, preferably renewable sources of energy are required. Fortunately, as the consequences of fossil fuels have become more evident, new, renewable sources of energy have begun to emerge, one of the most promising of these being solar energy.

Enough sunlight hits the surface of the earth in a single hour to meet the worlds entire energy consumption in one year.[7] The energy provided by the sun in fact dwarfs all other potential sources combined, including fossil fuels, nuclear power, wind, and biofuels.[8,9] If even 0.1% of this energy is able to be effectively and economically harvested, projected global consumption demands could easily be met, eliminating fossil fuel dependence.

Solar photovoltaic cells, or solar cells, provide a means of harvesting this sunlight. By absorbing incident light from the sun, solar cells convert this light into electricity, producing zero emissions in the process. The most common types are single-junction solar cells, classed as "first-generation" cells, in which a single absorbing material (the active material) is used. Upon absorbing a photon, an excited electron is generated in the active material, which can be separated from the positively charged vacancy (or "hole") left behind and used to generate a current, or electricity. Single-junction solar cells with silicon as the active material are already becoming economically competitive with fossil fuels in some places.[10] But, despite their potential, solar cells contribute little to the current energy use.[1] Improvements in efficiency and cost of these devices are necessary to accelerate widespread adoption.

1.2 The Shockley-Queisser Limit

Single junction solar cells are limited to a maximum theoretical efficiency of around 33.7%. This means out of all the light from the sun incident on an ideal solar cell, only

33.7% can be converted into electricity. This is known as the Shockley-Queisser (SQ) limit, and was first presented in a seminal 1961 paper by Shockley and Queisser,[11] who calculated the maximum theoretical efficiency of a single junction solar cell for an active material with a range of different band gaps. The original paper found the maximum theoretical efficiency was 30% for band gap of 1.1 eV under the 6000 K blackbody spectrum, but recalculations with the air-mass 1.5 global spectrum have lead to the now widely accepted value of 33.7% for an optimum band gap of 1.34 eV, as shown in Figure 1.1.[12–15]

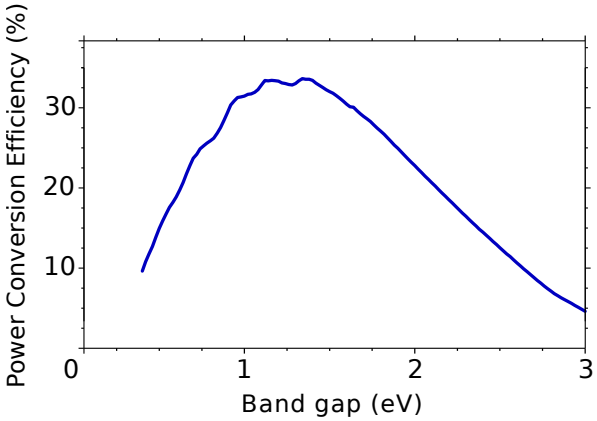

Figure 1.1: Shockley-Queisser limit of the maximum theoretical efficiency of solar cells for varying band gaps.[16]

The main losses of efficiency accounted for in the Shockley-Queisser (SQ) limit are explained in Figure 1.2. Out of all sunlight incident on a solar cell, a proportion of this will have an energy below the band gap of the active material. These low-energy photons are thus not absorbed, and are effectively wasted, causing a loss of ~31% efficiency for a band gap of 1.34 eV. The portion of light with energies above the band gap also contribute to the efficiency loss, as any excess energy above the band gap is lost as heat through thermalisation, or non-radiative decay. The energy lost as heat contributes a further ~23%. The remaining 13% loss comes from unavoidable radiative recombination of excited states (~1%), and thermodynamic loss (~12%).[13]

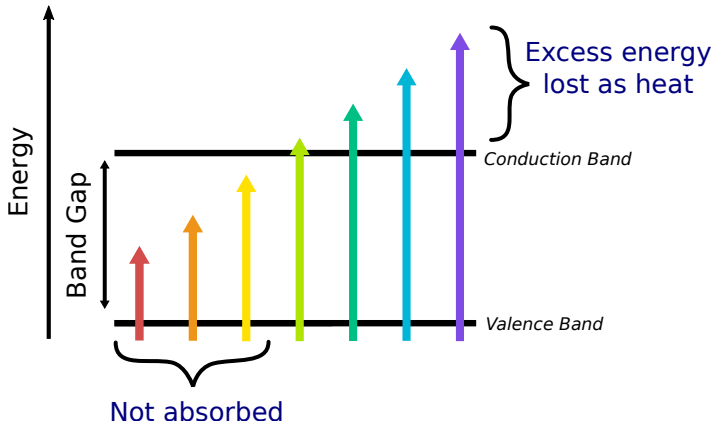

Figure 1.2: Shockley Queisser Limit. ~31% of efficiency is lost from lower energy photons not being absorbed, and ~23% from thermal relaxation of higher energy photons.

The first practical solar cells had efficiencies of around 6%.[17] Over the past 60 years the development of solar cell technologies has been an active area of research,

with conventional cells now approaching the SQ limit.[18] The highest efficiency to date for a single-junction solar cell is 28.8% for thin-film crystalline gallium-arsenic cells, and 25.6% for silicon heterostructures.[19] Though high efficiency is evidently possible for single junction, or first and second (thin film) generation photovoltaics, the cost needed to produce these high-performing cells is high, and there is room to improve solar cell efficiency even more.

While the improvement of conventional solar cells has increased over the years, new technologies have also emerged that have the potential to exceed the SQ limit. Among these "third generation" photovoltaics are tandem solar cells, which increase the range of light absorbed; hot carrier cells, which reduce energy loss due to thermalisation; and devices using molecular processes such as photon upconversion, downconversion, and singlet fission.[20]

1.3 Singlet Exciton Fission

Singlet exciton fission, or simply singlet fission (SF), is a spin-conserving process in which a chromophore in its first singlet excited state, S_1, shares its energy with a chromophore in the ground state, S_0, to give two triplet excitons, T_1, as illustrated in Figure 1.3. This is generally agreed to proceed through a correlated triplet-pair intermediate, $^1(TT)$, which is a coherently coupled pair of triplets with an overall singlet character,

$$S_0 + S_1 \rightleftharpoons {}^1(TT) \rightleftharpoons T_1 + T_1.$$

Because spin is conserved, SF is potentially much faster than triplet formation by intersystem crossing, and can also be distinguished by the formation of two triplets per singlet exciton, instead of one.[21]

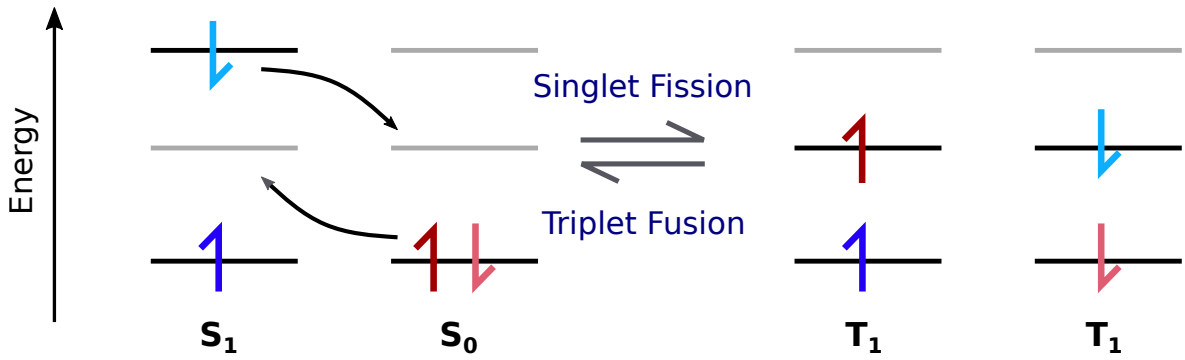

Figure 1.3: Singlet Fission of a ground state chromophore, S_0, and singlet exciton S_1 to give a pair triplets T_1. The reverse process is triplet fusion.

SF was first identified in crystalline anthracene by Singh and coworkers in 1965.[22] The reverse process, triplet fusion or triplet-triplet annihilation (TTA), in which two triplets combine to give an S_1 and S_0 state, has been widely studied over the last 50 years.[23–28] However, after its initial identification, SF had not been of significant interest until the last decade or so. The revival of research on SF is in part due to the suggestion by Nozik et al. of its potential ability to increase the efficiency of solar cells.[14,29,30]

Whereas the energy of photons in excess of the band gap of the absorbing material in conventional single junction solar cells is lost through thermal relaxation, SF could use these high-energy photons to generate two triplet excitons, each of which could be used for charge separation. This process is described in Figure 1.4.

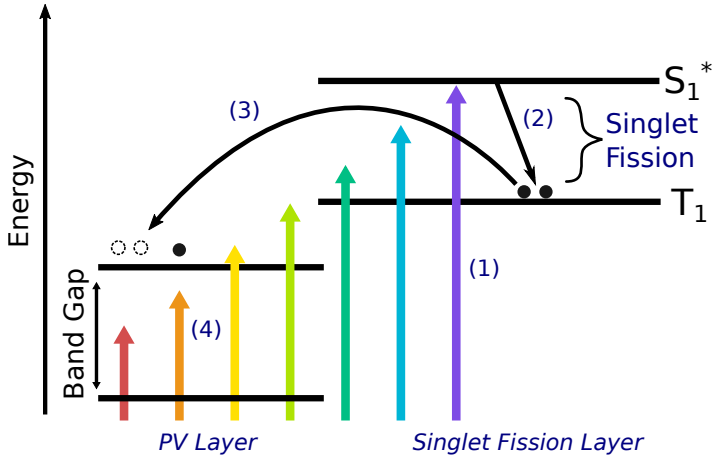

Figure 1.4: Singlet fission in solar cells. Ideally a lower band gap material (photovoltaic (PV) layer) would absorb lower energy photons (4), and a SF layer absorb the higher energy photons (1) converting them into 2 triplet excitons via SF (2). The energy of the triplet excitons can then be transferred to the PV layer (3).

The usual idea is that a material that undergoes SF is used in tandem with an electron acceptor of a lower energy band gap, such as a semiconductor like silicon (the photovoltaic or PV layer in Figure 1.4). The SF layer would absorb high-energy photons to generate the excited state S_1 (1). S_1 then shares its energy with a ground-state chromophore to give two lower energy T_1 states. Thus 2 excitations are generated from a single photon (2). If the energy of T_1 is greater than that of the conduction band of the PV layer, the excitations can be transferred to the acceptor and harvested for electricity (3). In this way the higher energy photons are not wasted, and since triplet energy is transferred into a lower band gap material, current is increased without compromising the voltage.[31,32] Additionally the lower energy photons that the SF layer does not absorb are transmitted through to the next material, so these can then be absorbed by the PV layer, or alternatively a second sensitizer layer (4).[16,31,33] It has been calculated that using SF the maximum theoretical efficiency of a single bandgap solar cell would be increased from 33.7 to ~46%, as shown in Figure 1.5.[15,33,34]

Despite this potential, the highest efficiencies of SF based solar cells so far have been less than 5%.[35–37] It is clear that a better understanding of the underlying mechanism of SF and how to best implement it in solar cells is required. Broadly, there are two fundamental issues to address: the ability to effectively transport and harvest the produced triplet excitons, and the efficiency of the SF process itself. This thesis primarily focuses on the latter.

1.3.1 Efficiency of Singlet Fission

The efficiency of SF can be quantified by the SF quantum yield. This is defined as the number of triplets excitons produced per singlet exciton,

$$\phi_{SF} = \frac{\max([T_1])}{\max([S_1])}, \tag{1.1}$$

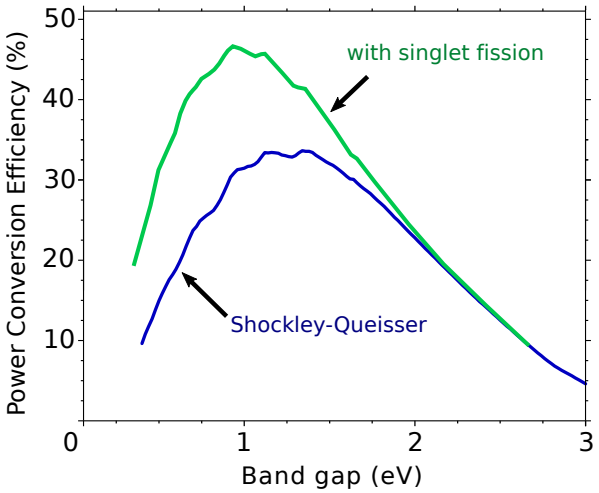

Figure 1.5: Increased maximum theoretical efficiency of solar cells when SF is used.[16]

where $[T_1]$ and $[S_1]$ are the concentrations of triplet and singlet excitons, respectively. When SF is completely efficient, two triplet excitons are produced for every singlet exciton, so the maximum ϕ_{SF} is 2. In practice the triplets eventually decay or annihilate, which reduces the yield. Ideally these processes should be slow compared with the rate of SF, such that the yield is still close to 2.

SF has been identified in a range of organic molecules, including acenes,[38–40] carotenoids,[41,42] diphenylisobenzofuran,[43] perylenediimide,[44] and diketopyrrolopyrrole.[45,46] However, just a few systems have been demonstrated to have high SF quantum yields;[42,43,47] in many others this is not the case. It is generally accepted that exothermic SF, in which the energy of the S_1 state is greater than or close to twice the energy of T_1, is one condition for efficient SF, but there are a range of other factors for which the effect on efficiency is less clear. The efficiency of SF has been shown to depend on a number of parameters, such as material, temperature, concentration, and morphology.[21,29] To effectively use SF in solar cells, a better understanding of the mechanism of SF and how each of these factors influence the process is needed.

1.3.2 Effect of Morphology

The morphology or arrangement of molecules in space can have a particularly profound impact on the efficiency of SF, and thus is an important property to consider in the design of materials for solar cells. Effects of morphology have been observed in a number of studies, both theoretical and experimental. For example, quantum dynamics and molecular dynamics simulations by Wang et al. found that the rate of SF can be increased by more than an order of magnitude by changing the intermolecular packing of pentacene dimers.[48] Though not strictly synonymous, a fast rate is typically associated with a high SF yield. Another computational study by Renaud et al. showed different packing geometries in crystals of perylenediimide derivatives led to SF quantum yields ranging from 1.34 down to 0. Two crystal structures from this study, in particular, only differed in their arrangements by a few tenths of an angstrom, yet one had a yield of 0.15 and in the other SF was suppressed entirely.[49] Observations of the sensitivity of SF to morphology are not just limited to crystalline systems. Amorphous films of diphenyl tetracene have been found to undergo diffusion-limited SF, in which excitons had to diffuse to specific "SF sites" in the film to undergo SF. This suggests that SF

in tetracene requires particular geometries or intermolecular separations.[50,51]

There is some dispute over whether SF is more efficient in crystalline or amorphous systems. The highest SF yields have mostly been reported for crystalline arrangements, but amorphous morphologies may still be favourable in that they can sample a higher number of different configurations between neighbouring chromophores, and therefore have a higher probability of forming sites that are favourable to SF, which may not be practical or possible in crystalline form. The potential of amorphous systems is exemplified by the relatively high quantum yield of 1.22 for the amorphous diphenyl tetracenes, as well as observations of rapid SF in amorphous films of rubrene.[50,52] A recent study by Sutton et al. on various rubrene derivatives in fact found that amorphous films had sites of stronger types of coupling than in crystalline form, rationalising the fast SF observed.[52]

Structural order has been examined in nanoparticles (NPs) of acene derivatives. Pensack et al. studied five different pentacene derivatives and found their morphologies could be divided into two groups; those with highly disordered arrangements (denoted "Type I" NPs); and those with ordered, crystalline NPs ("Type II"). The strong interchromophore coupling of the ordered Type II arrangements lead to much faster SF, suggesting that, at least for these materials, crystallinity may be more favorable for SF.[53]

There are various other examples in the literature on the effects of morphology on SF,[54,55] sometimes conflicting and not overly clear on the implications for the application of SF in solar cells. As mentioned, the rate of SF is commonly used to make implications about efficiency, but the two are not necessarily equivalent. There may be cases where SF is fast, but due to the the presence of phenomena such as, for example, exciton trap sites, overall efficiency is not high.[38,55,56] To make informed decisions about what kinds of materials and morphologies offer the best prospects for the application of SF in solar cells, a more thorough understanding of the mechanism of SF and how it is related to the arrangements of molecules is required.

1.3.3 Mechanism of Singlet Fission

Despite the growing number of studies on SF, the mechanism of the process is still not fully understood. As mentioned previously, it is widely agreed that SF proceeds through a correlated triplet pair intermediate, ^{1}(TT), also referred to as a multi-exciton state. Recently, SF intermediates have been observed in systems such as crystalline pentacene,[57] crystalline tetracene,[58] films of terrylenediimide,[59] and covalently linked tetracene dimers.[60] But, the exact nature of these intermediates and how they are formed is a subject of some debate. One possibility is an excimer-like state: an emissive state in which an excitation is delocalised over a pair of molecules.[29] In solution studies of substituted pentacene, and later tetracene, SF was shown to be sufficiently slow to allow identification of an intermediate that exhibits some weak emission, leading to its assigment as an excimer.[47,61] Several studies have since identified excimer intermediates in other systems,[60,62–65] but a proportion of these suggested they were in fact traps rather than precursors to triplets.[60,64,65]

Formation of ^{1}(TT) directly from a singlet exciton requires a concerted two-electron transfer process. Given the coupling of a two-electron transfer is weak in most systems, it is thought that the ^{1}(TT) intermediate can instead form through two one-electron processes through a charge transfer (CT) state.[66] The CT state can be thought of as

a state in which neighbouring molecules take on either electron or hole characteristics, and can be a distinct intermediate (real CT states) or exist as a virtual state (i.e. a state that is never significantly populated but is necessary to describe the transition to a non-CT intermediate).[66] The presence of CT states was well demonstrated in a study by Lukman et al. on linked pentacene dimers.[67] One type of dimer studied, a TIPS-substituted bipentacene, was observed to form triplet pairs through a real, observable CT intermediate with energy that could be tuned through solvent polarity. At low polarity, SF was less efficient as the energy of this CT state was higher than the preceding singlet exciton. At much higher polarities, the CT state was overly stabilised and became an energetic trap, leading to a low yield of triplets. The optimum triplet yield was for a medium-polarity solvent, in which the CT state energy was sufficiently low to compete with singlet relaxation, but not overly low so as to become a trap state. A second type of dimer, mesityl-substituted bipentacene, instead exhibited a virtual CT state. Here the singlet exciton itself had CT character, such that the singlets effectively proceeded directly to triplet pairs in a concerted process. The effect of solvent polarity in this case was only to stabilise the relaxed singlet exciton. At low polarities this stabilisation was weak, so there was less competition between relaxation and SF, and the process was efficient. Polarity dependence of SF has been linked to CT states in a number of studies, for example in NPs of diketopyrrolopyrrole, dimers of 1,3-diphenylisobenzofuran and in terrylenediimide films.[45,59,68] The observed intermediate in crystalline pentacence and tetracene was also attributed to a CT state by comparing results of time-resolved two-photon photoemission spectroscopy with density functional theory calculations.[57,58]

However, not all SF systems have characteristics consistent with CT states. For example, a study of NPs of diphenyltetracene prepared by Mastron et al. found the SF efficiency was close to that of disordered films, and the high dielectric constant of aqueous NPs did not increase efficiency as would be expected for a CT intermediate.[69] More recently, Fuemmeler et al. reported that SF in their pentacene dimers was independent of CT states.[70] An alternate mechanism suggests that CT states are not necessary for SF, instead proposing a fast non-adiabatic transition from S_1 to ^{1}(TT).[71,72]

Another important note regarding the ^{1}(TT) intermediate is that a few studies have suggested it does not always dissociate into separated triplets.[60,73] This could have significant consequences for the application of SF in solar cells, as ultimately separated triplet excitons are needed to generate charges. Why this loss occurs, whether it is common in other systems, and how it can be prevented, highlights the importance of improving the understanding of the mechanism of SF.

1.4 Aims and Research Questions

Whilst there have been many studies on how morphology and packing affect SF, the exact dependence on intermolecular distance between molecules undergoing SF has not been investigated to a large extent. This is a pertinent topic, as naively it might be predicted that SF would be faster and more efficient when the S_1 and S_0 chromophores are closer together. But intermolecular distance governs interchromophore coupling, and if the coupling in a system is too strong, the first step of SF, i.e. ^{1}(TT) formation, may be efficient, but the second step, the dissociation of ^{1}(TT) to separated triplets, may not occur at all.[29] Additionally, intermolecular distance is likely to affect other competing processes. In particular, the reverse process of SF, triplet fusion or TTA,

could also increase with average intermolecular separation, as if the initial S_1 and S_0 chromophores are closer together, so to are the resulting triplet excitons. If this is the case, there may be an optimum average intermolecular separation, where SF and TTA are balanced such that a maximum amount of triplets are produced. This would have important implications for future design of photovoltaic devices.

A study by Wu et al. gives some insight on the matter by looking at SF in crystalline films of 6,13-bis(triisopropylsilylethnyl) pentacene (TIPS-Pn) and "ADPD pentacene", which has the same structure of TIPS-Pn with nitrogens replacing two of the carbons on the terminal rings.[74] It was found that the presence of these two nitrogens causes a slightly decreased spacing in the otherwise similar packing arrangement of the molecules and resulted in a higher triplet yield than for TIPS-Pn. This suggests that a decreased spacing could lead to enhanced electronic coupling and more efficient SF. But, the molecules in this study were not identical, and differences due to their different molecular structure complicates the analysis. Another very recent study by Izadnia et al. examined an amorphous system of acene molecules by distributing them on the surface of a rare gas cluster.[75] This system allowed control over the number of molecules and the spacing between them in an inert environment. It was found that at low exciton concentrations, there was a strong dependence of the fluorescence lifetime on intermolecular distance for TIPS-Pn, but this dependence was absent for anthracene. Given anthracene does not undergo SF, but TIPS-Pn does, this suggests the reduction in lifetime is due to SF.

Both of these studies are insightful, but a more comprehensive analysis of the distance dependence of SF may yet add further knowledge on the mechanism and the effects of morphology. Particularly the effect on the triplet and SF intermediate populations, as well as triplet-triplet annihilation still require analysis. The aim of the research presented in this thesis is to further investigate the effect of intermolecular distance on SF, and in particular what implications it has for elucidating the mechanism of SF and its applications to photovoltaic devices. Specifically, we provide a more complete picture by studying a range of different intermolecular distances and by directly probing the populations of the triplet excited states and SF intermediates, in addition to the singlet states.

In the research presented in this thesis, we take an alternative approach to controlling intermolecular distance, or separation between molecules. By embedding a molecule that undergoes SF in a polymer matrix in the form of an aqueous dispersion of NPs, the mass ratio of molecule to polymer can be varied to control the average intermolecular separation between molecules. 6,13-bis(triisopropylsilylethynyl) pentacene (TIPS-Pn) (Figure 1.6a), is an ideal model system to study, as it has already been shown to undergo fast and efficient singlet fission in solution, film and neat NP form.[47,54,56] Additionally, the TIPS sidegroups make it soluble in organic solvents such as tetrahydrofuran, but not in water, so TIPS-Pn can form an aqueous suspension, rather than a solution, which is key for the control of intermolecular distance. The polymer poly(methyl methacrylate) (PMMA) (Figure 1.6b) was chosen as the host matrix, as it has no absorption or emission in the visible spectrum, and is known by our group to form stable aqueous NP suspensions.

Assuming TIPS-Pn is evenly dispersed thoughout the NP, changing the TIPS-Pn:PMMA mass ratio allows the average intermolecular separation to be controlled. For example, if there is a high proportion of PMMA compared with TIPS-Pn, the TIPS-Pn molecules will be relatively isolated and average intermolecular separation

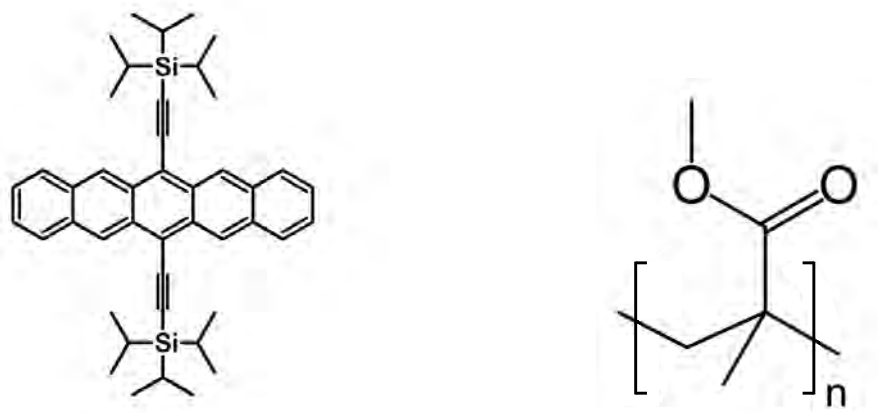

(a) **(b)**

Figure 1.6: Structure of triisopropylsilylethnyl (TIPS) pentacene (Pn) (a) and poly(methyl methacrylate) (PMMA) (b).

will be large. Conversely, if there is a low proportion of PMMA, or high proportion of TIPS-Pn, the average intermolecular separation will be small. As well as allowing control over the intermolecular separation, NPs are a simple and practical system to study compared with for example, films, which can have issues with degradation, consistency and quality, and can also be difficult to prepare.

Ultimately, we aim to study the dynamics of SF in these NP suspensions using steady-state and time resolved absorption and fluorescence spectroscopy. These tools are common techniques for studying SF, as they allow the identification of the different species involved in singlet fission (i.e. S_0, S_1 and T_1), and a means to follow the evolution of these species over time. Details of these methods are given in Chapter 2. In Chapter 3, we outline some basic characterisation of the TIPS-Pn:PMMA NPs, and provide evidence that the TIPS-Pn molecules are randomly dispersed throughout the NP, and thus that the average intermolecular separation increases with proportion of PMMA. In Chapter 4, time-resolved fluorescence upconversion and transient absorption are used to demonstrate the presence of the SF of TIPS-Pn in these NPs, and investigate the change in efficiency and rate of SF with intermolecular separation. Lastly in Chapter 5, we present a kinetic model to describe SF in the NPs which explains the observed trends in the absorption and fluorescence, and provides detailed molecular-level insight into the effect of intermolecular separation on the SF process.

CHAPTER 2
Methods

2.1 Preparation of Aqueous Nanoparticle Suspensions

2.1.1 Materials

6,13-Bis(triisopropylsilylethynyl)pentacene (TIPS-Pn, 99.9%) was purchased from Ossila and used as supplied. Poly(methyl methacrylate) (PMMA, average MW: 120000, degree of polymerisation: 1200) and the surfactant poly(oxyethylene)nonylphenyl ether (Igepal CO-520) were purchased from Sigma-Aldrich. HPLC grade tetrohydrofuran (THF) was purchased from RCI Labscan and freshly distilled prior to use. All water used in experiments was purified using a 10 MΩ Millipore Milli-Q Reagent Water System fitted with a 0.45 µm filter.

2.1.2 Nanoparticle Preparation

Various TIPS-Pn/PMMA nanoparticle (NP) suspensions were prepared by a reprecipitation method based on that developed by Kasai and coworkers.[76,77] In this method, a volume of conjugated polymer, or in this case polymer/TIPS-Pn mixture, in a good solvent such as THF is rapidly injected into a poor solvent that is miscible with the good one, such as water. Unfavorable interactions between the polymer and the poor solvent cause the polymer chains to collapse and fold, forming roughly spherical particles that minimise the solvent–polymer interactions, as illustrated in Figure 2.1.[76,78–80] The resulting size of particles depends on temperature, solvent, and polymer concentration, but they are typically formed in a range of 10 to a few hundred nanometers.[76,77,79] Other methods of NP formation, such as miniemulsion use surfactants to keep the NPs in suspension.[80] In the re-precipitation process, however, surfactants are not necessary, except at very high concentrations.[81,82] As NP concentration is increased, the likelihood of NPs colliding increases until eventually aggregation is unavoidable. In this case, surfactants can then be used to add additional stability and extend the possible range of concentrations. In this study, high concentrations of NPs were necessary to achieve a range of TIPS-Pn:PMMA mass ratios without lowering the overall TIPS-Pn concentration. This meant surfactant was required to stabilise the highest ratios (1:5 to 1:100). Therefore, although not necessary, for consistency an amount of surfactant proportional to the total PMMA concentration was included in all the samples. Results were compared for the small mass ratios (1:0, 1:0.5, 1:1) without surfactant, and no differences were observed in the NP characteristics.

To prepare the NPs, stock solutions were prepared for each of TIPS-Pn, PMMA and surfactant by dissolving the appropriate amount in freshly distilled THF. Volumes of each solution were then combined to make a mixture stock solution of the desired TIPS-Pn:PMMA ratio. An example of quantities used for different samples is given in

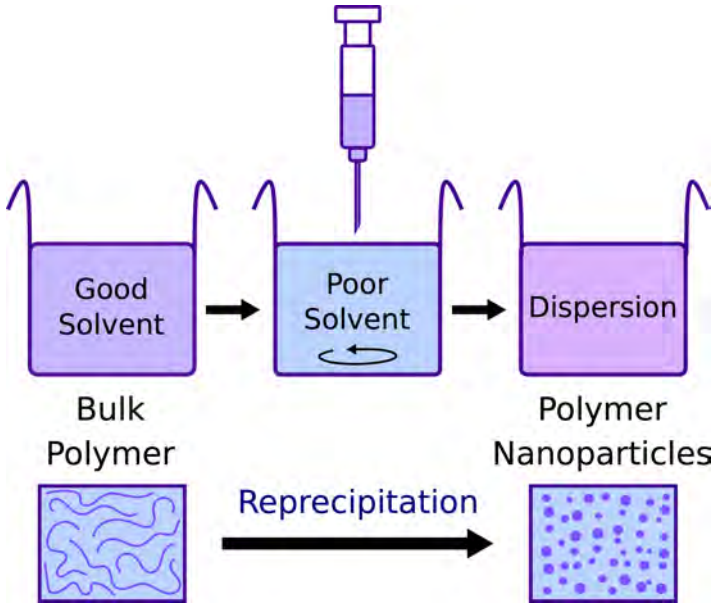

Figure 2.1: Preparation of polymer nanoparticles by the reprecipitation method.

Table 2.1. The mixture stock solution was injected into 5 times the volume of vigorously stirring water and left to stir for approximately 5 minutes. The THF was then removed under reduced pressure and the NP suspension further concentrated to reach a TIPS-Pn concentration of $\sim 0.1\,\mathrm{g\,L^{-1}}$. The samples were finally filtered through a 0.2 µm hydrophilic syringe filter (Sartorius Minisart NML). Typical final concentrations are given in Table 2.1.

2.2 Steady-State Optical Measurements

Steady-state UV-visible absorption spectra were obtained with a Cary Varian 1E UV-visible spectrophotometer using a 2 mm path length quartz cuvette (Starna Cells 21-Q). Fluorescence spectra were measured on a Perkin Elmer LS 55 fluorescence spectrophotometer with an excitation wavelength of 590 nm, excitation slit bandwidth of 5 nm and emission slit bandwidth of 15 nm, using a 1 cm path length quartz cuvette (Starna Cells 3-Q).

2.3 Scanning Electron Microscopy

Scanning electron microscopy (SEM) is a method of collecting high-resolution images of samples on a nm scale using a focused beam of electrons. Images were collected at Adelaide Microscopy with the assistance of Lynette Waterhouse and Animesh Basak using a focused ion beam (FIB) scanning electron microscope. This combines two beams, a focused beam of Ga^+ ions and a beam of electrons, enabling sputtering of the surface of a sample by ions to emphasise sub-surface features and collection of electron-induced signals from the exposed surfaces. At a low ion beam current the FIB enables high-resolution images.

SEM images were collected of a 1×10^{-3} $\mathrm{gL^{-1}}$ suspension of pure TIPS-Pn NPs as well as Milli-Q water to ensure features observed in the SEM image were due to the

Table 2.1: Quantities used to prepare NP suspensions of different TIPS-Pn:PMMA mass ratios

TIPS-Pn:PMMA mass ratio	Component	Concentration in individual stock ($\times 10^{-3}$ gL^{-1})	Volume used (mL)	Concentration in final stock ($\times 10^{-3}$ gL^{-1})	Volume final stock (mL)	Volume water (mL)	Concentration of NPs ($\times 10^{-3}$ gL^{-1})	Volume of NPs (mL)
1:0	TIPS-Pn	400	0.75	20	15.00	75.00	100	3.00
	PMMA	-	-	-			0	
	CO520	500	0.30	10			50	
	THF	-	13.95	-			-	
1:0.5	TIPS-Pn	400	1.50	20	30.00	150.00	100	6.00
	PMMA	400	0.75	10			50	
	CO520	500	0.60	10			50	
	THF	-	27.15	-			-	
1:1	TIPS-Pn	400	0.75	20	15.00	75.00	100	3.00
	PMMA	400	0.75	20			100	
	CO520	500	0.60	20			100	
	THF	-	12.90	-			-	
1:3	TIPS-Pn	400	0.75	20	15.00	75.00	100	3.00
	PMMA	400	2.25	60			300	
	CO520	500	1.80	60			300	
	THF	-	10.20	-			-	
1:5	TIPS-Pn	400	1.00	20	20.00	100.00	100	4.00
	PMMA	400	5.00	100			500	
	CO520	2000	1.00	100			500	
	THF	-	13.00	-			-	
1:7	TIPS-Pn	400	0.75	20	15.00	75.00	100	3.00
	PMMA	400	5.25	140			700	
	CO520	2000	1.05	140			700	
	THF	-	7.95	-			-	
1:10	TIPS-Pn	400	0.55	20	11.00	55.00	100	2.20
	PMMA	400	5.50	200			1000	
	CO520	2000	1.10	200			1000	
	THF	-	3.85	-			-	
1:100	TIPS-Pn	240	0.50	6	20.00	100.00	30	4.00
	PMMA	640	18.75	600			3000	
	CO520	16000	0.75	600			3000	
	THF	-	0	-			-	

NPs rather than contaminants. The samples were dropped through a 0.2 µm filter onto clean silicon wafers. They were then coated with 5 nm of platinum and images taken on a FEI Helios Nanolab 600 dual beam FIB SEM operating at 5 kV.

2.4 Fluorescence Upconversion Spectroscopy

Time-resolved fluorescence measurements were obtained using fluorescence upconversion (UC). This is a technique with a femtosecond time resolution, and was used to monitor the fluorescence of samples for up to 3 ns after excitation. The operation of fluorescence upconversion is as follows: The first laser pulse, the "pump" beam, is used to excite the sample and generate fluorescence, which is then focused onto a β-barium borate (BBO) crystal. A second pulse, the "gate" beam, is focused onto the same BBO crystal, as shown in Figure 2.2. The non-linear properties of the BBO crystal allow the two pulses to form photons of a higher energy through sum frequency generation (SFG). Thus the fluorescence is "upconverted" to a higher frequency,

$$\hbar\omega_{\text{upconverted}} = \hbar\omega_{\text{gate}} + \hbar\omega_{\text{fluorescence}},$$

where ω_{gate} is the frequency of the gate pulse and $\omega_{\text{fluorescence}}$ is the frequency of fluorescence being studied. The detector only detects this upconverted frequency, which is only produced when the fluorescence and the gate pulse are overlapped in time. The time-resolved data is then obtained by delaying the arrival of the gate pulse by

different amounts of time after the initial excitation. Thus rather than continuously detecting fluorescence after a single excitation, a different time is measured after each excitation by changing the gate pulse delay. In this way the resolution is not limited by the speed of the detector. The fluorescence wavelength to be studied is selected by phase matching, i.e, rotating the BBO crystal such that SFG of the gate beam and wavelength of interest give the wavelengths detected by the detector.

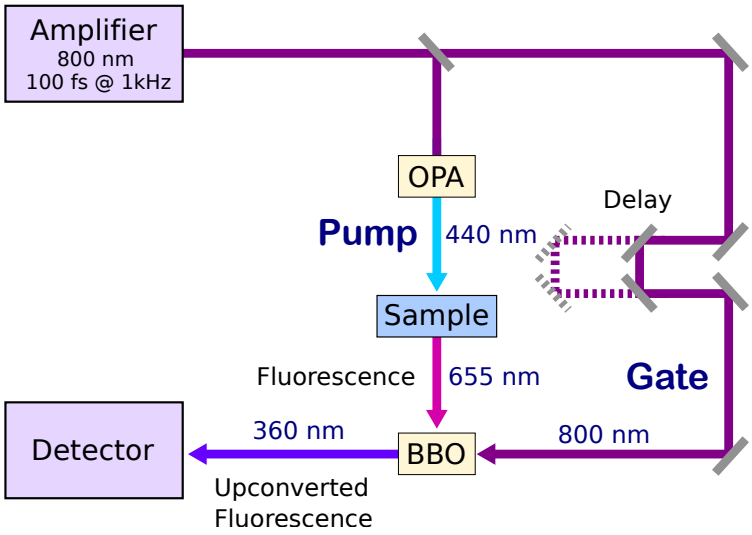

Figure 2.2: Schematic of fluorescence upconversion apparatus used to collect time-resolved fluorescence of TIPS-Pn (beams are not drawn to equal length).

The fluorescence spectrometer used to collect data on the TIPS-Pn samples is shown in Figure 2.2 (Ultrafast Systems, Halcyone). The pulses were sourced from a Ti:sapphire regenerative amplifier (Spectra Physics, Spitfire), giving pulses centered at 800 nm with a 1 kHz repetition rate and 100 fs duration. The samples were excited with 440 nm pump pulses obtained with an optical parametric amplifier, or OPA (Light Conversion, TOPAS-C) using the fourth harmonic of the signal at 1760 nm. These pulses had an energy of $\sim$0.25 µJ and were focused to a full width half maximum (FWHM) spot size of 0.5 mm. The polarization was rotated to the magic angle (54.7°) relative to the gate to negate anisotropy effects. A small fraction of the 800 nm amplifier output was used for the gate beam, focussing onto the 0.4 mm BBO crystal used for sum-frequency generation with the fluorescence. The detector used to detect the intensity of the upconverted fluorescence was a photomultiplier tube attached to a double monochromator. The fluorescence wavelength of TIPS-Pn selected was 655 nm, resulting in an upconverted wavelength of 360 nm. Each experiment was averaged over three runs, with the sample stirred continuously. Measurements were taken in a 0.2 mm quartz cuvette (Starna Cells 21-Q) at a TIPS-Pn concentration of 0.1 g L^{-1}, and samples were observed to degrade by less than 10% over the course of the experiment (approximately 90 minutes).

2.5 Time-Correlated Single Photon Counting

Time-correlated single photon counting (TCSPC) measurements were additionally used to measure time-resolved fluorescence. This has a poorer time resolution than fluores-

cence upconversion, but it is highly sensitive, making it a useful technique to monitor fluorescence over a longer (ns) time scale. The set up for TCSPC is the same as fluorescence upconversion, but without the gate beam, and with the detector set to detect the fluorescence at 655 nm. This means the time resolution is limited to ∼1 ns by the speed of the detector, but the raw fluorescence is detected, resulting in greater sensitivity and the ability to measure over a significantly longer time scale (i.e. up to 50 ns). The bin size used for TCSPC was 50 ps, with an instrument response function (IRF) of 0.6 ns.

2.6 Transient Absorption Spectroscopy

Transient absorption (TA) spectroscopy is a technique commonly used to the study the kinetics of photo-physical processes. By monitoring changes in absorption over time, useful information can be obtained about the formation, decay, and interactions of different species. Pump–probe transient absorption spectroscopy in particular is a useful technique for monitoring the excited states of a sample. This is a two-pulse technique, in which a "pump" pulse is used to excite the sample, and a "probe" pulse is used to measure the absorption after excitation. The basic set up of a pump–probe TA spectrophotometer is given in Figure 2.3. The pump pulse, typically chosen to match an S_0 to S_n transition, is modulated to arrive once every two probe pulses, so the probe is then able to detect the absorption with and without the pump, $A_{\text{pump on}}$, and $A_{\text{pump off}}$, respectively. Pump pulse modulation allows continuous collection of the excited and steady state spectra to reduce noise from fluctuations in the laser power. Data is then recorded as the change in absorbance:

$$\Delta A = A_{\text{pump on}} - A_{\text{pump off}},$$

which is equivalent to

$$\Delta A = A_{\text{excited state}} - A_{\text{steady state}}.$$

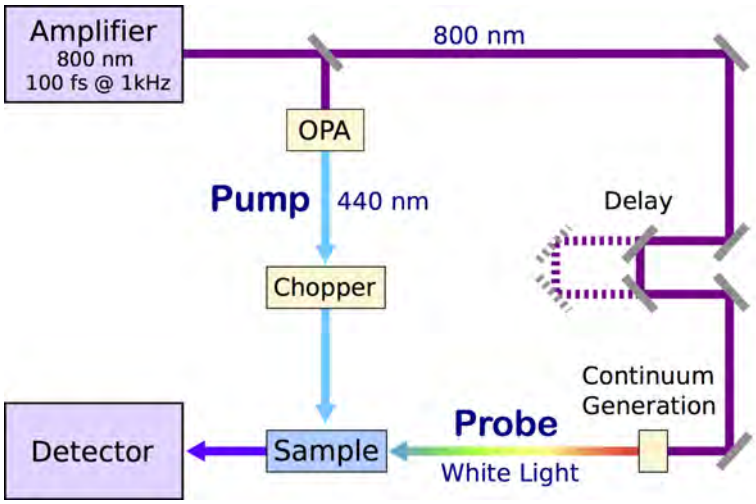

Figure 2.3: Schematic of the transient absorption apparatus used to collect time-resolved absorption of TIPS-Pn (beams are not drawn to equal length).

Time-dependent measurements are achieved by delaying the arrival of the probe pulse. Each time the pump excites the sample, the probe pulse is delayed to arrive at

some time t after excitation. The time resolution is then only limited by the duration of the pulses, and is typically on the order of femto to picoseconds. Additionally the probe pulse can be a white light continuum rather than a single wavelength, so multiple wavelengths can be detected at once. If t is the time after the pump pulse, the change in absorption recorded is then:

$$\Delta A(\lambda, t) = A(\lambda, t) - A_{\text{pump off}}(\lambda).$$

A negative ΔA signal implies a decrease in the steady-state absorbance. This is referred to as a ground-state bleach (GSB), and results from the loss of ground-state population by the pump excitation, as well as any other processes that deplete the ground-state. Negative signals can also be obtained if the sample emits light, for example, from stimulated emission (SE) caused by a probe photon equal to the S_1 to S_0 transition. The resulting emission will be Stokes shifted from the GSB. A positive ΔA signal implies the formation of a population that was not present in the absence of the pump pulse. For example, if S_1 is generated by the pump, this state can then absorb the probe to jump to a higher excited state. The resulting S_1 to S_n transition is referred to as an excited-state absorption (ESA). The types of transitions observed in a TA spectrum are outlined in Figure 2.4.

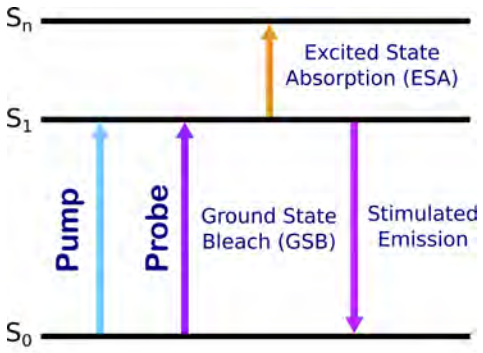

Figure 2.4: Possible transitions measured in a pump-probe TA experiment. The ground-state bleach and stimulate emission appear as negative ΔA signals, whilst excited state absorptions appear as positive ones.

To obtain TA of the TIPS-Pn samples, the transient absorption spectrometer (Ultrafast Systems, Helios) used the output of a Ti:sapphire regenerative amplifier (Spectra-Physics, Spitfire Pro XP 100F) to produce 800 nm pulses of 100 fs duration operating at a 1 kHz repetition. An optical parametric amplifier (OPA) (Light Conversion, TOPAS-C) was used to obtain the 440 nm pump beam using the fourth harmonic of the signal. The pump pulse energy was 1.5 µJ with a FWHM spot size of 740 µm. This was mechanically chopped at 500 Hz to produce one pump pulse every two probe pulses. The probe was a white light continuum obtained by focusing a small portion of the 800 nm amplifier output into a 3.2 mm sapphire crystal. This was then split into signal and reference beams, and focused onto the sample with a FWHM spot size of 225 µm. This was finally detected using a linear CMOS sensors (Ultrafast Systems, CAM-VIS-2). Experiments were performed at 21°C with the pump polarization rotated to the magic angle (54.7°) relative to the probe. Measurements were taken in a 0.2 mm quartz cuvette (Starna Cells 21-Q) at a TIPS-Pn concentration of approximately $0.1\,\text{g}\,\text{L}^{-1}$. Each experiment was averaged three times, stirring continuously.

Photo-degradation was observed to be less than 5% after each experiment. All spectra were corrected for the dispersion of the probe.

2.7 Fitting and Deconvolution of Transient Absorption Spectra

Transient absorption spectra often contain contributions from multiple different species. When singlet fission occurs, for example, the absorption of the S_0, S_1, T_1 and any potential intermediate states are all present, resulting in a complex spectral signature. With insight into the kinetic processes occuring, regions of the TA can be assigned to a particular species. For example, the triplet in TIPS-Pn is widely agreed to have a strong ESA around 500 nm, and the singlet a shallower, broader absorption from around 500 nm to 600 nm, based on the formation and decay times of these peaks.[39,47,53,56,73,83] It is common practice to select a single wavelength of these regions to use as a kinetic trace for a population. If the spectral shape of the said population is already well established and does not overlap with another, this is a valid approach. However, in many systems the transient absorption is much more complex, with many overlapping contributions such that there are no regions that can be attributed to a single species, and thus no single wavelengths that can be used as a kinetic trace for any population. In the visible region for TIPS-Pn for example, the T_1 ESA overlaps with the S_1 ESA, the S_1 ESA overlaps with the GSB, and the GSB overlaps with stimulated emission. While it might be agreed that a particular region is *mostly* one component, it is not reliable to use its kinetics unless the exact proportions are known. This is particularly important in cases in which quantitative measures of populations are needed. When determining the triplet yield in SF, for example, the triplet ESA also contains contributions from the singlet, resulting in an overestimate if this is used to determine triplet concentration.

To extract kinetics from more complicated spectra, the TA needs to be resolved into its respective components. Following the convention of Roberts et al. [50] we term these components "basis spectra", ϵ. Then, if a sample contains n populations, with basis spectra $\epsilon_n(\lambda)$ and time-dependent concentration $C_n(t)$, the TA data can be expressed as

$$\Delta A(\lambda, t) = C_1(t)\epsilon_1(\lambda)l + C_2(t)\epsilon_2(\lambda)l + C_3(t)\epsilon_3(\lambda)l + ... + C_n(t)\epsilon_n(\lambda)l \qquad (2.1)$$

where l is the path length. Once the relevant basis spectra are known, and given a large enough wavelength range (number of data points $\geq n$), Equation 2.1 can be solved to obtain the kinetics in the form $C_1(t), C_2(t)$, to $C_n(t)$.

One method commonly used to deconvolute TA spectra is global target analysis.[84–87] This is typically done on software such as Glotaran, which uses singular value decomposition (global) and differential equations (target) to extract both spectra and population kinetics.[88] However, this method requires a model of the kinetics as an input, and extracts the spectra to best fit the TA data to this model. The resultant spectra therefore are not necessarily physical, particularly if the model is not accurate. An alternative method to determine the T_1 spectra in particular is through sensitisation experiments. This involves doping a sample with a triplet sensitizer, such as N-methylfulleropyrrolidine or anthracence.[47,60,84] These materials undergo rapid intersystem crossing to form triplets, which they then transfer to the sample studied, resulting in nearly full conversion from S_1 to T_1. This is a useful technique, but it is

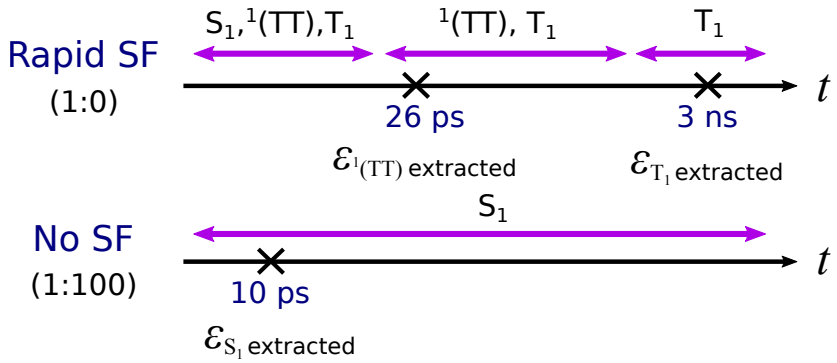

Figure 2.5: T_1 and ^{1}(TT) basis spectra (ϵ_{T_1} and $\epsilon_{^1(TT)}$, respectively) can be extracted from a sample with rapid SF at some time after S_1 has decayed. The S_1 basis spectrum (ϵ_{S_1}) is extracted from a sample in which no SF occurs, and thus only has S_1 present. The times used to extract each spectra are indicated by crosses.

not practical for all systems, particularly not solid or colloidal systems such as NPs or films. Additionally, the presence of the sensitizer may alter the environment of the triplets, and thus the spectra of sensitised triplets may be subtly different from those generated by SF. The method we present here outlines an alternative approach to extract basis spectra, and fit these the TA to obtain kinetics without the use of sensitisers or a model.

Given TIPS-Pn is known to undergo singlet fission, the components of interest here are the S_1 and T_1 states. Technically the S_0 state could also be included to account for the GSB, but since singlets and triplets bleach the ground state in the same way, for simplicity we incorporate the GSB into the basis spectra of these. This results in some negative ϵ values. Thus the basis spectra here only make sense in the context of transient absorption. Recent studies have also identified spectral features due to the triplet pair intermediate, ^{1}(TT).[60,67,85] We therefore consider deconvolving the spectra with an additional intermediate species. The resulting fits with and without this species are referred to as 3-component and 2-component spectral fits, respectively.

T_1 Basis Spectrum. We determined the T_1 basis spectrum using a sample that undergoes rapid SF. If SF is fast and complete, there will eventually be a pump-probe delay time sufficiently long such that all the S_1 have decayed or undergone fission, and the only remaining populations are T_1 and ground-state molecules. Previous studies on TIPS-Pn nanoparticles suggest SF is rapid in pure TIPS-Pn NPs, so we used a very late time measurement (e.g. 3 ns) of the 1:0 TIPS:PMMA sample, as shown in Figure 2.5.[53,56] At this time there is then no S_1 ESA or stimulated emission in the TA, so the ground state bleach at 646 nm, $\Delta A(646\text{ nm}, 3\text{ ns})$, represents the exact amount of bleached ground-state molecules. This is then equal to the amount of T_1 present. Using the steady-state extinction coefficient of the singlet ground state at 646 nm, $\epsilon_{SS}(646\text{ nm})$, the concentration of T_1, C_{T_1} can be determined at 3 ns from

$$C_{T_1}(3\text{ ns}) = \frac{\Delta A(646\text{ nm}, 3\text{ ns})}{-\epsilon_{SS}(646\text{ nm})l},$$

where l is the path length. The triplet extinction coefficient, ϵ_{T_1}, can then be found at each wavelength to give the triplet basis spectrum,

$$\epsilon_{T_1}(\lambda) = \frac{\Delta A(\lambda, 3 \text{ ns})}{C_{T_1}(3 \text{ ns})l}.$$

S_1 Basis Spectrum. Obtaining a pure S_1 spectrum is relatively complicated, as all samples studied potentially have some degree of SF which is so rapid that there are no times at which only singlets are present. To minimise the amount of SF occuring, a 1:100 TIPS:PMMA sample was used, with an average intermolecular TIPS-Pn separation of 5 nm. As will be discussed in the results section, the fluorescence lifetime of this sample is the same as that of the dilute solution, only fitting to a single exponential with a 12 ns lifetime. This implies that there are no additional non-radiative decay pathways, i.e, no SF. The TA spectra of this sample agree with this argument, through its resemblance to the solution spectrum and lack of triplet features. The 1:100 sample therefore only has singlets present and can be used to obtain the S_1 basis spectrum, using

$$C_{S_1}(10 \text{ ps}) = \frac{\Delta A(646 \text{ nm}, 10 \text{ ps})}{-\epsilon^*_{SS}(646 \text{ nm})l}$$

and

$$\epsilon_{S_1}(\lambda) = \frac{\Delta A(\lambda, 10 \text{ ps})}{C_{S_1}(10 \text{ ps})l}.$$

To obtain the 1:100 sample a low concentration of $0.03\,\text{g}\,\text{L}^{-1}$ TIPS-Pn was used, so the TA was performed in a 1 cm path length cuvette and collected at 10 ps with additional averaging. Given only singlets are present, this time is arbitrary; however the relatively short time of 10 ps was chosen to maximise TA signal. It should be also be noted that the presence of stimulated emission and S_1 ESA in this sample means the 646 nm peak does not represent the exact GSB signal, so we cannot use $\epsilon_{SS}(646 \text{ nm})$ to determine $C_{S_1}(10 \text{ ps})$ as was done with T_1. We therefore estimated the magnitude of fluorescence and ESA in this region to define a modified steady state extinction coefficient, $\epsilon^*_{SS}(646 \text{ nm})$. This approximation may slightly affect the magnitude of the resulting S_1 concentration profiles, but will not effect the spectral shape, nor the magnitudes of the T_1 and ^{1}(TT) populations (as these are determined from their own extinction coefficients).

2.7.1 Two-Component Fits

Given the extracted basis spectra, and assuming they are the only components present, the concentration of S_1 and T_1 can be solved for each time t using

$$\Delta A(\lambda, t) = \epsilon_{S_1}(\lambda)C_{S_1}(t)l + \epsilon_{T_1}(\lambda)C_{T_1}(t)l. \tag{2.2}$$

As the only fluorescent population is S_1, C_{S_1} can additionally be constrained to match the fluorescence UC data. If $f(t)$ represents the fluorescence UC signal, normalised and convoluted with the TA IRF, and $C_{S_{1\max}}$ is the maximum S_1 concentration then we have

$$C_{S_1}(t) = C_{S_{1\max}} f(t).$$
$$\therefore \Delta A(\lambda, t) = \epsilon_{S_1}(\lambda)C_{S_{1\max}} f(t)l + \epsilon_{T_1}(\lambda)C_{T_1}(t)l \tag{2.3}$$

We used a least squares fit over all wavelengths and times to obtain the best fit values for the unknowns, $C_{T_1}(t)$ and $C_{S_{1\max}}$.

2.7.2 Three-Component Fits

It has been suggested in the literature that the intermediate ^{1}(TT) can be observed in some systems.[60,67,85,86] We also considered this possibility by extracting a third basis spectrum of a ^{1}(TT) intermediate species that persists after S_1 has decayed, but disappears before T_1 decays as described below.

^{1}(TT) Basis Spectrum. To extract the basis spectrum of the ^{1}(TT) component we can again use the 1:0 TIPS-Pn:PMMA TA. Assuming SF is rapid, there exists some time during which S_1 has completely decayed, but T_1 and the intermediate component are still present, as indicated in Figure 2.5. As will be discussed in Chapter 4, by 40 ps the fluorescence intensity is zero, indicating S_1 has completely decayed. This time can thus be used for deducing the ^{1}(TT) basis spectrum. We can extract the ^{1}(TT) spectrum by estimating the proportion of T_1 decay between 40 ps and 3000 ps. If we denote this proportion p, then:

$$\begin{aligned}
C_{\mathrm{T_1}}(3000\text{ ps}) &= (1-p)C_{\mathrm{T_1}}(40\text{ ps}) \\
\therefore \Delta A(\lambda, 40\text{ ps}) &= \epsilon_{\mathrm{T_1}}(\lambda)C_{\mathrm{T_1}}(40\text{ ps})l + \epsilon_{^1(\mathrm{TT})}(\lambda)C_{^1(\mathrm{TT})}(40\text{ ps})l \\
&= \epsilon_{\mathrm{T_1}}(\lambda)\frac{C_{\mathrm{T_1}}(3000\text{ ps})}{1-p}l + \epsilon_{^1(\mathrm{TT})}(\lambda)C_{^1(\mathrm{TT})}(40\text{ ps})l \\
&= \frac{\Delta A(\lambda, 3000\text{ ps})}{1-p} + \epsilon_{^1(\mathrm{TT})}(\lambda)C_{^1(\mathrm{TT})}(40\text{ ps})l \\
\therefore \epsilon_{^1(\mathrm{TT})}(\lambda) &= \frac{\Delta A(\lambda, 40\text{ ps}) - \frac{\Delta A(\lambda, 3000\text{ ps})}{1-p}}{C_{^1(\mathrm{TT})}(40\text{ ps})l}
\end{aligned}$$

where

$$C_{^1(\mathrm{TT})}(40\mathrm{ps}) = \frac{\Delta A(649\mathrm{nm}, 40\mathrm{ps}) - \frac{\Delta A(649\mathrm{nm}, 3000\mathrm{ps})}{1-p}}{-2 \times \epsilon_{\mathrm{SS}}(646\mathrm{nm})l}.$$

The 507 nm peak, which is predominantly T_1, decays by 27% between 40 ps and 3000 ps (see Chapter 4), so T_1 must decay somewhere between 0 and 27% ($0 \leq p \leq 0.26$). For simplicity, the fits presented in the main text of this study, both for the spectral fitting and kinetic fitting, were done in the middle, assuming 15% T_1 decay ($p = 0.15$). Given that a 27% decay corresponds to a decay time constant of around 10000 ps, 15% 18000 ps, and 0% an infinite lifetime, and our experimental window is only 3000 ps, this choice does not significantly affect the results of the fits, but it does slightly vary the respective magnitudes of $C_{\mathrm{T_1}}$ and $C_{^1(\mathrm{TT})}$. The 27% decay implies all the absorption at 507 nm is due to T_1, and 0% means there is a significant ^{1}(TT) component there, so these two extremes give the upper and lower bounds of the amount of T_1 produced. As such fits were additionally done for the 0% and 27% decays, and the singlet fission yields in this study (Equation 1.1) are reported as the ranges given by these extremes.

Given the S_1, T_1 and ^{1}(TT) basis spectra, we decomposed the TA as with the 2-component fit, using

$$\Delta A(\lambda, t) = \epsilon_{\mathrm{S_1}}(\lambda)C_{\mathrm{S_1(t)}}l + \epsilon_{^1(\mathrm{TT})}(\lambda)C_{^1(\mathrm{TT})}(t)l + \epsilon_{\mathrm{T_1}}(\lambda)C_{\mathrm{T_1}}(t) \tag{2.4}$$

or with the time-resolved fluorescence for S_1 using

$$\Delta A(\lambda, t) = \epsilon_{\mathrm{S_1}}(\lambda)C_{\mathrm{S_{1max}}}f(t)l + \epsilon_{^1(\mathrm{TT})}(\lambda)C_{^1(\mathrm{TT})}(t)l + \epsilon_{\mathrm{T_1}}(\lambda)C_{\mathrm{T_1}}(t) \tag{2.5}$$

A least squares fit over all wavelengths and times measured gives $C_{S_{1\,max}}$, $C_{1(TT)}(t)$ and $C_{T_1}(t)$.

2.8 Modelling Rate Processes of Singlet Fission

To provide further insight into the efficiency of SF in TIPS-Pn/PMMA NPs, and how it is affected by intermolecular separation, it is useful to fit the TA data to a kinetic model. The exact mechanism of singlet fission is not well established, and is likely different in different systems. The simplest description involves the excited S_1 population either decaying radiatively with the rate k_{S_1}, or undergoing SF with a nearby ground-state molecule to give a pair of triplets with the rate k_{SF}. This is represented schematically in Figure 2.6, in which we have also included the excitation of S_0 with instrument response function $G(t)$, and the decay of T_1 with rate k_{T_1}.

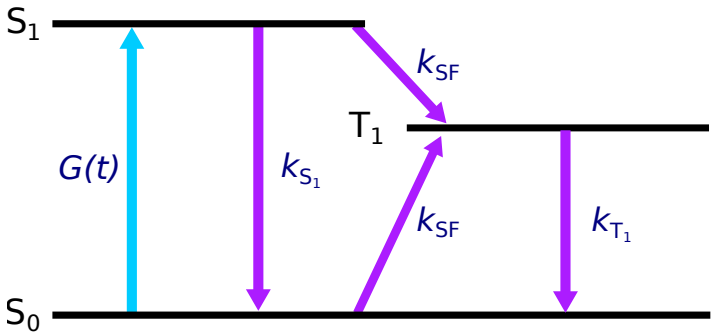

Figure 2.6: Schematic of a simple model of SF.

This simple model can be described by the following four equations, describing the excitation of the ground state to give S_1 (a), SF to give two triplets (b), the decay of S_1 to the ground state (c) and the decay of T_1 (d).

$$\begin{aligned} S_0 &\xrightarrow{G(t)} S_1 && \text{(a)} \\ S_0 + S_1 &\xrightarrow{k_{SF}} T_1 + T_1 && \text{(b)} \\ S_1 &\xrightarrow{k_{S_1}} S_0 && \text{(c)} \\ T_1 &\xrightarrow{k_{T_1}} S_0 && \text{(d)} \end{aligned} \tag{2.6}$$

With these equations in mind the model can now described with a series of coupled differential equations, representing the rate of change in different populations as shown below:

$$\begin{aligned} \frac{d[S_0]}{dt} &= -G(t)[S_0] - k_{SF}[S_1][S_0] + k_{S_1}[S_1] + k_T[T_1]; \\ \frac{d[S_1]}{dt} &= G(t)[S_0] - k_{S_1}[S_1] - k_{SF}[S_1][S_0]; \\ \frac{d[T_1]}{dt} &= 2 \times k_{SF}[S_1][S_0] - k_{T_1}[T_1]. \end{aligned} \tag{2.7}$$

$[S_0]$, $[S_1]$ and $[T_1]$ are the time-dependent concentrations of the ground, excited singlet and excited triplet states, respectively. The IRF for the laser excitation of S_0, $G(t)$,

was taken to be a Gaussian with a width given by the instrument response time. For laser excitations in the power regimes studied in this thesis, the number of excitons was low compared with the number of ground-state molecules. We can thus simplify the model by assuming the rate of change of $[S_0]$ is approximately zero, and drop this component. Given the abundance of S_0, SF can be considered a pseudo-first order process, so we can neglect $[S_0]$ concentration dependence in the SF terms. Redefining k_{SF} as a unimolecular rate constant, and fitting to times after the excitation pulse (i.e. when $G(t)$=0), this leads to the much simpler system in Equation 2.8, which is also represented schematically in Figure 2.7:

$$\begin{aligned}\frac{d[S_1]}{dt} &= -k_{S_1}[S_1] - k_{SF}[S_1];\\ \frac{d[T_1]}{dt} &= 2 \times k_{SF}[S_1] - k_{T_1}[T_1].\end{aligned} \tag{2.8}$$

As well as neglecting $[S_0]$, we also assumed the power was sufficiently low such that there was no exciton-exciton annihilation. We note, however, that many previous studies discussed in this thesis have included annihilation, in particular to describe the decay of T_1. This has been done by adding a second order term, $-k_{TTA}[T_1]^2$, to the rate of T_1 decay in Equation 2.8 (i.e. including the reverse process of Equation 2.6b). It is possible that, because of the close proximity of triplets when they are initially formed, triplet-triplet annihilation (TTA) is in fact a major decay pathway even in low-power studies. However, SF in TIPS-Pn is known to be exothermic (the energy of the T_1 state relative to the ground state is less than half that of S_1, 0.78 eV and 1.9 eV, respectively), so TTA should be disfavoured.[89] Additionally, given the triplet decay was observed to be slow, the relatively short time regimes here are unlikely to exhibit the effects from TTA, so to begin with it was excluded from our model.[39]

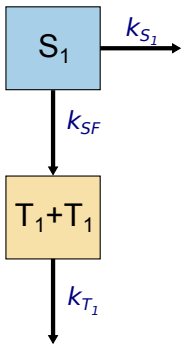

Figure 2.7: Flow diagram of a simple model for SF.

A range of values have previously been reported for k_{S_1}, k_{T_1}, and k_{SF}, or alternatively, their inverses τ_{S_1}, τ_{T_1}, and τ_{SF}, as given in Table 2.2. These values vary depending on the morphology and material studied. For TIPS-Pn, the natural lifetime of S_1, τ_{S_1}, has been reported to be between 12 and 17 ns in solution, but in crystalline films of pentacene without the TIPS side groups this value was found to be 10 times shorter at 1.2 ns.[38,39,47] The T_1 lifetime τ_{T_1} has been measured as 2.1 µs, 6.5 µs, and 954 ps in film, solution, and NP form, respectively.[47,56,83] The significantly faster decay in the NPs is possibly due to TTA of recently separated triplets, due to slower diffusion in the more disordered system. In composite TIPS-Pn/electron-acceptor films, TTA occurred on a range of time scales between 50 and 370 ns, and triplet lifetime

τ_{T_1} ranged from 500 to 3000 ns.[39] The value of k_{SF} also varies in different studies. In films of TIPS-Pn it is widely agreed that SF is fast, usually on a sub-picosecond timescale.[41,54,83] SF in NP form is slightly slower, with time constants on the order of 1–3 ps, which is to be expected from a more disordered system.[53,56,73] TIPS-Pn in solution has the slowest dynamics, with triplet formation occurring on a 100 ps time scale at high concentrations (0.075 molL^{-1}).[47] Additonally, two time components are often observed for SF rather than one. When this is the case the short component is typically less than 10 ps.[50,53,56,83] The wide variation of these parameters highlights the complexity of SF. Both the formation and decay of triplets depends on pathways that compete with SF, and how SF itself is modelled also affects the values obtained. To more comprehensively describe SF and add additional complexity to the model in Equation 2.8, we have considered the aspects outlined in the following sections.

Table 2.2: Examples of experimental time constants for TIPS-Pn. τ_{S_1} is the natural lifetime S_1, τ_{T_1} the lifetime of T_1, and τ_{SF} the time constant for SF. For TIPS-Pn films studied by Grieco et al.,[83] and in TIPS-Pn NPs, SF was fit with two time constants.

	Solution	Film	NP
τ_{S_1}	13 ns[47] 17 ns[39]	1.2 ns[a 38]	-
τ_{T_1}	6.5 µs[47]	2.1 µs[83] 80 ps[39]	954 ps[56]
τ_{SF}	∼100 ps[47]	0.1 ps[54] 0.11-0.21 ps and 2.26-5.1 ps[b 83] 0.08 ps[41] 0.08 ps[a 38]	2.9 and 169 ps[56] 0.22 and 1.37 ps[53]

[a] Data for crystalline pentacence film. [b] For TIPS-Pn films with a range of different preparation conditions.

2.8.1 Diffusion Limited SF

A study by Roberts et al. on disordered 5,12-diphenyl tetracene films found that SF in these films was diffusion limited.[50] They observed that the S_1 decay and corresponding T_1 rise occurred on two main time scales, one rapid and one slow. Fitting the evolution to a biexponential function, ∼50% of the T_1 rise and S_1 decay was described by an initial fast 1.3 ps time constant, and the rest with a slower 105 ps constant. This is explained by considering that SF is highly dependent on the relative orientations and separations of chromophores. In a disordered system such as the one studied by Roberts et al., it is likely some neighbouring molecules would have an orientation and separation favourable for SF, and others would not. Those with favourable geometry were referred to as "SF sites". After exciting the system, any singlet excitons near SF sites would rapidly undergo SF, resulting in the fast time constant observed. Excitons in other areas have to diffuse to these site to undergo SF. SF from these is thus delayed, giving the slow time component. This explanation is supported by quantum molecular dynamics and kinetic Monte Carlo simulations by Mou et al., which were able to reproduce the experimental data obtained by Roberts, and identify the SF sites in

this system as pairs of molecules with a twisted stack arrangement of the backbone π-orbitals, close proximity and with a high number of nearest neighbours.[51]

This diffusion-limited behaviour has been observed in a number of systems. The TIPS-Pn NPs studied by Tayebjee et al. exhibited biexponential decay in the time-resolved fluorescence, which the authors also attributed to two different S_1 populations.[56] Again one of the populations decayed rapidly, due to fast SF, and the other much slower due to the need to migrate to SF sites. The same has also been concluded in studies of thin films of terrylenediimide and films of 5,11-dicyano-6,12-diphenyltetracene by Margulies and coworkers.[59,87]

In terms of a rate model, this behaviour can be described by spitting the singlet excitons into two populations, those that are located on SF sites and therefore can undergo prompt SF, and those that require diffusion to SF sites. We refer to these populations as S_{SF} and S_D, respectively; i.e.

$$[S_1] = [S_D] + [S_{SF}].$$

Some S_{SF} is populated by the initial excitation, resulting in the fast SF fission observed, and the non-SF population, S_D, is then able to diffuse to available SF sites. This process can be modelled by

$$\begin{aligned}\frac{\mathrm{d}[S_D]}{\mathrm{d}t} &= -k_{S_1}[S_D] - k_D(t)[S_D],\\ \frac{\mathrm{d}[S_{SF}]}{\mathrm{d}t} &= -k_{S_1}[S_{SF}] + k_D(t)[S_D] - k_{SF}[S_{SF}].\end{aligned} \tag{2.9}$$

k_{S_1} is the rate constant for natural radiative S_1 decay, k_{SF} is the rate constant of SF, and $k_D(t)$ is the rate of diffusion of S_D excitons to a SF site. The diffusion of singlet excitons can be described by the Smoluchowski theory of diffusion-limited reactions.[90,91] If an exciton with a diffusion constant D diffuses to a single "activator", which traps or absorbs excitons with a trapping radius, R, the rate of diffusion to the activator, k_d, is given by

$$k_d(t) = 4\pi RD\left(1 + \frac{R}{\sqrt{\pi Dt}}\right). \tag{2.10}$$

If there are multiple activators that are far apart relative to the trapping radius, this rate is multiplied by their total number. In the context of SF, the activators are the SF sites, and the trapping radius, R, is the distance at which an exciton is considered to be "on" this site. This is equivalent to the maximum distance an exciton can be from a SF site and still undergo SF.[38,50] The rate of diffusion of S_D to S_{SF} is then given by

$$k_D(t) = 4\pi RDc_{SF}\left(1 + \frac{R}{\sqrt{\pi Dt}}\right), \tag{2.11}$$

where c_{SF} is the total number of singlet fission sites. Note that this expression is only valid if there are many more SF sites than excitons, such that c_{SF} can be considered constant.

The ranges of D and R depend on the morphology of the system studied. For the diphenyl tetracene films studied by Roberts et al., D was found to be 1.5×10^{-5} cm^2s^{-1} and R 0.43 nm.[50] In this system the phenyl groups hinder crystal growth, resulting in a disordered film. In contrast, diffusion in ordered tetracene crystals is much faster, with D reported as high as 4×10^{-2} cm^2s^{-1}.[92] In another study on an ordered system of microcrystalline pentacene films the fitted D and R are 5×10^{-4} cm^2s^{-1} and 1 nm, respectively.[38,93] In perylene crystals, D was found to be 5×10^{-5} cm^2s^{-1}.[94] The higher diffusion constant of crystalline tetracene suggests that the crystals are less susceptible to deformations. It is expected that in a system such as the TIPS-Pn/PMMA NPs studied here, the disordered arrangement and increased spacing will result in a much lower diffusion constant, around the same order as the disordered diphenyl tetracene films.

2.8.2 Singlet Exciton Trap Sites

A study by Marciniak et al. on SF in microcrystalline pentacene films modelled the SF process by including S_1 traps.[38] Typically, trap sites are sites with lower energies than their surroundings, such that once occupied, excitons lack the energy to hop out of them. Here we consider S_1 trap sites as sites where these excitons additionally cannot undergo SF. In highly crystalline materials, such as the films studied by Marciniak et al., these sites are caused by deformations or imperfections in the crystalline structure. Singlet trap sites have additionally been observed in materials such as thin films of 1,3-diphenylisobenzofuran,[64] and in more disordered systems such as TIPS-Pn NPs. The traps sites in TIPS-Pn NPs prepared by Tayebjee et al. were suggested to have arisen from a slow conversion of the morphology from an amorphous weakly coupled system, to one with strong coupling and more order.[56,73] In the case of more disordered systems, including the TIPS-Pn/PMMA NPs, we hypothesise that S_1 traps may also arise from particularly stable geometries or large intermolecular separations. These can be modelled as a separate population of S_1, to which excitons are allowed to migrate to, but not away from.

If we include the SF sites discussed above (section 2.8.1), the S_1 decay can now be expressed with a 3-population model:

$$
\begin{aligned}
[S_1] &= [S_D] + [S_{SF}] + [S_{trap}];\\
\\
\frac{d[S_D]}{dt} &= -k_{S_1}[S_D] - k_{trap}(t)[S_D] - k_D(t)[S_D];\\
\frac{d[S_{trap}]}{dt} &= -k_{S_1}[S_{trap}] + k_{trap}(t)[S_D];\\
\frac{d[S_{SF}]}{dt} &= -k_{S_1}[S_{SF}] + k_D(t)[S_D] - k_{SF}[S_{SF}].
\end{aligned}
\tag{2.12}
$$

Diffusion of S_D to trap sites can be described in the same way as SF sites:

$$
k_{trap}(t) = 4\pi R D c_{trap}\left(1 + \frac{R}{\sqrt{\pi D t}}\right),
\tag{2.13}
$$

where c_{trap} is the total number of trap sites in a NP. As with Equation 2.11, to apply this rate there must be many more trap sites than excitons.

2.8.3 Intermediate States

As discussed in Section 2.7, it is possible for the ^{1}(TT) state to be an observable intermediate. Recently, SF intermediates have been observed in systems such as crystalline pentacene,[57] crystalline tetracene,[58] films of terrylenediimide,[59] and covalently linked tetracene dimers.[60] In some cases this was identified as an excimer intermediate; an emissive state where an excitation is delocalised over a pair of molecules.[29,47,61–63] It is also thought that real or virtual charge transfer (CT) states could be involved in the formation of ^{1}(TT), so there may be multiple intermediate species as well.[45,57–59,66–68]

Regardless of the nature of the ^{1}(TT) intermediate, and how it is formed, the fact that it has previously been identifiable means it is important to include in SF models. If it is neglected, any spectral contributions from the ^{1}(TT) state will instead be attributed to other species. Mixing with the T_1 absorption, for example, can result in an overestimate of the T_1 concentration and consequently the SF yield.

If CT states act as a real intermediate to ^{1}(TT), it may also be beneficial to model their contribution and include an additional component in the kinetic model. But for now we consider this beyond the scope of this thesis (and as will be discussed in the results a fourth species is not necessary for an adequate fit to the experimental data).

To account for the possibility of an observable ^{1}(TT) state, and including SF and trap sites, Equation 2.7 can be modified to

$$\begin{aligned}
\frac{\mathrm{d}[\mathrm{S_D}]}{\mathrm{d}t} &= -k_{\mathrm{S_1}}[\mathrm{S_D}] - k_{\mathrm{trap}}(t)[\mathrm{S_D}] - k_{\mathrm{D}}(t)[\mathrm{S_D}];\\
\frac{\mathrm{d}[\mathrm{S_{trap}}]}{\mathrm{d}t} &= -k_{\mathrm{S_1}}[\mathrm{S_{trap}}] + k_{\mathrm{trap}}(t)[\mathrm{S_D}];\\
\frac{\mathrm{d}[\mathrm{S_{SF}}]}{\mathrm{d}t} &= -k_{\mathrm{S_1}}[\mathrm{S_{SF}}] + k_{\mathrm{D}}(t)[\mathrm{S_D}] - k_{\mathrm{SF}}[\mathrm{S_{SF}}];\\
\frac{\mathrm{d}[^1(\mathrm{TT})]}{\mathrm{d}t} &= k_{\mathrm{SF}}[\mathrm{S_{SF}}] - k_{\mathrm{diss}}[^1(\mathrm{TT})] - k_{^1(\mathrm{TT})}[^1(\mathrm{TT})];\\
\frac{\mathrm{d}[\mathrm{T}]}{\mathrm{d}t} &= 2 \times k_{\mathrm{diss}}[^1(\mathrm{TT})] - k_{\mathrm{T_1}}[\mathrm{T}].
\end{aligned} \tag{2.14}$$

k_{SF} now represents the rate constant at which excitons on SF sites form the ^{1}(TT) intermediate, and k_{diss} is the rate the ^{1}(TT) dissociates into individual separated triplets. We also consider the possibility of ^{1}(TT) decaying to the ground state instead of separating, with rate $k_{^1(\mathrm{TT})}$. All of the processes considered in this more complex model are described in Figure 2.8.

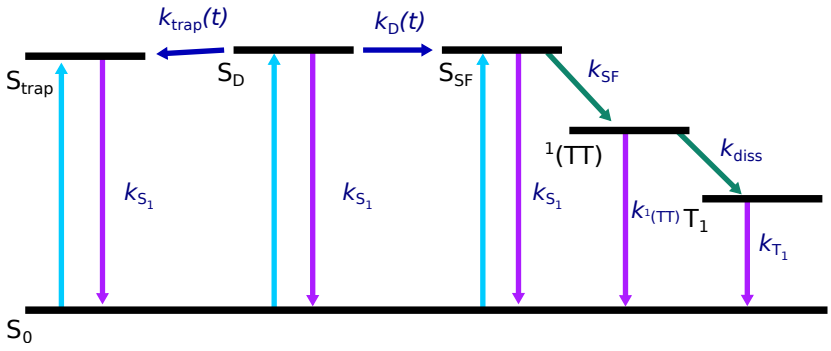

Figure 2.8: Schematic of SF including diffusion, singlet traps and triplet pair intermediate species.

As will be discussed in Chapter 5 of the results, the simple sequential model of S_1 to $^1(TT)$ to T_1 is unable to capture both a fast formation of T_1 and a long-lived component of $^1(TT)$. This also cannot be described by exciton diffusion, so to capture this we instead propose splitting $^1(TT)$ into two populations, $^1(TT)_A$ and $^1(TT)_B$.

$$[^1(TT)] = [^1(TT)_A] + [^1(TT)_B]$$

Similar to how the multiple S_1 populations allow a fast and a slow S_1 decay, one of the intermediate states, $^1(TT)_A$ can dissociate rapidly into a separated T_1, whilst the other slowly decays non-radiatively, giving a long lived component. Then, when S_{SF} undergoes SF, it forms either $^1(TT)_A$ or $^1(TT)_B$, with rate constants k_{SF_A} and k_{SF_B}, respectively, giving the modified model,

$$\begin{aligned}
\frac{d[S_D]}{dt} &= -k_{S_1}[S_D] - k_{trap}(t)[S_D] - k_D(t)[S_D];\\
\frac{d[S_{trap}]}{dt} &= -k_{S_1}[S_{trap}] + k_{trap}(t)[S_{trap}];\\
\frac{d[S_{SF}]}{dt} &= -k_{S_1}[S_{SF}] + k_D(t)[S_D] - (k_{SF_A} + k_{SF_B})[S_{SF}];\\
\frac{d[^1(TT)_A]}{dt} &= k_{SF_A}[S_{SF}] - k_{^1(TT)}[^1(TT)_A];\\
\frac{d[^1(TT)_B]}{dt} &= k_{SF_B}[S_{SF}] - k_{diss}[^1(TT)_B];\\
\frac{d[T_1]}{dt} &= 2 \times k_{diss}[^1(TT)_B] - k_{T_1}[T],
\end{aligned} \tag{2.15}$$

which is also represented by the flow diagram in Figure 2.9.

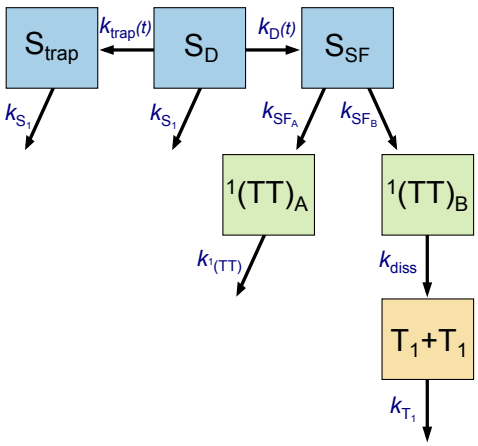

Figure 2.9: Flow diagram of the full kinetic model used to describe SF, given in Equation 2.15.

2.8.4 Fitting the Kinetic Model to Experimental Data

Fitting a kinetic model to the TA data involves first solving the series of coupled differential equations. If we model n populations, with time-dependent concentrations

$C_1(t), C_2(t), ...C_n(t)$, then the system of differential equations can be generalised as

$$\begin{aligned} \frac{\mathrm{d}C_1(t)}{\mathrm{d}t} &= f_1(t); \\ \frac{\mathrm{d}C_2(t)}{\mathrm{d}t} &= f_2(t); \\ &\vdots \\ \frac{\mathrm{d}C_n(t)}{\mathrm{d}t} &= f_n(t); \end{aligned} \tag{2.16}$$

where $f_1(t), f_2(t), ...f_n(t)$ are some functions of concentration and time. Given initial conditions this system can be solved using a 4th order Runge-Kutta algorithm.[95,96] The solutions, $C_1(t), C_2(t)...C_n(t)$ were then convoluted with the TA instrument response function (IRF), which was a Gaussian with a FWHM width of 0.15 ps (the instrument response time):

$$\mathrm{IRF}(t) = e^{-\left(\frac{(t-t_0)0.15}{2\ln 2}\right)^2}$$

The convoluted solutions, $(C_1 * IRF)(t), (C_2 * IRF)(t)...(C_n * IRF)(t)$ were then used to construct a fitted TA spectra:

$$\Delta\mathrm{A}_{\mathrm{fit}}(\lambda, t) = (C_1 * IRF)(t)\epsilon_1(\lambda)l + (C_2 * IRF)(t)\epsilon_2(\lambda)l + \ldots + (C_n * IRF)(t)\epsilon_n(\lambda)l$$

where ϵ_i is the extinction coefficient (or basis spectra) of population i. These were the same as the basis spectra determined in Section 2.7. Finally, the sum of squares of residuals between the fitted and experimental TA spectra were calculated as

$$\mathrm{SS}_{res} = \sum_t \sum_\lambda \left(\Delta\mathrm{A}_{\mathrm{fit}} - \Delta\mathrm{A}_{\mathrm{exp}}\right)^2.$$

The above is done iteratively, changing the rate constants and initial conditions of the kinetic equations until the sum of squares of residuals were minimised, using the `fmincon` function in Matlab.

2.9 Calculations

The methods for calculating the average intermolecular separation of TIPS-Pn molecules and their concentration in the NPs of various TIPS-Pn:PMMA mass ratios are outlined below. Additionally, in the kinetic fits of the TA and time-resolved fluorescence in Chapter 5, the value of the trapping radius, R, was calculated using a Poisson distribution and fitted values of c_{SF}, which is also outlined here.

2.9.1 Average Intermolecular TIPS-Pn Separation

The average intermolecular separation between TIPS-Pn molecules was estimated using the mass ratio between TIPS-Pn and PMMA, and their respective densities. If m_{PMMA} is the mass of PMMA in the nanoparticle and m_{TIPS} is the mass of TIPS-Pn, then for a NP with TIPS-Pn:PMMA mass ratio $1 : \alpha$,

$$m_{\mathrm{PMMA}} = \alpha m_{\mathrm{TIPS}}. \tag{2.17}$$

The total density of the NP, ρ_{Total} is given by the total mass of the nanoparticle $m_{\text{Total}} = m_{\text{PMMA}} + m_{\text{TIPS}}$ over the total volume of the nanoparticle $V_{\text{Total}} = V_{\text{PMMA}} + V_{\text{TIPS}}$,

$$\begin{aligned}\rho_{\text{Total}} &= \frac{m_{\text{Total}}}{V_{\text{Total}}} \\ &= \frac{m_{\text{TIPS}} + m_{\text{PMMA}}}{V_{\text{TIPS}} + V_{\text{PMMA}}}.\end{aligned} \tag{2.18}$$

Making use of the mass ratio we can then express this in terms of the densities of TIPS-Pn and PMMA, ρ_{TIPS} and ρ_{PMMA},

$$\begin{aligned}\rho_{\text{Total}} &= \frac{m_{\text{TIPS}} + \alpha m_{\text{TIPS}}}{V_{\text{TIPS}} + V_{\text{PMMA}}} \\ &= \frac{(1+\alpha)m_{\text{TIPS}}}{V_{\text{TIPS}} + V_{\text{PMMA}}} \\ &= \frac{(1+\alpha)\rho_{\text{TIPS}} V_{\text{TIPS}}}{V_{\text{TIPS}} + V_{\text{PMMA}}} \\ &= \frac{(1+\alpha)\rho_{\text{TIPS}}}{1 + \frac{V_{\text{PMMA}}}{V_{\text{TIPS}}}} \\ &= \frac{(1+\alpha)\rho_{\text{TIPS}}}{1 + \frac{m_{\text{PMMA}}\rho_{\text{TIPS}}}{\rho_{\text{PMMA}} m_{\text{TIPS}}}} \\ &= \frac{(1+\alpha)\rho_{\text{TIPS}}}{1 + \alpha\frac{\rho_{\text{TIPS}}}{\rho_{\text{PMMA}}}} \\ &= \frac{(1+\alpha)\rho_{\text{TIPS}}\rho_{\text{PMMA}}}{\rho_{\text{PMMA}} + \alpha\rho_{\text{TIPS}}}.\end{aligned} \tag{2.19}$$

If the average separation between evenly dispersed particles is d, then each particle can be surrounded by a cube of width d such that no other particles are in the box, as illustrated in Figure 2.10. Then we can approximate:

$$\begin{aligned}\frac{\text{Total Volume of Nanoparticle}}{\text{Number of TIPS-Pn molecules}} &\approx d^3 \\ \therefore d^3 &\approx \frac{V_{\text{Total}}}{N} \\ &= \frac{V_{\text{Total}}}{\frac{m_{\text{TIPS}}}{MW_{\text{TIPS}}} N_A} \\ &= \frac{V_{\text{Total}} MW_{\text{TIPS}}}{m_{\text{TIPS}} N_A} \\ &= \frac{V_{\text{Total}} MW_{\text{TIPS}}}{\rho_{\text{TIPS}} V_{\text{TIPS}} N_A} \\ &= \frac{MW_{\text{TIPS}}}{\rho_{\text{TIPS}} \frac{V_{\text{TIPS}}}{V_{\text{Total}}} N_A} \\ &= \frac{MW_{\text{TIPS}}}{\rho_{\text{TIPS}} \frac{m_{\text{TIPS}}\rho_{\text{Total}}}{\rho_{\text{TIPS}} m_{\text{Total}}} N_A}\end{aligned}$$

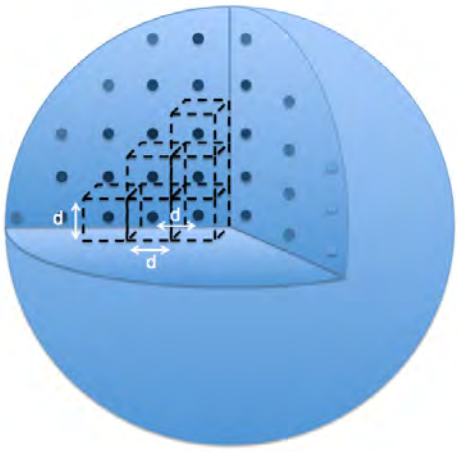

Figure 2.10: Evenly spaced TIPS-Pn molecules (represented by small spheres) inside a nanoparticle. Each molecule can be surrounded by a cube of width d, the average intermolecular distance between molecules, making the volume of that cube, which is approximately the volume of nanoparticle per TIPS-Pn molecule, d^3.

$$\begin{aligned} &= \frac{MW_{\text{TIPS}}}{\frac{m_{\text{TIPS}}}{m_{\text{Total}}}\rho_{\text{Total}}N_A} \\ &= \frac{MW_{\text{TIPS}}}{\frac{1}{\alpha+1}\rho_{\text{Total}}N_A} \\ &= \frac{MW_{\text{TIPS}}(\alpha+1)}{\rho_{\text{Total}}N_A}, \end{aligned} \tag{2.20}$$

where N is the number of TIPS-Pn molecules inside the nanoparticle, MW_{TIPS} is the molecular weight of TIPS-Pn, and N_A is Avogadro's number. Then using the expression for ρ_{Total} found before (equation 2.19) we have:

$$\begin{aligned} d^3 &\approx \frac{MW_{\text{TIPS}}(\rho_{\text{PMMA}} + \alpha\rho_{\text{TIPS}})}{\rho_{\text{TIPS}}\rho_{\text{PMMA}}N_A} \\ \therefore d &\approx \sqrt[3]{\frac{MW_{\text{TIPS}}(\rho_{\text{PMMA}} + \alpha\rho_{\text{TIPS}})}{\rho_{\text{TIPS}}\rho_{\text{PMMA}}N_A}}. \end{aligned} \tag{2.21}$$

Given $MW_{\text{TIPS}} = 639.07$ gmol^{-1}, $\rho_{\text{TIPS}} = 1.104$ gcm^{-3} and $\rho_{\text{PMMA}} = 1.188$ gcm^{-3} we obtain the average separations given in Table 2.3.

Table 2.3: Intermolecular separation between TIPS-Pn molecules determined for different TIPS-Pn:PMMA mass ratios (calculated using Equation 2.21) and the average concentration of TIP-Pn per NP (calculated using Equation 2.23).

TIPS-Pn:PMMA mass ratio (1:α)	Intermolecular TIPS-Pn separation (d) (nm)	Concentration of TIPS-Pn per NP (c_{total}) (molL^{-1})
1:0	0.99	1.73
1:0.5	1.12	1.18
1:1	1.23	0.90
1:3	1.54	0.46
1:5	1.76	0.31
1:7	1.93	0.23
1:10	2.15	0.17
1:20	2.66	0.09
1:100	4.49	0.02

2.9.2 Average Concentration of TIPS-Pn in a Nanoparticle

It is also possible to calculate the concentration of TIPS-Pn per NP. If the average separation between TIPS-Pn molecules is d, then the average volume occupied by 1 TIP-Pn is d^3. Then the number of TIPS-Pn molecules per volume is given by

$$\begin{aligned}\text{Number of TIP-Pns per volume} &= \frac{1}{\text{volume per TIPS-Pn}} \\ &= \frac{1}{d^3},\end{aligned} \tag{2.22}$$

and the TIPS-Pn concentration in a NP in molL^{-1} is given by

$$c_{\text{total}} = \frac{1}{d^3 N_A}, \tag{2.23}$$

where d is in dm. The concentrations per NP are given in Table 2.3.

2.9.3 Poisson Distribution to Determine Trapping Radius

In the kinetic fitting of the TA spectra of TIPS-Pn:PMMA NPs, the diffusion of singlet excitons to SF sites is given by the rate

$$k_{\text{D}}(t) = 4\pi R D c_{\text{SF}}\left(1 + \frac{R}{\sqrt{\pi D t}}\right), \tag{2.24}$$

where t is time, c_{SF} is the total concentration of SF sites in a NP, D is the diffusion constant and R is the maximum distance a singlet exciton can be from the center of a SF site and undergo SF, or the trapping radius. If we take a SF site to be two TIPS-Pn molecules separated by a maximum distance of d_{SF}, as shown in Figure 2.11, then $R = \frac{1}{2}d_{\text{SF}}$.

The value of c_{SF} obtained from kinetic fits to the TA spectra can be used to determine the proportion of TIPS-Pn molecules that are SF sites, $\frac{2 \times c_{SF}}{c_{\text{total}}}$, where c_{total} is

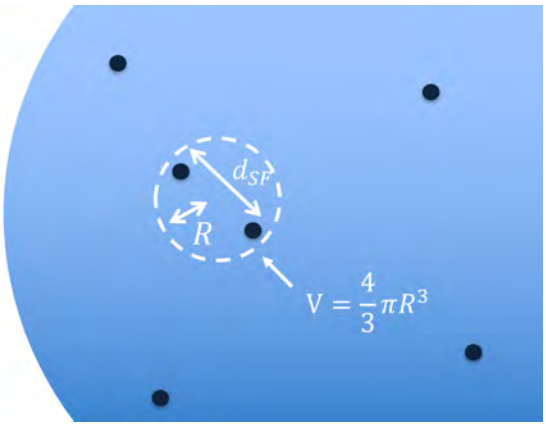

Figure 2.11: TIPS-Pn (blue circles) within a PMMA matrix NP. Define the maximum distance possible for SF as d_{SF} and the volume surrounded by the dashed line as the SF site.

the total concentration of TIPS-Pn in a NP (Table 2.3). Then the probability of two TIPS-Pn molecules having a separation possible for singlet fission is given by

$$P(\text{separation} \leq d_{\mathrm{SF}}) = \frac{2 \times c_{\mathrm{SF}}}{c_{\mathrm{total}}}. \tag{2.25}$$

If we then take a sphere of volume $V = \frac{4}{3}\pi d_{\mathrm{SF}}^3$ as in Figure 2.11, the probability of finding two or more TIPS-Pn molecules inside V is equivalent to the probability finding two TIPS-Pn molecules with a separation of d_{SF} or less,

$$P(\text{no. of pentacenes in V} \geq 2) = P(\text{separation} \leq d_{SF}) = \frac{2 \times c_{SF}}{c_{\mathrm{total}}}. \tag{2.26}$$

We assume the probability of observing k molecules inside V follows a poisson distribution,

$$P(k) = \frac{e^{-\lambda}\lambda^k}{k!}, \tag{2.27}$$

where λ is the average number of pentacenes in V,

$$\lambda = \text{no. pentacenes per volume} \times V = c_{\mathrm{total}} \times V. \tag{2.28}$$

Then we have

$$\begin{aligned} P(k \geq 2) &= 1 - P(k = 0) - P(k = 1) \\ &= 1 - e^{-\lambda}\frac{\lambda^0}{0!} - e^{-\lambda}\frac{\lambda^1}{1!} \\ &= 1 - e^{-\lambda} - e^{-\lambda}\lambda, \\ \therefore 1 - e^{-c_{\mathrm{total}}V} - e^{-c_{\mathrm{total}}V}c_{\mathrm{total}}V &= \frac{2 \times c_{SF}}{c_{\mathrm{total}}}. \end{aligned} \tag{2.29}$$

Given c_{SF} we can solve Equation 2.29 for V. Then

$$R = \frac{d_{\mathrm{SF}}}{2} = (\frac{3}{4\pi}V)^{\frac{1}{3}}. \tag{2.30}$$

CHAPTER 3
Characterisation of Aqueous TIPS-Pn/PMMA Nanoparticles

To determine the effect of intermolecular distance on SF, aqueous dispersions of mixed TIPS-Pn/PMMA nanoparticles were prepared with various different mass ratios. It is expected that each resulting particle will be a mixture of randomly arranged TIPS-Pn and PMMA, with proportions reflecting the mass ratios used to prepare them. The average intermolecular separation of TIPS-Pn in the NPs can thus be controlled by varying the mass ratio, with higher proportions of PMMA leading to larger intermolecular separations. In the following chapter we present evidence that the arrangement of TIPS-Pn in the NPs is random, and that TIPS-Pn and PMMA do not phase separate. We additionally outline some characteristic properties of the NPs, including size, stability in solution, steady-state absorption and steady-state fluorescence. For simplicity, each sample in this chapter will be referred to by its mass ratio. The convention is always TIPS-Pn:PMMA, and full details of the compositions can be found in Section 2.1 of Chapter 2.

3.1 Nanoparticle Formation

Aqueous dispersions of TIPS-Pn/PMMA NPs were prepared by the reprecipitation method, as outlined in Section 2.1 of Chapter 2. The resulting suspensions were a clear blue colour, as shown in Figure 3.1, with no visible aggregation. UV-visible absorption spectra were taken before and after filtration through 250 nm pores, with no change in absorption observed. This result confirms that nanoparticles less than 250 nm in size were formed, with no aggregation. The suspensions were stable as a colloidal suspension for a number of months, but some oxidation is observed after a few days. Details of NP stability and degradation are given in Section 3.5.

Figure 3.1: TIPS-Pn in THF (left) and TIPS-Pn NPs in water (right). Both have a concentration of $\sim 0.1\,\mathrm{g\,L^{-1}}$.

3.2 Nanoparticle Size

Scanning electron microscopy (SEM) images were taken to determine the size of the NPs, as described in Section 2.3. Approximately $0.001\,\mathrm{g\,L^{-1}}$ of neat TIPS-Pn NPs (with no surfactant) was passed through a filter (250 nm pores) directly onto a clean silicon wafer to reduce the presence of impurities from the sample vial and water. The resultant images are given in Figure 3.2 (a) and (b), showing evenly dispersed particles around 40 nm in size. To confirm the observed particles were the TIPS-Pn NPs and not impurities, water was kept in an identical sample vial and filtered onto another silicon wafer. The resultant SEM, Figure 3.2 (c), is featureless. Given the only differences between the two samples was the TIPS-Pn NPs, it follows that the particles in images (a) and (b) are TIPS-Pn. A single distribution of particle sizes was observed, as shown in Figure 3.3. The size distribution is consistent with the sizes of previously studied nanoparticles prepared by the same method.[53,56] Given that NPs of all TIPS-Pn:PMMA mass ratios studied were filtered through 250 nm pores with no change in maximum absorbance, these must also have an average diameter less than 250 nm.

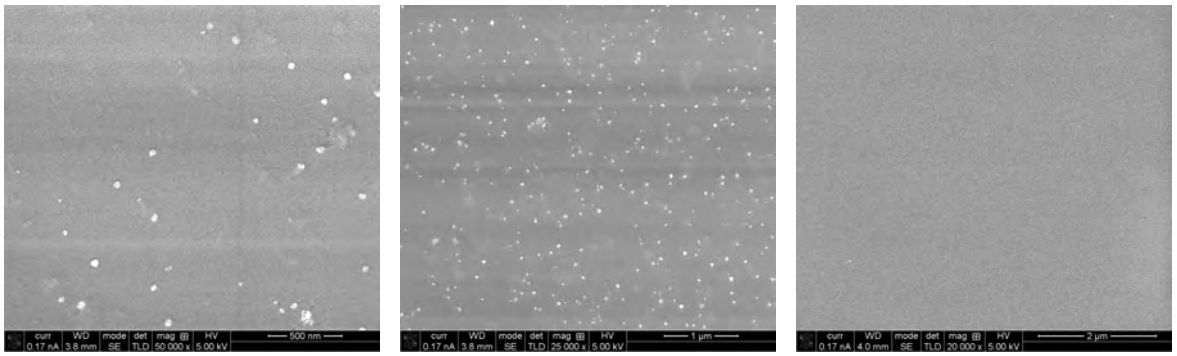

(a) NPs at 500 nm. **(b)** NPs at 1 µm. **(c)** Blank silicon wafer (coated with water instead of NP solution) at 2 µm

Figure 3.2: Scanning Electron Microscopy (SEM) images of neat TIPS-Pn NPs. (a) shows round particles around 40 nm in diameter and (b) shows the wider NP size distribution. The blank image in (c) confirms identity of NPs in images (a) and (b).

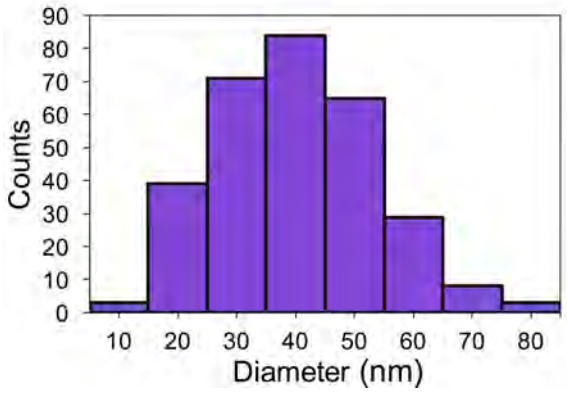

Figure 3.3: Size distribution of neat TIPS-Pn nanoparticles determined from SEM images.

3.3 Steady-State Absorption

The UV-visible absorption spectra of the different TIPS-Pn:PMMA mass ratios prepared are compared with TIPS-Pn in solution (THF) in Figure 3.4a. Previously, TIPS-Pn has been studied in crystalline forms, where the types of molecular packing and strength of coupling between molecules are reflected in the steady-state spectra. Aggregate features distinct from solution-phase ones have been observed in a number of studies of crystalline TIPS-Pn films,[39,47,74,83] as have similarly been observed for pentacene[38] and tetracene.[50] Crystalline domains of highly coupled brickwork packing have also been reported in NPs of TIPS-Pn, again resulting in a distinct spectral feature from solution.[56,73] In contrast, the spectra of the NPs in Figure 3.4 are nearly identical to the solution spectra, with no aggregate features, even after a number of days in storage (see Section 3.5 on NP stability). This result suggests weak electronic coupling between TIPS-Pns inside the NPs due to a highly amorphous arrangement, with negligible crystalline domain formation. We therefore assume that TIPS-Pn is randomly distributed inside the NP as represented in the illustration in Figure 3.5, where the dots represent TIPS-Pn molecules, randomly arranged in a PMMA matrix

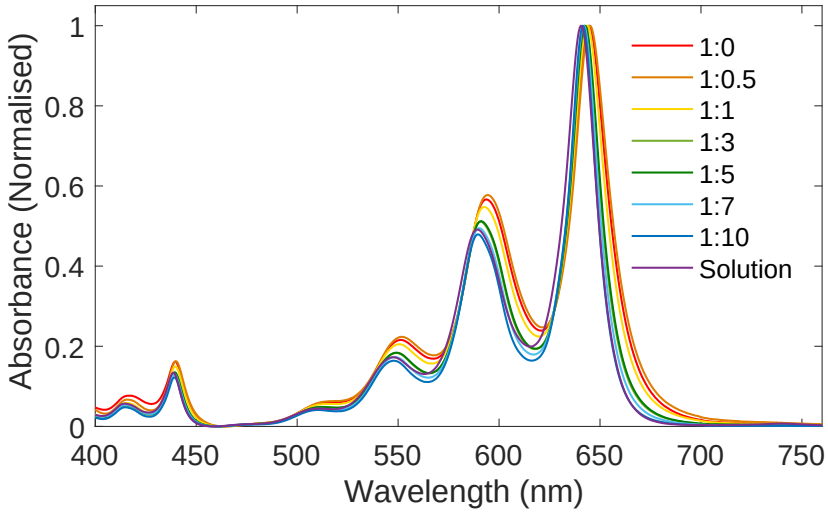

Figure 3.4: (a) UV-Vis spectra of NPs with different TIPS-Pn:PMMA mass ratios and pure TIPS-Pn in solution (THF). The similarity of the NP and solution spectra suggests that the TIPS-Pn molecules are not electronically coupled and are evenly dispersed as illustrated in Figure 3.5.

which constitutes the bulk of the NP. *

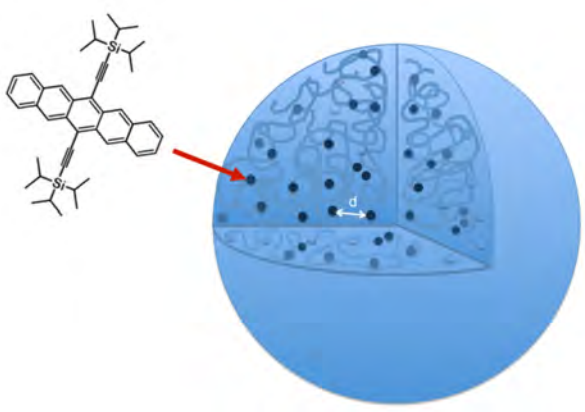

Figure 3.5: Illustration of randomly dispersed TIPS-Pn molecules with average intermolecular separation d, embedded in a PMMA NP. The TIPS-Pns are represented by dots and the PMMA chains constitute the bulk of the NP. For the 1:0 sample, no PMMA is present, so the NP is entirely TIPS-Pn.

Given this amorphous arrangement we can approximate the average center-to-center distance, or intermolecular separation, d, between neighboring TIPS-Pns in a NP, by using the mass ratio and the densities of TIPS-Pn and PMMA. The resultant separations are given in Table 3.1, with details of the calculations shown in the methods chapter (Section 2.9.1). Previous studies of neat TIPS-Pn NPs by Tayebjee et al. and Pensack et al. have also reported an amorphous arrangement based on similar

*It is also possible that the molecules could take a more clustered or left-skewed distribution, which could result in different average intermolecular separations than those calculated here. However, the overall trend with proportion of PMMA would be the same, so for simplicity we assume a purely random distribution.

Table 3.1: Range of different TIPS:PMMA mass ratios used to prepare NPs and the corresponding average intermolecular separation between TIPS-Pn molecules.

TIPS-Pn:PMMA Mass Ratio	Intermolecular Separation d (nm)
1:0	0.99
1:0.5	1.12
1:1	1.23
1:3	1.54
1:5	1.76
1:7	1.93
1:10	2.15

arguments.[53,56,73] It should be noted, however, that the NPs prepared by Tayebjee et al. eventually experienced a morphological evolution to a more strongly coupled system, with an additonal spectral feature at 700 nm.[56] This evolution was not observed here, likely due to subtle differences in the preparation procedure. A recent study by Pensack et al. was able to reproduce this evolution, and attributed it to co-precipitation with a chemical additive from the syringe used in NP preparation.[73] The lack of this additive in our preparation is likely the reason the morphology does not change.

The series of peaks at 650, 590 and 550 nm represent the $S_0 \rightarrow S_1$ 0–0, 0–1, and 0–2 vibronic transitions, and the smaller series from 440 nm represent the $S_0 \rightarrow S_2$ transitions.[97] The transitions become red shifted from those in solution as the proportion of PMMA is decreased, with the 1:10 TIPS-Pn:PMMA sample the least shifted and most solution-like. This supports the trend in intermolecular separations in Table 3.1, because as the proportion of PMMA increases, the molecules become more isolated and thus more solution-like. The largest redshift, of the 1:0 sample, was also observed in the amorphous NPs prepared by Tayebjee et al. and Pensack et al..

3.4 Steady-State Fluorescence

The steady-state fluorescence spectra of the samples are shown in Figure 3.6. After excitation at 590 nm, fluorescence was detected with a peak at ∼660 nm and a shoulder ∼700 nm, reflecting the 0–0 and 0–1 vibronic transitions. As the intermolecular spacing between TIPS-Pn is decreased, the fluorescence intensity decreases with negligible change in the spectral shape, and by the 1:1 sample is effectively quenched. This phenomenon is illustrated in Figure 3.6 (b), where the maximum fluorescence intensity approaches zero as separation is decreased. One possibility for this quenching is an increase in self absorption. When TIPS-Pns are more closely packed, an emitted photon has a higher probability of encountering another TIPS-Pn and being absorbed again, however it is unlikely that self-absorption would quench the fluorescence to the extent seen here. Another explanation is the increase of a non-radiative decay pathway that competes with fluorescence, such as singlet fission (SF).

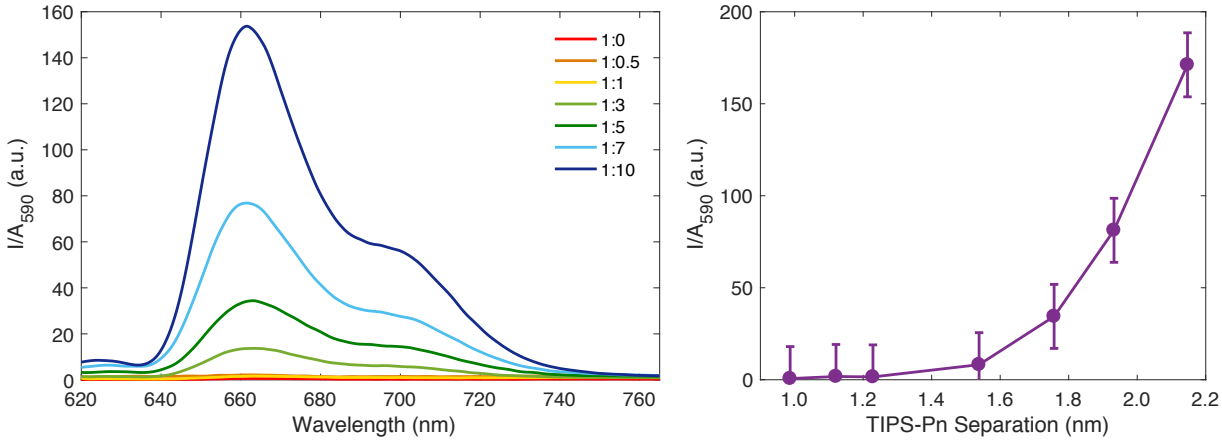

(a) **(b)**

Figure 3.6: (a) Steady-state fluorescence of TIPS-Pn/PMMA NPs. (b) Variation of the maximum fluorescence intensity as a function of average intermolecular TIPS-Pn separation. The fluorescence was divided by absorption at the 590 nm peak to account for various concentrations.

3.5 Degradation and Colloidal Stability

It is important that the TIPS-Pn/PMMA NPs do not aggregate or degrade in the time period they are studied. To illustrate the colloidal and chemical stability of the NPs, Figure 3.7 shows the steady-state absorption spectra of the 1:0 and 1:10 samples at 6.5 and 31 weeks after preparation, respectively. The samples were also refiltered through 250 nm pores to check for aggregation, with the spectra shown on the same axes. After 6.5 weeks the absorbance of the 1:0 sample was 60% lower than when it was first prepared. However, the spectra of the filtered and unfiltered samples are identical, implying no significant aggregation had occurred. The decrease is therefore due to the degradation of the TIPS-Pn molecules rather than the nanoparticles aggregating. This is additionally accompanied by an increase in absorbance below 450 nm, implying the formation of a new species. TIPS-Pn has previously been described to degrade under ambient conditions by reacting with oxygen to form endoperoxides.[98–100] The 6,13-endoperoxide of TIPS-Pn has been identified as the main product of this reaction, which has no visible absorption, however, 5,14-endoperoxide is also formed in small quantities and is known to absorb below 450 nm, which accounts for the increase in absorption there.[100] This is distinct from the spectral features observed in crystalline TIPS-Pn, so we conclude that no morphological evolution of TIPS-Pn occurs, and the arrangement in the NP stays amorphous. The 1:10 sample only degraded by 20% over 31 weeks, and similarly no aggregation was observed. The increased chemical stability of this sample could be due to the surrounding PMMA chains limiting the contact of TIPS-Pn with dissolved oxygen in solution, however an alternative explanation could be a reduced amount of SF. TIPS-Pn triplets react with oxygen triplets to form endoperoxides, so less SF in the 1:10 sample would lead to less triplets and thus less degradation. This could be confirmed by replacing TIPS-Pn with a material that undergoes intersystem crossing to form triplets rather than SF, but this is beyond the scope of this thesis.

The degradation discussed here occurs on a much longer timescale than what was needed for spectroscopy experiments, but, to minimise the effect of degradation, samples were used within 24 hours of preparation, and the absorption spectra taken be-

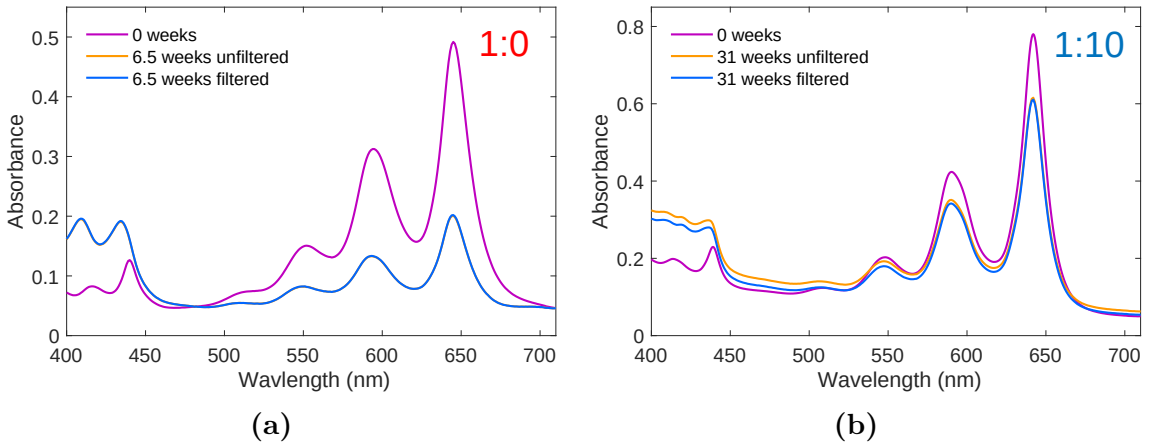

(a) **(b)**

Figure 3.7: Oxidation and colloidal stability of the TIPS-Pn/PMMA NPs. (a) 1:0 sample over 6.5 weeks. (b) 1:10 sample over 31 weeks. The 1:0 sample degrades significantly more than the 1:10, but neither samples aggregate (in the 1:0 case the unfiltered and filtered 6.5 week spectra are coincident).

fore and after experiments. After transient absorption and fluorescence experiments (roughly 90 minutes of laser exposure) absorption was only observed to decrease by 5% or less.

3.6 Conclusions

To summarise, it has been demonstrated that TIPS-Pn/PMMA NPs of mass ratios ranging from 1:0 to 1:10 TIPS-Pn:PMMA are able form colloidal suspensions in water that are stable for a number of weeks. The size of the neat 1:0 NPs was around 40 nm in diameter, and the remaining samples are expected be similar, with a diameter at least less than 250 nm. Further SEM experiments are required to confirm the actual size, but in any case this should not significantly affect any of the optical process studied. For one, the average intermolecular TIPS-Pn separation is independent of NP size, and additionally, the exciton diffusion length is much smaller than 40 nm. With regards to the morphology of the NPs, the visible absorption spectra of TIPS-Pn in the NPs are nearly identical to TIPS-Pn in solution, indicating that no crystalline domains are present and that the distribution of TIPS-Pn molecules is random. Additionally the gradual blue shift as proportion of PMMA is increased indicates the NPs are becoming more isolated. As such for the remainder of this thesis we take the average intermolecular separations as those calculated in Chapter 2. Lastly the steady-state fluorescence of the NPs is quenched as proportion of PMMA, or intermolecular separation is decreased. This is potentially due to an increase in the rate of SF.

CHAPTER 4
Spectroscopic Analysis of Singlet Fission in TIPS-Pn/PMMA Nanoparticles

The TIPS-Pn/PMMA nanoparticles described in Chapter 3 are a useful system to study the occurrence of singlet fission (SF). TIPS-Pn is known to undergo SF with high efficiencies.[41,47,53,54,56,83] By controlling the intermolecular separation of TIPS-Pn molecules in a NP, we can investigate the effect of distance on the dynamics of SF and related processes. In this chapter, ultrafast time-resolved spectroscopic techniques are used to study the evolution of excited states in different TIPS-Pn:PMMA NPs on fs to ns timescales. Initially time-resolved fluorescence is used to trace the lifetime of the excited singlet population, and then transient absorption measurements are used to elucidate the presence of triplets. Two systems where SF does not occur are also studied, a 1:100 TIPS-Pn:PMMA sample and a dilute TIPS-Pn solution in toluene. This allows the characteristics of the excited singlet state in a NP environment to be determined, in order to separate them from the triplet in the TA. The data can then be resolved into the respective contributions from each excited-state population, and the concentrations of these populations determined as a function of time, without the need to assume any specific kinetic model.

4.1 Time-resolved Fluorescence

In Section 3.4, the steady-state fluorescence of TIPS-Pn/PMMA NPs was observed to decrease with decreasing TIPS-Pn intermolecular separation. To investigate the source of this behaviour, the decay kinetics of the 655 nm fluorescence peak was monitored using time-resolved fluorescence upconversion (UC) spectroscopy, as described in Chapter 2 (Section 2.4). The UC data are plotted together over 300 ps and 25 ps in Figure 4.1, and each time-resolved trace is shown individually in Figure 4.2 fitted to the sum of exponentials $I(t) = \sum_n A_n \exp(-t/\tau_n)$ and convoluted with a Gaussian 0.45 ps instrument response function. The parameters for these fits are given in Table 4.1. Each fluorescence decay is able to be fit with 3 or fewer exponentials ($n \leq 3$) with fast, intermediate and slow decay time constants, τ_1, τ_2, and τ_3, respectively.

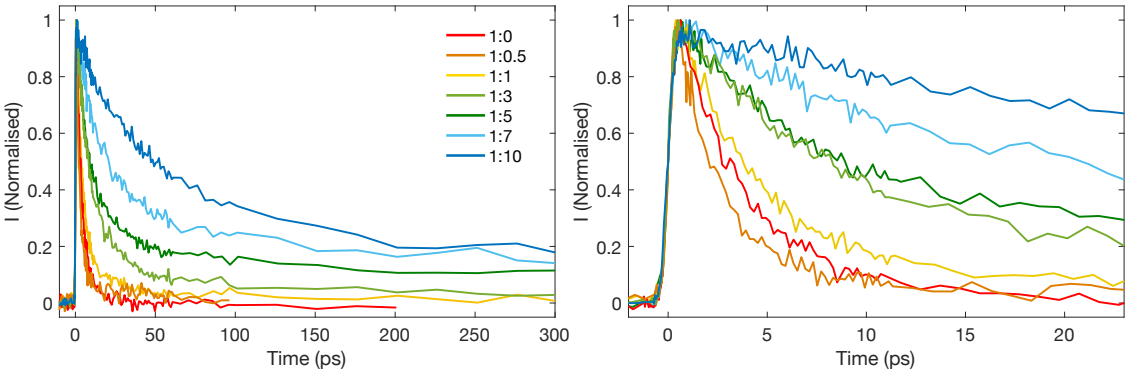

Figure 4.1: Time-resolved fluorescence upconversion data of NPs after 440 nm excitation (a) over 300 ps and (b) over the first 25 ps.

Table 4.1: Fitting parameters for the fluorescence UC data of TIPS-Pn:PMMA NPs.[a]

sample	A_1 [b]	τ_1 (ps)	A_2	τ_2 (ps)	A_3	τ_3 (ps)[c]
1:0	1.00	3.9±0.2	–	–	–	–
1:0.5	0.94±0.03	2.2±0.2	0.06±0.03	40±30	–	–
1:1	0.89±0.03	3.9±0.3	0.11±0.04	40±20	–	–
1:3	0.84±0.04	8.7±0.6	0.15±0.04	90±40	0.01±0.01	12000
1:5	0.79±0.01	9.1±0.4	0.19±0.01	430±90	0.02±0.01	12000
1:7	0.71±0.02	18±1	0.24±0.02	500±100	0.06±0.01	12000
1:10	0.71±0.06	48±6	0.17±0.06	400±200	0.13±0.01	12000

[a] Data fitted to a multi-exponential function $f(t) = \sum_n A_n e^{-t/\tau_n}$ with an instrument response time of 0.45 ps. Unconstrained parameters are shown with a 90% confidence interval. [b] Amplitudes normalized so $\sum_n |A_n| = 1$. [c] Fixed to natural singlet lifetime obtained from TCSPC measurements.

As the UC measurements were limited to a ~2.5 ns window, the ns-scale dynamics of the samples' fluorescence decay was obtained using time-correlated single photon counting (TCSPC), as described in Section 2.5. Fits to the TCSPC data of the NP samples are shown in Figure 4.3, with fit parameters in Table 4.2. In addition to the

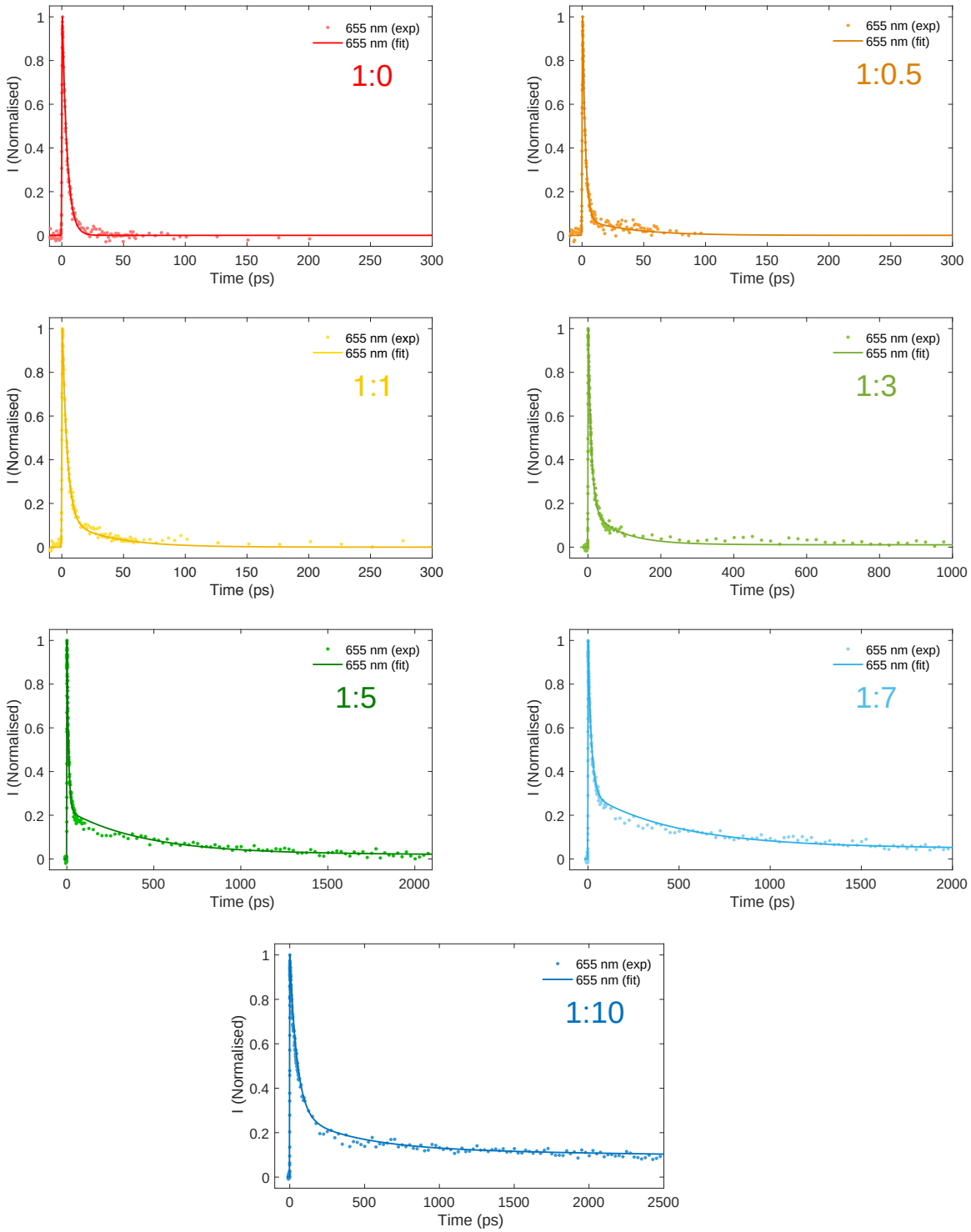

Figure 4.2: Fluorescence UC data for the TIPS-Pn:PMMA NPs. All samples fit to a sum of exponentials with a long time component of 12 ns. Fit parameters are given in Table 4.1.

NP samples, a 10^{-5} M TIPS-Pn solution in toluene was measured (Figure 4.4), which is sufficiently dilute to assume negligible intermolecular interactions between TIPS-Pn molecules over the duration of the experiment.[47] Because there are no additional singlet decay pathways in this sample, such as SF, the decay of the solution TIPS-Pn fits to a single exponential with a time constant of $\tau = 12\,\text{ns}$. This is assigned to

the intrinsic singlet lifetime, in good agreement with other studies of TIPS-Pn.[39,47] This lifetime also matches the slowest decays observed in the TCSPC measurements of the NPs, thus we have used it to constrain the long time constants in the fits of the time-resolved fluorescence data. This is particularly necessary for the UC data as the experimental time window is much shorter than the natural singlet lifetime. The two shorter time components of the UC data, τ_1 and τ_2, were fit without constraints. As the proportion of PMMA is increased, the fluorescence becomes significantly more long lived, which is reflected in the fit parameters. Given the only fluorescent species present is the S_1 state, this indicates a decrease in S_1 lifetime due to the presence of nonradiative decay pathways, which become more dominant as the TIPS-Pn intermolecular separation decreases. Only the neat 1:0 NP sample is able to be fit with a single, fast exponential with $\tau_1 = 3.9\,\text{ps}$. The other TIPS-Pn:PMMA blend NPs require a second exponential with an intermediate time constant τ_2, indicating the presence of a second type of nonradiative decay pathway, or a second population of singlet excitons.[50,56] As the proportion of PMMA, and hence intermolecular separation, increases, the amplitude of this intermediate time constant grows, as does the natural singlet decay, τ_3. τ_1 consequently becomes less dominant, and both τ_1 and τ_2 also become slower with increased separation. This change in fluorescence lifetimes confirms that the quenching of steady-state fluorescence is due to non-radiative decay pathways, rather than self-absorption (which would decrease the magnitude of fluorescence at all times, not the lifetime). As the instrument response function of the TCSPC data is so slow (60 ps), it is not used to make any significant conclusions about trends in the lifetimes of the NPs other than τ_3, which, as with UC, increases in amplitude with intermolecular separation.

There is a slight inconsistency in the general trend, as can be seen from the raw UC data of the 1:0 and 1:0.5 samples in Figure 4.2 (b). The 1:0.5 sample has a faster τ_1 than the 1:0 sample and can be seen to decay faster until $\sim$10 ps. Because the proportion of PMMA in this sample is so small, the intermolecular distance for 1:0 and 1:0.5 are very similar, and the difference between decay time constants is within experimental error.

Finally, TCSPC data is also given for a 1:100 TIPS-Pn:PMMA sample in Figure 4.4a. This sample was additionally included for the the purposes of obtaining a pure singlet TA spectrum, as discussed in Section 4.3. Because of the large TIPS-Pn separation in this sample ($\sim$5 nm) it is expected that no SF would occur. Similar to the dilute solution (Figure 4.4b), the TCSPC of this sample shows a single 12 ns exponential decay, confirming this is in fact the case.

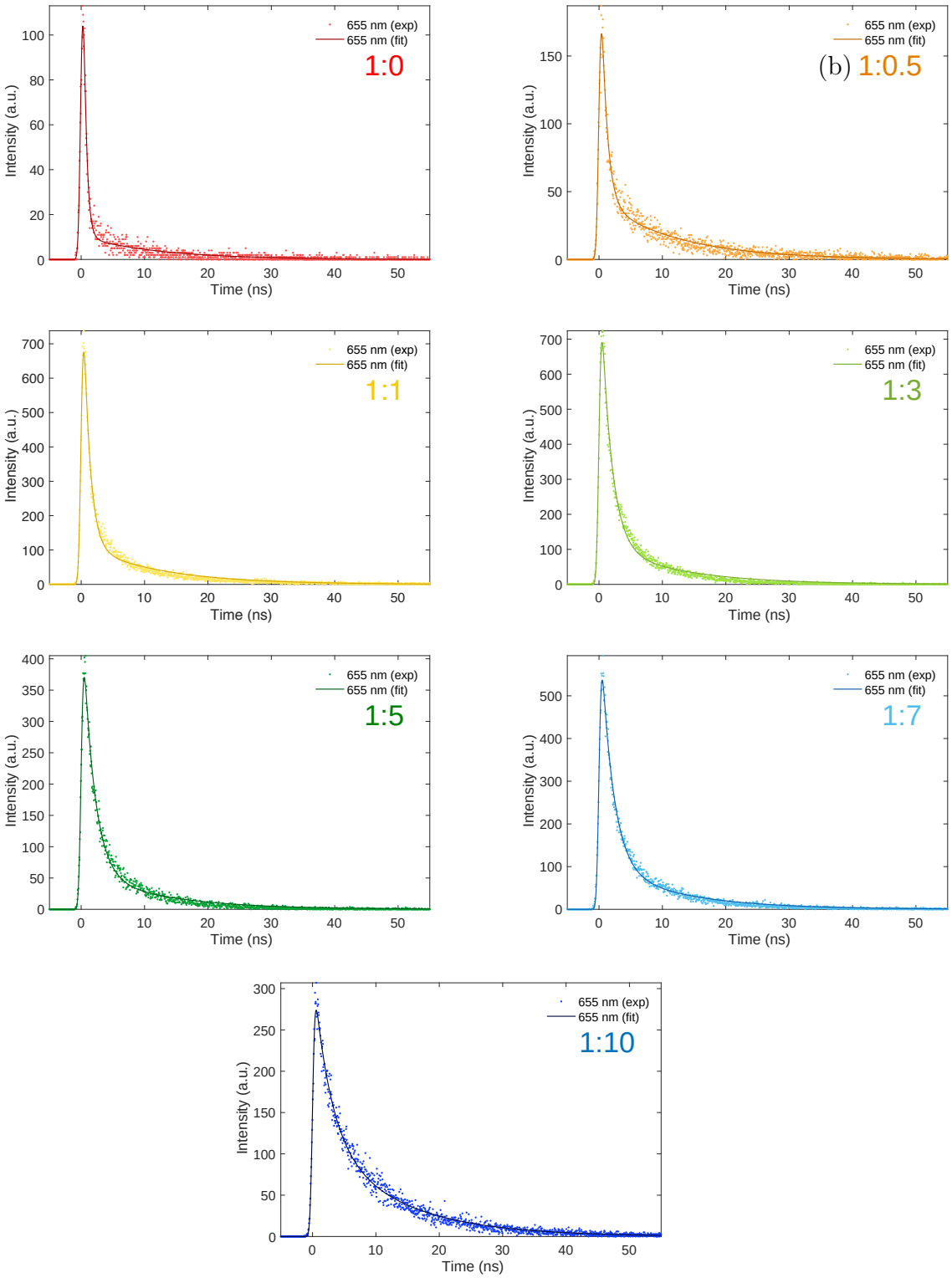

Figure 4.3: TCSPC data for the TIPS-Pn:PMMA nanoparticles. All samples fit to a sum of exponentials with a long time component of 12 ns. Fitting parameters are given in Table 4.2.

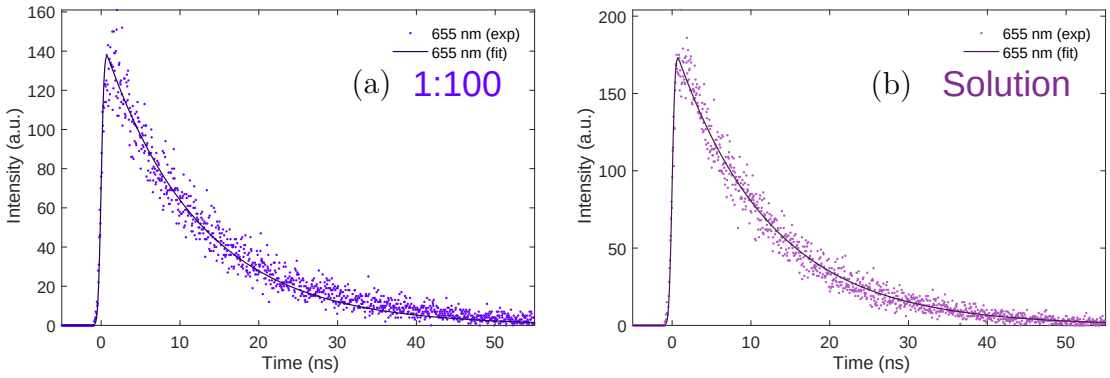

Figure 4.4: TCSPC data for (a) 1:100 ratio TIPS-Pn:PMMA nanoparticles and (b) 10^{-5} M TIPS-Pn solution in toluene. Both samples are fit to single-exponential decay with a time constant of 12 ns.

Table 4.2: Fitting parameters for the TCSPC data, including the fits for 10^{-5} M TIPS-Pn solution in toluene, and the 1:100 sample of NPs.[a]

sample	A_1 [b]	τ_1 (ns)	A_2	τ_2 (ns)
1:0	0.97±0.09	0.46±0.02	0.03±0.002	12
1:0.5	0.85±0.07	0.90±0.05	0.15±0.002	12
1:1	0.90±0.02	1.01±0.03	0.10±0.002	12
1:3	0.88±0.01	1.63±0.04	0.117±0.004	12
1:5	0.88±0.01	1.77±0.05	0.119±0.01	12
1:7	0.86±0.01	1.91±0.05	0.145±0.01	12
1:10	0.61±0.02	2.7±0.2	0.394±0.01	12
1:100	–	–	1.00	12
solution	–	–	1.00	12

[a] Data fitted to a multi-exponential function $f(t) = \sum_n A_n e^{-t/\tau_n}$ with an instrument response time of 0.6 ns. Unconstrained parameters are shown with a 90% confidence interval. [b] Amplitudes normalised so $\sum_n |A_n| = 1$.

4.2 Transient Absorption Spectroscopy

To investigate the origin of the non-radiative decay observed in time-resolved fluorescence, transient absorption (TA) spectra were collected over 460–800 nm, exciting the $S_0 \rightarrow S_2$ transition at 440 nm. Previous time-resolved studies of TIPS-Pn have shown the excitation energy has minor impact on exciton dynamics and decay products, as the $S_2 \rightarrow S_1$ relaxation occurs rapidly.[66] Based on the energy gap law this should be on the order of less than 100 fs,[101,102] which is faster than the 150 fs instrument response time of the TA spectrometer. We observed minimal differences in TA dynamics when instead exciting the $S_0 \rightarrow S_1$ transition at 590 nm, as shown in Appendix 4.5.2. Full TA spectra are given in Figures 4.5, 4.6, and 4.7, and details of the TA collection are outlined in Section 2.6. Before discussing the features of the 1:0 to 1:10 NP spectra in depth, it is first useful to compare the spectra of two different samples, a 10^{-4} M TIPS-Pn solution in toluene, and a 1:100 TIPS-Pn:PMMA NP sample (Figure 4.5).

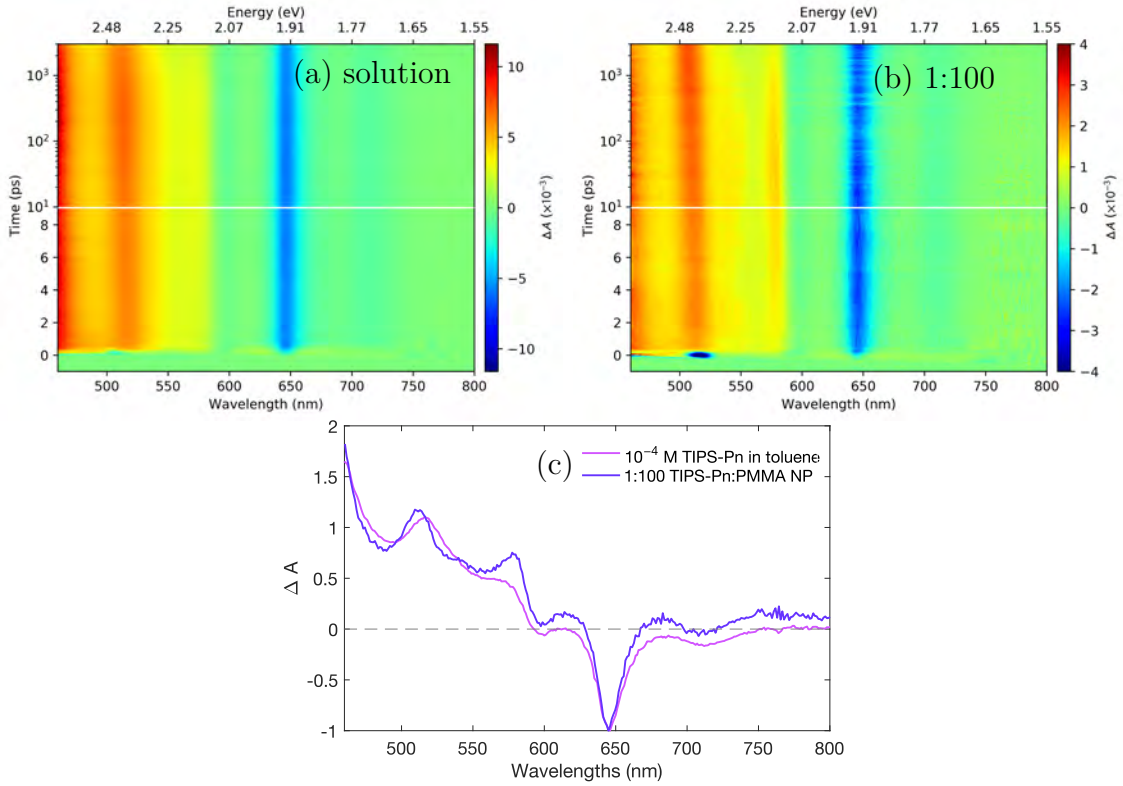

Figure 4.5: TA spectra of (a) 10^{-4} mol L^{-1} TIPS-Pn solution in toluene and (b) 1:100 ratio TIPS-Pn:PMMA NPs. Spectra in (c) show the ΔA at 10 ps for each sample, normalized to the signal at 650 nm. 1:100 NP TA was collected in a 1 cm path-length cuvette due to its low TIPS-Pn concentration, and the 10 ps ΔA was averaged over many scans.

As mentioned in Section 4.1, it has been shown that the the separation between TIPS-Pn molecules in a 10^{-4} M solution is sufficiently large that intermolecular interactions are negligible, and the transient absorption signal can thus be considered that of the pure singlet.[47] The 1:100 sample should have intermolecular separations large enough that the effect is the same. The features of the 1:100 TA spectra match those of the dilute solution extremely well, suggesting this is the case (Figure 4.5c). The subtle differences that are present between the two spectra can be attributed to the different environments (PMMA vs toluene).

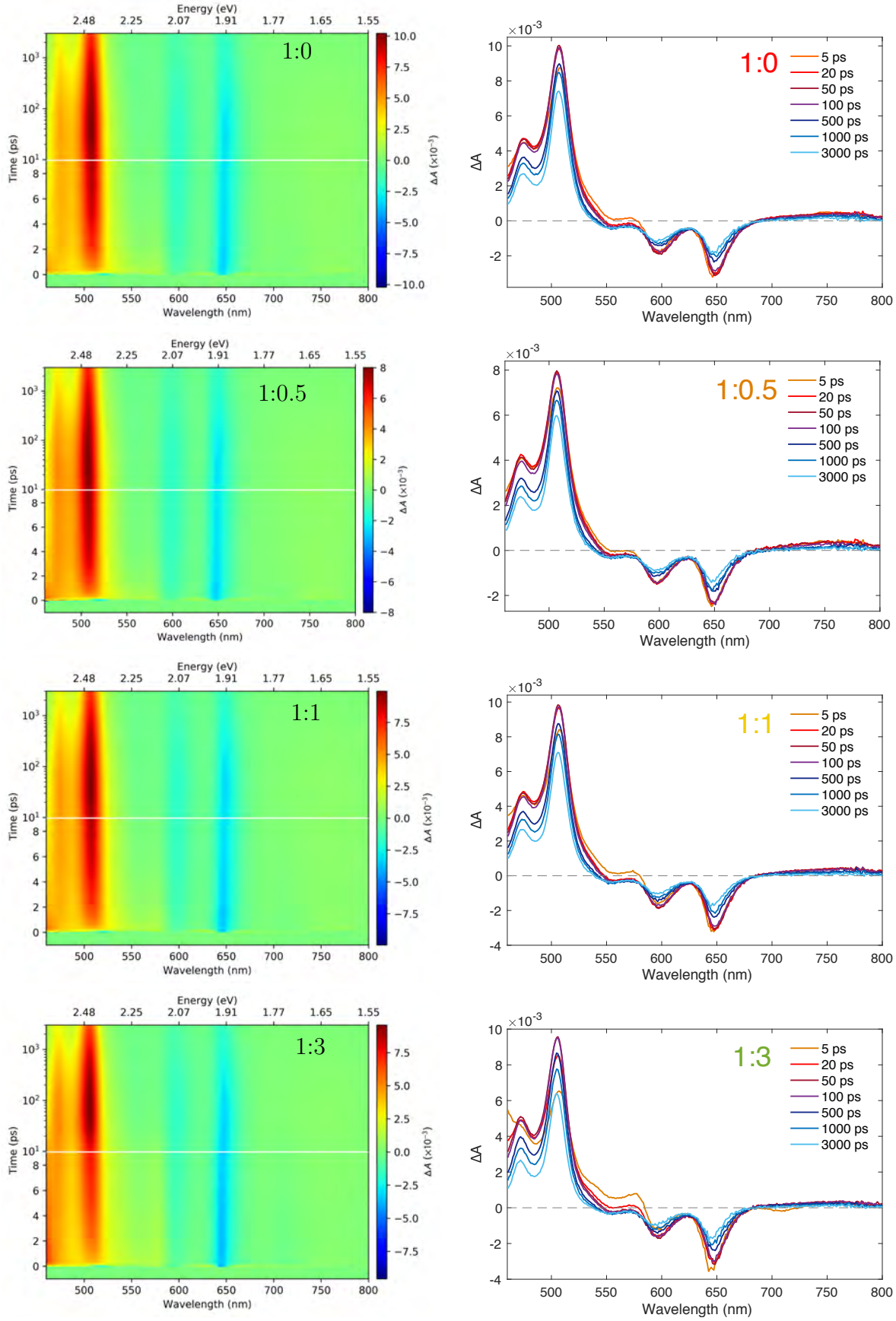

Figure 4.6: Transient absorption data for the 1:0 to 1:3 TIPS-Pn:PMMA nanoparticles. The full three dimensional data are shown on the left, and the spectra are sampled at various times on the right.

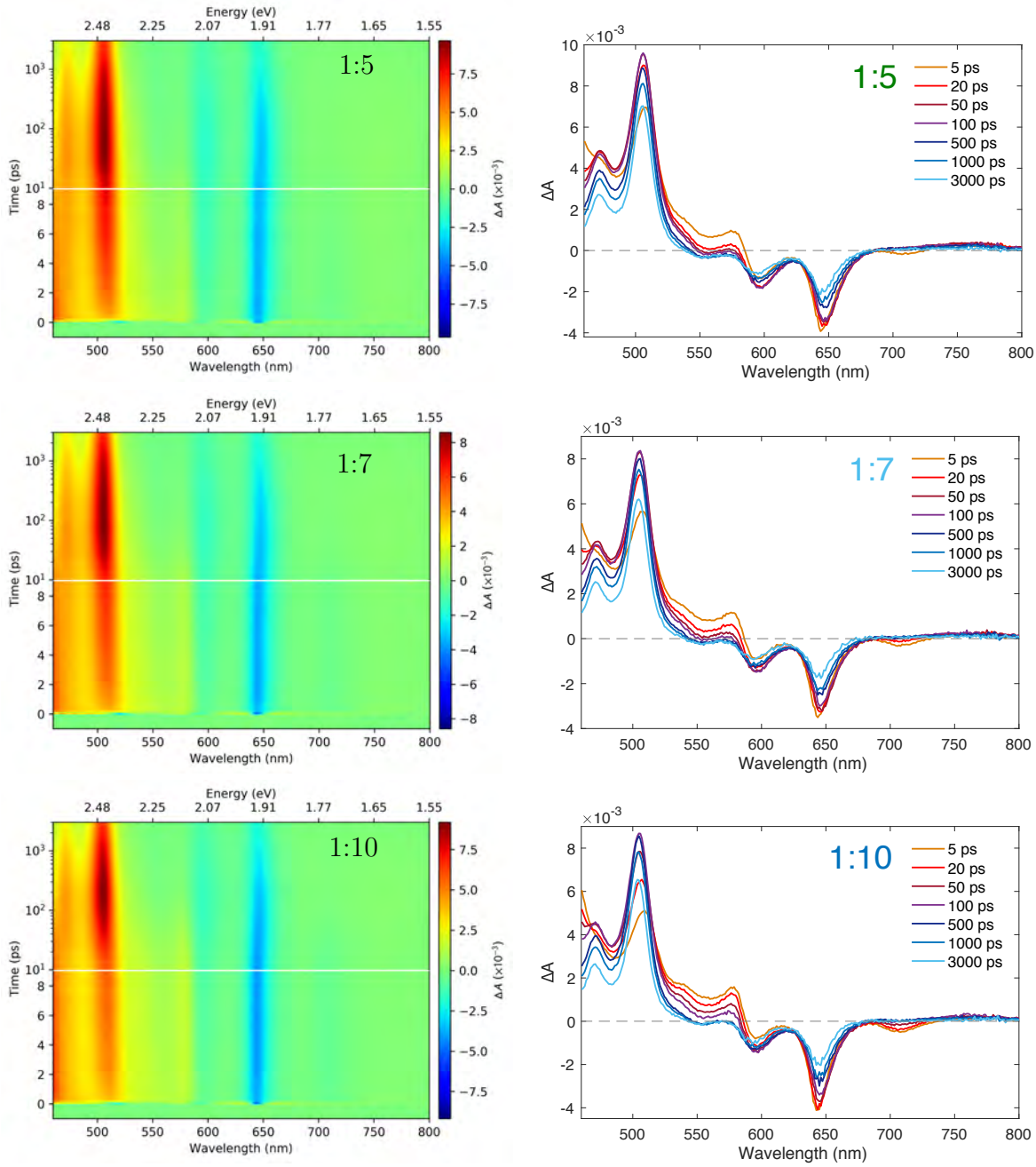

Figure 4.7: Transient absorption data for the 1:5 to 1:10 TIPS-Pn:PMMA nanoparticles.

For the other NP samples (Figures 4.6 and 4.7), a negative ground-state bleach (GSB) signal is observed at ∼650, 600 and 550 nm, matching the $S_0 \rightarrow S_1$ 0–0, 0–1 and 0–2 vibronic transitions seen in the steady-state absorption spectra of Section 3.3 (Figure 3.4). There appears to be some overlap of these bleach bands with the strong excited state absorption (ESA) signals which dominate the 450–600 nm spectral window. These positive ESA signals comprise more than one spectral component. Most obvious at early times, and in the higher-ratio samples, is an absorption exhibiting peaks around 450, 505 and 575 nm, and accompanied by a negative stimulated emission (SE) signal around 710 nm. The lifetimes of these features are consistent with the time-resolved fluorescence data, and are attributed to $S_1 \rightarrow S_n$ transitions, in agreement with previous studies.[39,47,53,56] They also match the features of the pure singlet spectra in

the 1:100 NP sample (Figure 4.5).

An additional ESA with peaks centered around 475 and 510 nm rises over 10s of ps, and decays at a rate much slower than that of the singlet, dominating the spectra over the latter part of the 3 ns experimental time window. This absorption is characteristic of the TIPS-Pn $T_1 \rightarrow T_3$ transition,[29,54] indicating the production of triplet excitons.[39,53,56] Given the appearance of the triplet signal occurs much faster than the rate of $S_1 \rightarrow T_1$ intersystem crossing, we attribute the nonradiative decay of singlets observed in the time-resolved experiments to triplet production via SF.[47]

As the TIPS-Pn intermolecular separation increases, there is a decrease in the rate of formation of triplets and concurrent decay of singlet ESAs. In the TA spectrum of the 1:0 NP (Figure 4.6), a well-defined $T_1 \rightarrow T_3$ peak is present by 5 ps, with minimal features of the singlet exciton. In contrast, for the 1:10 NP sample, at 5 ps the spectral shape differs significantly, with relatively weak triplet ESA and obvious singlet exciton presence. These trends are consistent with the increase in long-lived signal in the fluorescence UC data (Figure 4.2, Table 4.1), and demonstrate the reduced rate of singlet fission as TIPS-Pn separation increases.

To highlight the difference in SF rates with separation, Figure 4.8 shows the TA at 5 ps for all the TIPS-Pn:PMMA ratios.

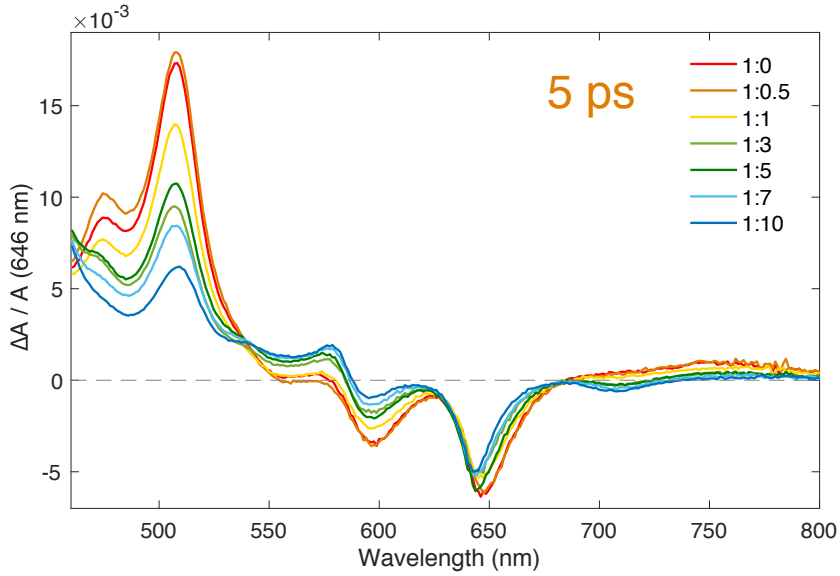

Figure 4.8: TA spectra at 5 ps for different TIPS-Pn:PMMA mass ratio NPs. The shape of the spectra at early times is significantly different for the different TIPS-Pn separations.

Two isosbestic points are present at 540 and 670 nm, characteristic of the conversion from one kinetic species to another. As the proportion of PMMA, and hence TIPS-Pn separation, decreases (blue to red lines), the triplet-dominated region around 507 nm increases and the singlet ESA decreases, indicating a faster conversion from singlets to triplets for the smaller separations. The isosbestic point at 670 nm similarly shows the increase in magnitude of the GSB region with a decrease in intensity of the SE at 710 nm, indicative of the effects of exciton multiplication by SF. The strengthening of the broad ESA band around 750 nm as singlet excitons are depleted is worth noting. While there is some overlap with the SE at 710 nm, the appearance of this feature does not directly correspond with either the observed singlet exciton decay, nor the growth of the triplet ESA peaks, suggesting another component may be present. This will be

discussed further in Section 4.3.2.

It should be noted that there is significant overlap of the $T_1 \rightarrow T_3$ and $S_1 \rightarrow S_3$ ESA around 475–525 nm, and of the $S_1 \rightarrow S_3$ ESA and the GSB features around 550–625 nm. Additionally, the observed SE signal at 710 nm corresponds to the weaker 0–1 shoulder in the steady-state fluorescence (Figure 3.6a, Chapter 3), implying there must also be a significant 0–0 SE component to the negative signal band around 650 nm, overlapping the GSB. Hence it is not reliable to use solely the magnitudes of the GSB or ESAs to quantitatively analyze SF rates or yields, although some previous studies of SF have attempted to do so.

4.3 Spectral Deconvolution of Transient Absorption Spectra

Because of the extent of overlap of the different features in the TIPS-Pn TA spectra, there are no regions that can be solely assigned to S_1 or T_1, and thus no single wavelengths can be used as a kinetic trace for either population. To extract the kinetics from the TA data, the spectra need to be resolved into its respective components, or "basis spectra" following the nomenclature of Roberts et al.[50] The TA spectra can then be fit to a linear combination of the basis spectra, and the concentrations of each component obtained as a function of time. To avoid confusion with the concentrations given by fitting a kinetic model to the data in Chapter 5, we refer to the fits obtained from this method as "spectral fits". The details of the extraction of basis spectra and subsequent spectral fitting are described in detail in Section 2.7. Here, we only justify the times and samples chosen to determine the basis spectra.

To extract the basis spectrum of T_1 we require a sample that undergoes rapid SF. The TA of the 1:0 sample shows rapid triplet formation, and the fluorescence UC of this sample indicates all singlets have decayed by ∼25 ps. Assuming that no additional components are present, it follows that the TA spectra after this time must represent a pure T_1 spectrum. We therefore used the 1:0 TA spectrum at 3 ns to extract the T_1 basis spectra, which is given in Figure 4.9. As discussed in Chapter 2, the GSB was incorporated in the S_1 and T_1 basis spectra for simplicity, resulting in the negative values in the 600–700 nm region.

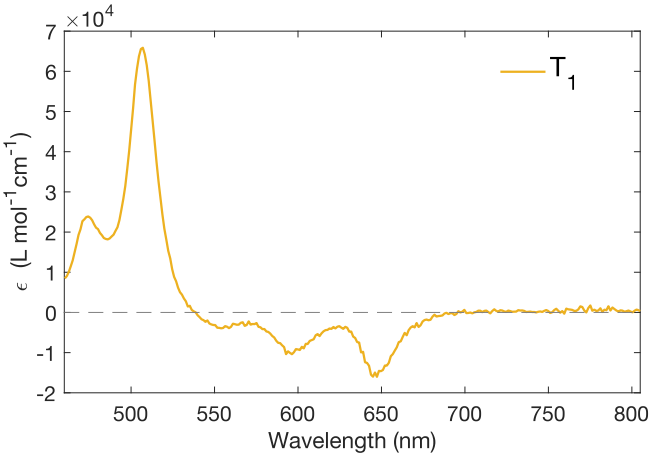

Figure 4.9: T_1 basis spectrum taken from the 1:0 sample at 3 ns.

To extract the S_1 spectra, a sample that does not undergo SF is needed. All of the originally prepared TIPS-Pn:PMMA ratios exhibit instant triplet formation, evident from the short time component in the fluorescence upconversion decay (τ_1), and the sharp rise of the triplet features around 500 nm (Figure 4.8). This result indicates there are no times in any of these TA spectra where only singlets are present. The 10^{-4} M solution of TIPS-Pn in toluene has been previously shown to not undergo SF and as such its TA can be considered a pure singlet spectrum, but the singlets in this sample are in a toluene environment, rather than being surrounded by other TIPS-Pn or PMMA.[47] To minimise the amount of SF in a NP solution the 1:100 TIPS-Pn:PMMA NP suspension was used (Figure 4.5). As discussed previously, the TA of this sample is consistent with that of the dilute TIPS-Pn solution, neither exhibit triplet features or are observed to evolve significantly over time and, additionally, no non-radiative decay pathways are observed in the time-resolved fluorescence (Figure 4.4). This confirms that no intermolecular interactions, and in particular no SF, occur in either sample and therefore the amount of triplets are negligible. The 1:100 sample therefore only contains singlets, so its TA spectrum can be used as a pure singlet basis spectrum, as shown in Figure 4.10. Note that in fitting the data the basis spectra were shifted appropriately for each ratio to match the red shift observed in the steady-state absorption.

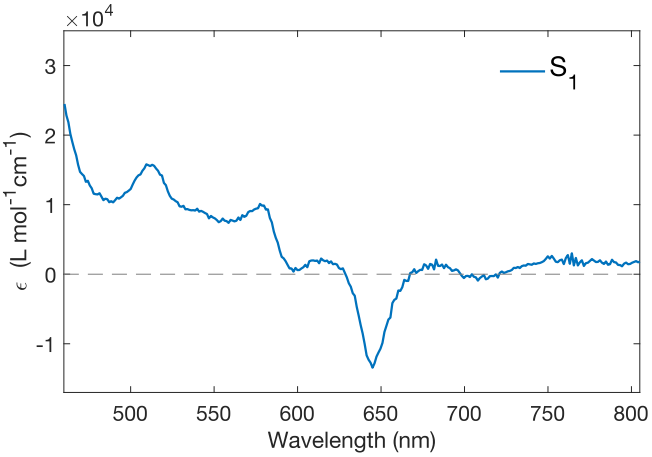

Figure 4.10: S_1 basis spectrum taken from the 1:100 sample at 10 ps.

4.3.1 Two-Component Fits

Initially we attempted to fit the TA using only 2 components, S_1 and T_1. The resultant S_1 and T_1 concentrations as a function of time are given in Figure 4.11 and the fitted TA is shown with the experimental data at selected times in Figures 4.12 and 4.13. Given that the fluorescence decay is a reflection of the S_1 lifetime, the shape of the S_1 curves were constrained to match the fluorescence UC data, and only the magnitude of the concentration, $C_{S_{1max}}$, was fit. The maximum S_1 concentrations are consistent with the expected initial exciton concentration of $\sim 10^{-6}$ M for a 0.1 g L^{-1} TIPS-Pn sample excited at 1.5 mW (see Appendix 4.5.4). Because S_1 decay is so rapid in many of these samples, the observed $C_{S_{1max}}$ are not expected to exactly match those determined from the laser power, so a detailed comparison has not been made. The T_1 population has a much longer lifetime than S_1 as expected, and its decay does not appear to vary significantly between the different samples. The magnitude of the

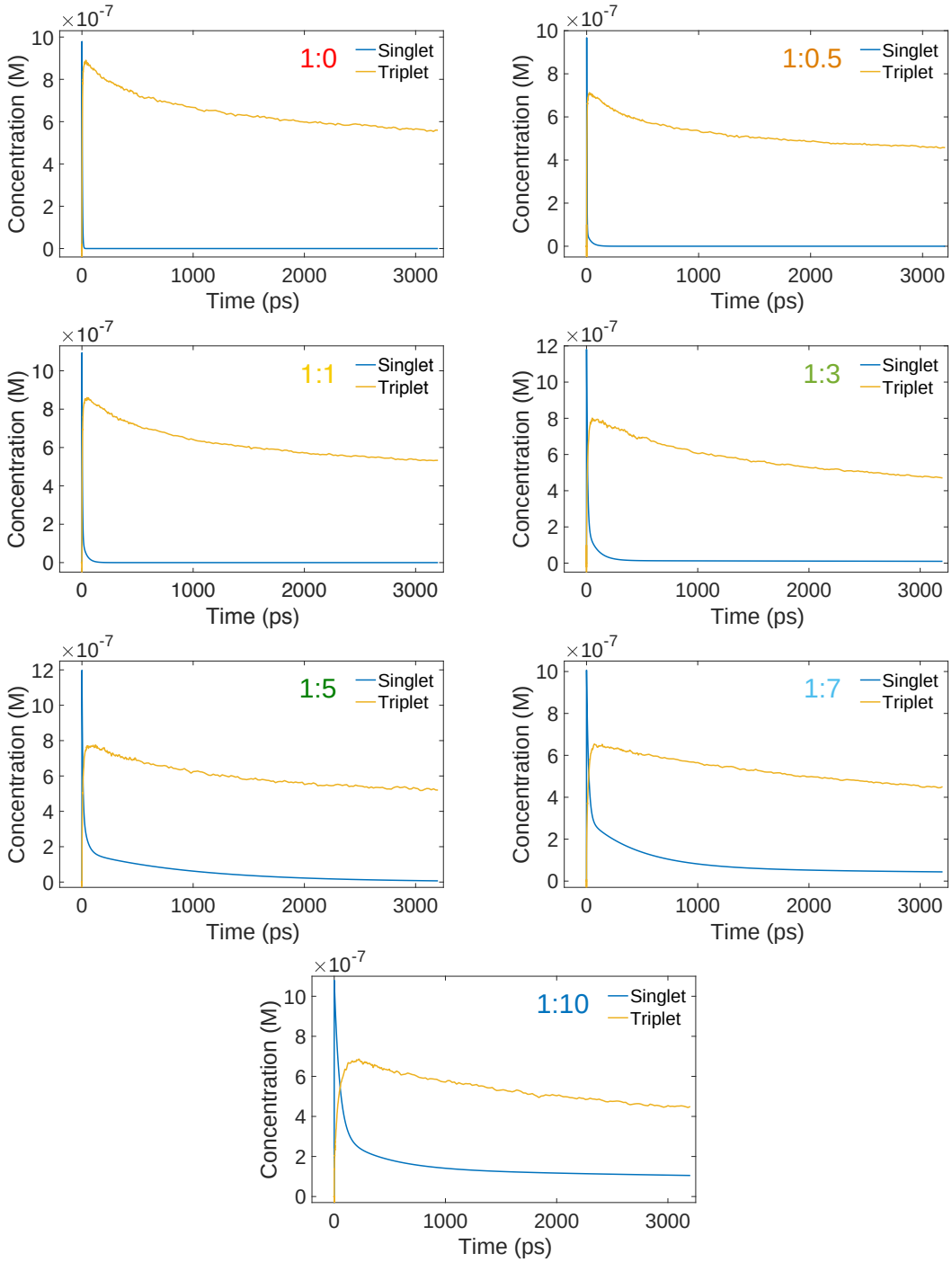

Figure 4.11: Singlet and triplet exciton concentrations over time ($C_{T_1}(t)$ and $C_{S_1}(t)$) fit to the TA data using a 2-component model, with $C_{S_1}(t)$ constrained to fit the fluorescence UC. The basis spectra were shifted appropriately for each ratio to match the red shift observed in the steady-state absorption.

T_1 population, however, does decrease with increasing intermolecular separation. The T_1 and S_1 concentrations can be used to define a SF quantum yield to quantify the efficiency of SF:

$$\phi_{SF} = \frac{\max(C_{T_1})}{\max(C_{S_1})}$$

The theoretical maximum of this yield is 2, which is for the case that every S_1 exciton produces two T_1 excitons, without any recombination or annihilation of triplets. The ϕ_{SF} calculated for each sample are given in Table 4.3, alongside the sum of squares of residuals of the fit.

Table 4.3: Results from 2-component spectral fit to TA data

Sample	Residual Sum of Squares ($\times 10^{-3}$)	Singlet Fission Yield
1:0	10.2	0.91
1:0.5	10.2	0.74
1:1	10.6	0.79
1:3	8.5	0.68
1:5	8.0	0.65
1:7	5.1	0.65
1:10	6.0	0.64

The calculated values of ϕ_{SF} show a decrease as intermolecular separation increases, suggesting closer intermolecular separations are more efficient. However, ϕ_{SF} for the neat (1:0) TIPS-Pn NPs is still considerably lower than what has previously been reported for TIPS-Pn.[39,47,56,74,84] The quality of the fits can be seen in Figures 4.12 and 4.13. At late times (3 ns) the fitted and experimental TA spectra are practically coincident, but deviations are observed at earlier times. Even though the fits are not constrained to a kinetic model, some variation from the experimental data is to be expected, particularly at times when the S_1 population is still present. Although the 1:100 NPs were in the same solvent as the other samples (water), the TIPS-Pn molecules in these NPs are in an almost entirely PMMA environment, which could result in different ESAs to samples surrounded by a large number of TIPS-Pn molecules (this effect of this is directly observed in the red-shift of the steady-state absorption spectra in Section 3.3, Figure 3.4). However, even at 100 ps, by which the singlets have completely decayed for 1:0, 1:0.5 and 1:1 samples, there are still some regions of the spectra the T_1 basis spectrum is unable to fit. For example, the broad band at 750 nm persists after the singlet has decayed, and cannot be accounted for by the triplet. It was mentioned previously that the lifetimes of some of the features in the TA spectra suggest the presence of an additional species. The inability of the T_1 spectra to fit the shape of the TA at intermediate times is further indication of this. Hence to completely fit the TA data an additional component is necessary.

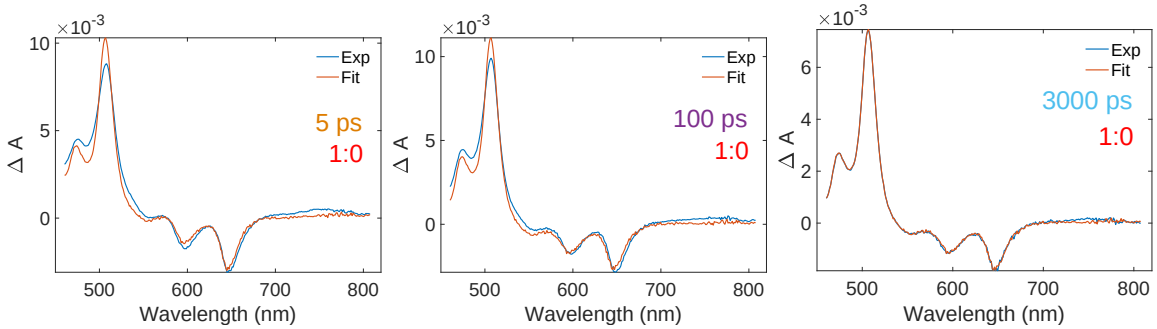

(a) 1:0

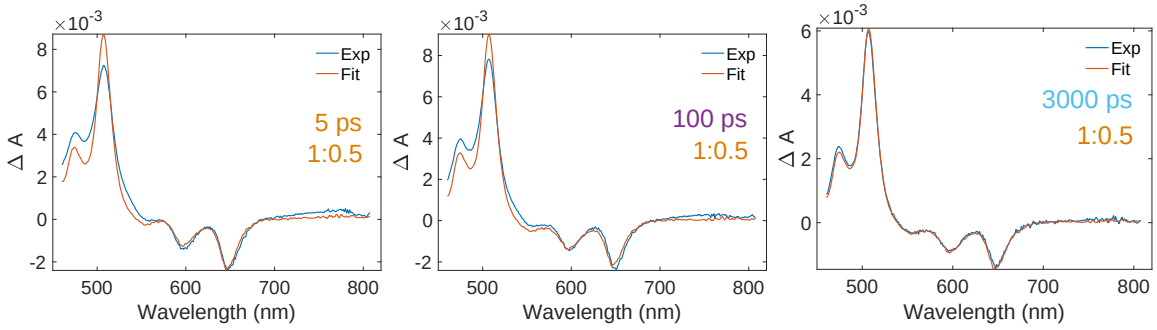

(b) 1:0.5

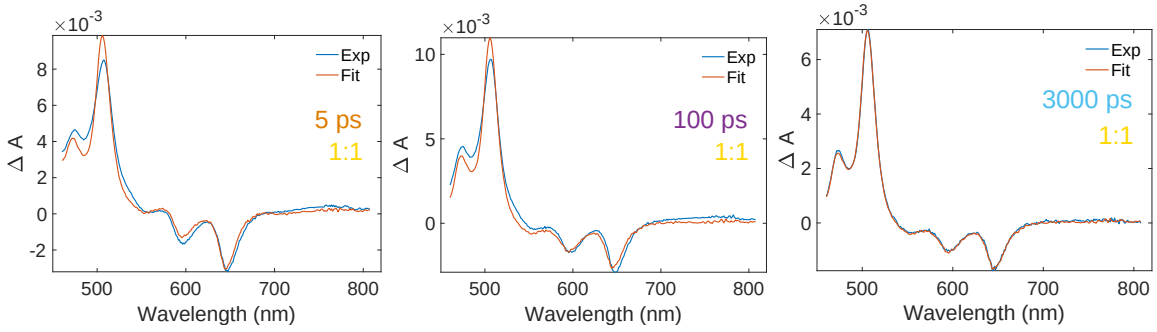

(c) 1:1

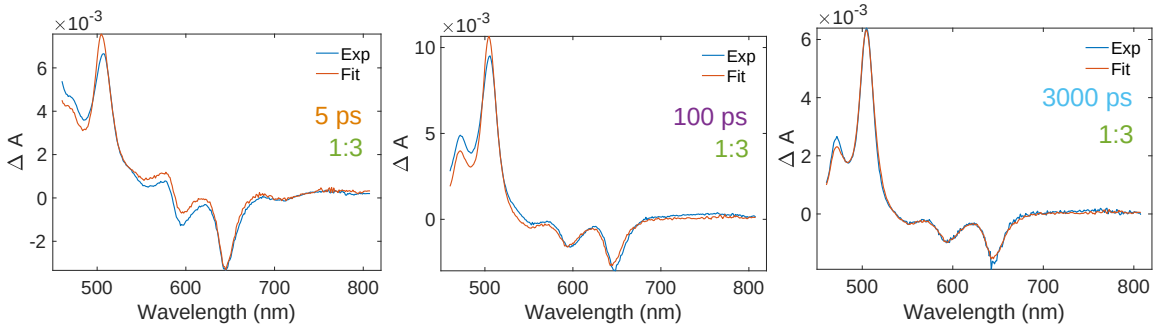

(d) 1:3

Figure 4.12: Two-component least squares fits of extracted basis spectra to the TA data at 5, 100 and 3000 ps for TIPS-Pn:PMMA ratios 1:0 to 1:3.

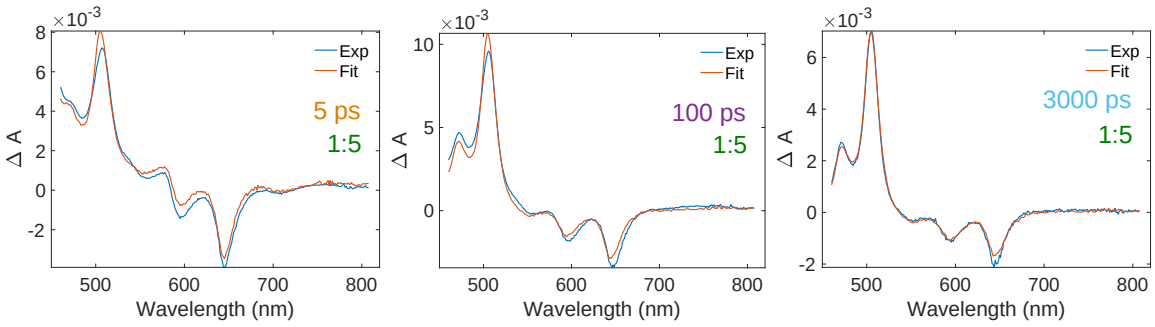

(a) 1:5

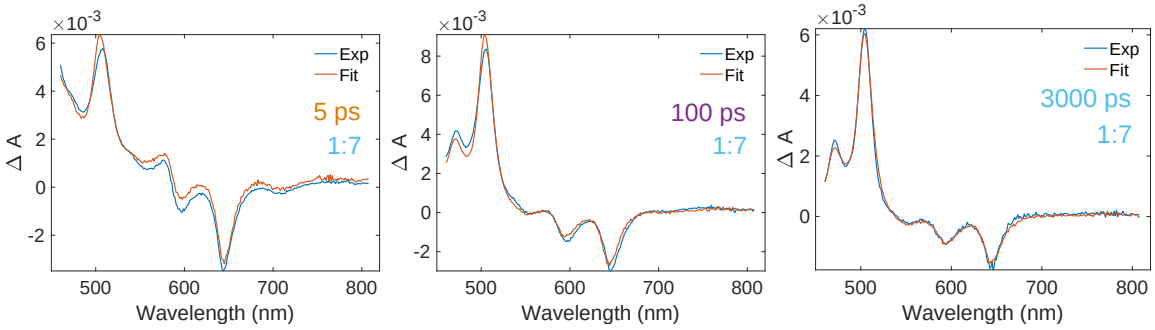

(b) 1:7

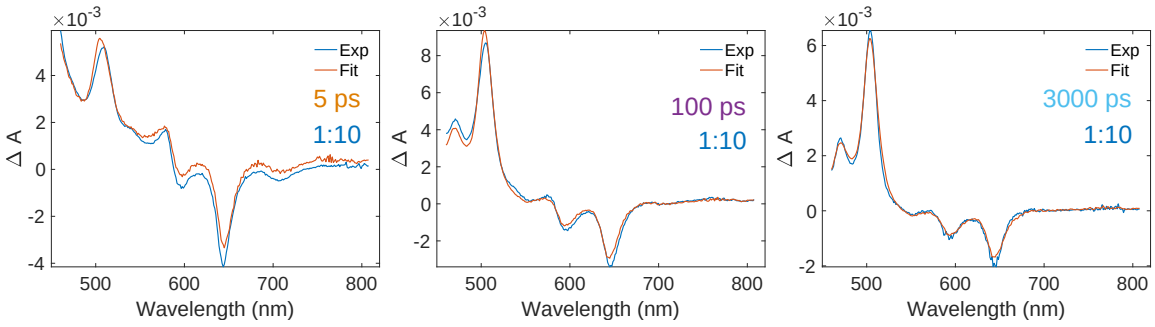

(c) 1:10

Figure 4.13: Two-component least squares fits of extracted basis spectra to the TA data at 5, 100 and 3000 ps for TIPS-Pn:PMMA ratios 1:5 to 1:10.

4.3.2 Three-Component Fits

To improve the spectral fits to the TA spectra an additional species was considered. Recent studies have reported the identification of the triplet pair intermediate in various kinds of systems.[57,59–61,67,103] Whilst the exact the nature and formation of ^{1}(TT) is still unclear, the suggestion that ^{1}(TT) is actually observable in some systems, and the fact our identified third component appears to exist at intermediate times between the S_1 and T_1 states leads to the conclusion that this component is the ^{1}(TT) intermediate. Again, the method for the 3-component fits is described in detail in Section 2.7, but for the clarity of the following discussion we reiterate the method of extracting the basis spectra here. The S_1 and T_1 basis spectra are the same as for the 2-component fits. While the 1:100 TA spectrum can still be considered as pure singlet, an intermediate component means we cannot say with certainty that only triplets are present at 3 ns in the 1:0 sample. However, given the broad band at 750 nm has disappeared by 3 ns, using the TA at this time for a pure T_1 spectrum is still a reasonable approximation. The intermediate species basis spectrum was also obtained using the 1:0 sample, this time at 40 ps, where singlets are absent but the intermediate component is likely to be present. Briefly, the basis spectrum was determined by estimating the amount the T_1 population decays between 40 ps and 3 ns, or in other words, what proportion of the spectra at 40 ps is due to T_1. For example, if T_1 decays by 15% between 40 ps and 3 ns, the contribution due to T_1 at 40 ps is the absorption at 3 ns (pure T_1) plus the 15% that decayed:

$$A_{T_1}(40\text{ ps}) = A(3\text{ ns}) + 0.15 \times A_{T_1}(40\text{ ps})$$

This is indicated by the green curve in Figure 4.14a. The triplet pair contribution is then the difference between the total absorption and the triplet contribution,

$$A_{^1(TT)}(40\text{ ps}) = A(40\text{ ps}) - (A(3\text{ ns}) + 0.15 \times A_{T_1}(40\text{ ps}))$$

as indicated by the green curve in Figure 4.14b. Given the 505 nm peak for this sample decays by 27% in this time, the maximum T_1 can decay is 27%, which is equivalent to saying the composition of the 505 nm peak is 100% T_1. A range of possible triplet and intermediate absorptions at 40 ps are shown in Figure 4.14.

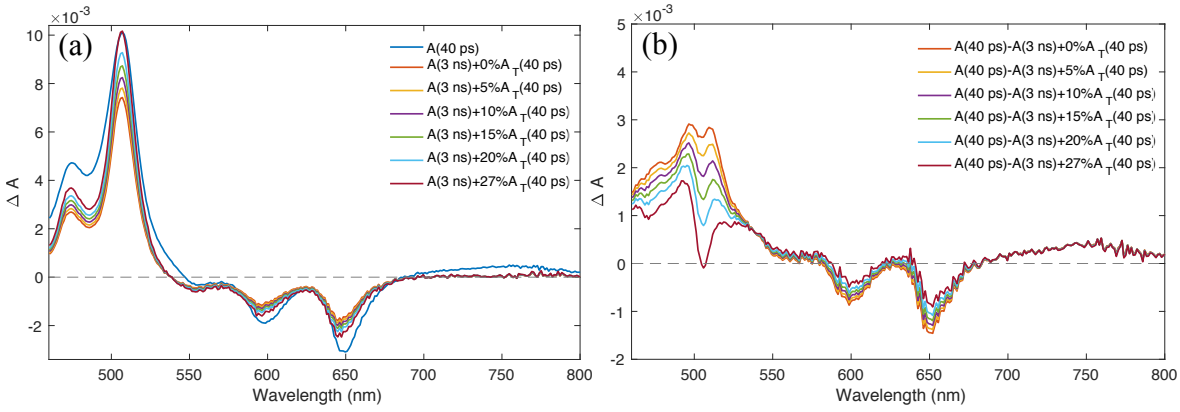

Figure 4.14: Fitting the intermediate component basis spectra. (a) Different proportions of the 1:0 TA spectra at 40 ps that can be attributed to the triplet, where the triplet spectra is taken at 3 ns. (b) Possible intermediate species contributions at 40 ps.

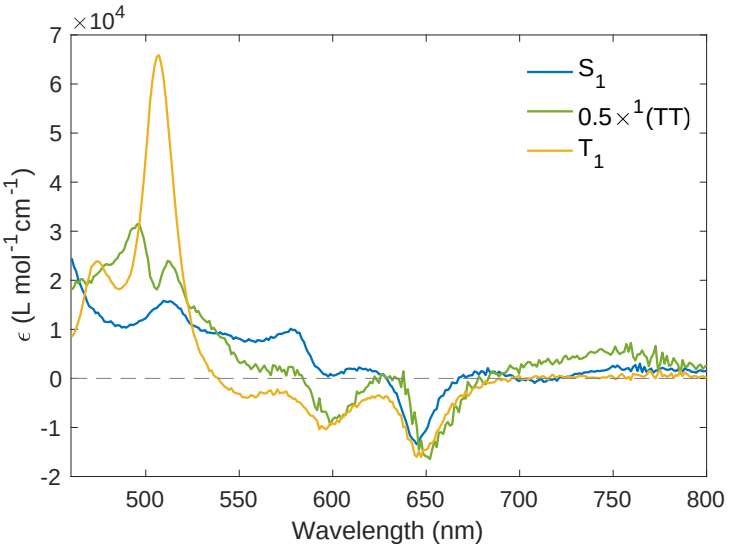

Figure 4.15: Basis spectra for the S_1, T_1 and intermediate species in TIPS-Pn/PMMA NPs, which we attribute to ^{1}(TT).

For the purposes of the following analysis, we used the intermediate basis spectra derived from 15% triplet decay as an example. Given 27% decay corresponds to a decay time of around 10000 ps, 15% 18000 ps, and 0% an infinite lifetime and our experimental window is only 3000 ps, this choice does not significantly affect the results of the fits, but does change the relative magnitudes of C_{T_1} and $C_{^1(TT)}$. The 27% decay implies all the absorption at 507 nm is due to T_1, and 0% means there is a significant ^{1}(TT) component, so these two extremes give the upper and lower bounds of the amount of T_1 produced. As such the singlet fission yields for the 3-component fits are reported as the ranges given by these extremes, and the fits using 0% and 27% triplet decay are given in Appendix 4.5.5.

The S_1, T_1 and 15% triplet decay ^{1}(TT) basis spectra are plotted together in Figure 4.15. The slight dip in the intermediate spectra at 500 nm is a result of the method used to extract the basis spectra from the experimental spectra. It is likely there was some broadening of the 500 nm T_1 feature between 40 ps and 3 ns, so the difference due to this is absorbed into the basis spectra of the intermediate. Apart from this artefact, it appears that ^{1}(TT) also exhibits ESA features around 450–550 nm, as well as the small broad 750 nm band.

The time-dependent concentrations determined by fitting the basis spectra to each TA spectrum are given in Figure 4.16, and the fitted and experimental TA are plotted together in Figures 4.17 and 4.18. For all samples, the fits are significantly improved by including the third component. In Figure 4.17 the fit is practically coincident with the experimental TA at all times for samples 1:0 to 1:1, and only slight deviations are observed for the 1:3 to 1:10 samples at early times. Small discrepancies of the fits at short times are to be expected, as there is some approximation in extracting the S_1 basis spectra, and S_1 is most prevalent at early times. For this same reason the 1:10 data has the worse fit, as this has the most long lived S_1 component. Even so, the 1:10 3-component fit still shows significantly better agreement with experiment than the 2-component. The sum of squares of residuals of these fits are given in Table 4.4. These are smaller than the 2-component fits for all the ratios, and nearly an order of magnitude better for the 1:0 to 1:5 ones.

It should be noted that adding additional components will always increase the goodness of fit, but as the number of components added exceeds the number of species actually present, this improvement becomes trivial. We propose that the improvement in the fit from two to three components is significant, and that the third species is necessary. To confirm this was not a result of the fit method, the TA spectra of the samples were also de-convoluted using global analysis methods, which is reported elsewhere.[104] The spectra used in global analysis are the best fits to the TA data, rather than being manually extracted and assigned as is the case here. Even with this additional freedom, the TA data cannot be fit using only singlets and triplets, and requires three components.

As with the 2-component fits, the initial concentration of S_1 is consistent with that determined using the power of the pump excitation (Appendix 4.5.4), and the time dependence is made to reflect the fluorescence UC. The T_1 time-dependent concentrations in Figure 4.16 show the amount of triplet produced increases with decreasing TIPS-Pn separation. Again a singlet fission quantum yield can be calculated as

$$\phi_{\mathrm{SF}} = \frac{\max(C_{\mathrm{T_1}})}{\max(C_{\mathrm{S_1}})}$$

giving the results in Table 4.4.

Table 4.4: Results from 3-component fit to TA data. The residuals reported are for the ^{1}(TT) basis spectra assuming 15% triplet decay between 40 ps and 3 ns for 1:0 sample. The ϕ_{SF} are ranges given using the two extreme cases for the ^{1}(TT) basis spectra, assuming 0% and 27% T_1 decay.

TIPS-Pn:PMMA Ratio	Residual sum of squares ($\times 10^{-3}$)	ϕ_{SF}	$\phi_{\mathrm{SF'}}$
1:0	2.0	1.10 ± 0.14	1.65 ± 0.04
1:0.5	2.0	0.98 ± 0.16	1.59 ± 0.05
1:1	2.6	1.04 ± 0.15	1.58 ± 0.04
1:3	3.3	0.75 ± 0.09	1.11 ± 0.02
1:5	4.2	0.77 ± 0.08	1.08 ± 0.02
1:7	3.5	0.73 ± 0.05	0.97 ± 0.01
1:10	5.0	0.64 ± 0.04	0.79 ± 0.01

As with the 2-component fits, the triplet yields are much lower than what is expected for TIPS-Pn. To explain this, we examined the concentrations of ^{1}(TT) in Figure 4.16. For all of the samples, the T_1 population can be seen to reach a maximum at relatively early times, from approximately 20 ps for 1:0 to 200 ps for 1:10. The ^{1}(TT) component, however, continues to decay past this time, i.e. the decay of ^{1}(TT) is not correlated with the rise of T_1. This implies that there is an alternate decay pathway for the ^{1}(TT), and that they do not all separate into T_1. This observation is consistent for all variations of ^{1}(TT) spectra, even when 0% triplet decay is assumed (Appendix 4.5.5). To quantify the effect of this behaviour we define a second quantum yield, $\phi_{\mathrm{SF'}}$ which takes into account the ^{1}(TT) intermediate:

$$\phi_{\mathrm{SF'}} = \frac{\max(C_{\mathrm{T_1}} + 2 \times C_{^1(\mathrm{TT})})}{\max(C_{\mathrm{S_1}})}$$

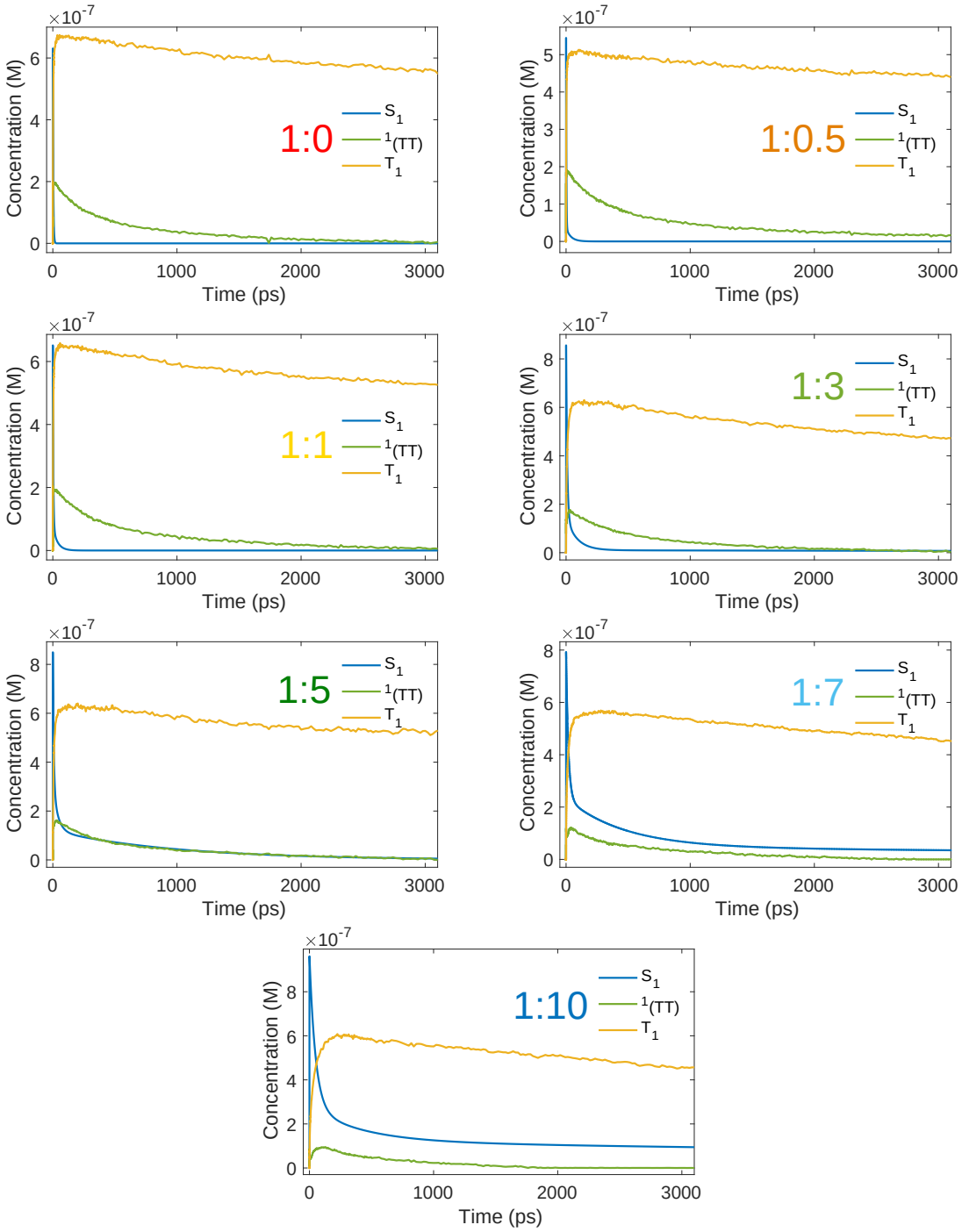

Figure 4.16: Singlet, triplet and triplet pair intermediate concentrations over time ($C_{\mathrm{T_1}}(t)$, $C_{\mathrm{S_1}}(t)$ and $C_{^1(\mathrm{TT})}$) fit to the TA data using a 3 component separation. $C_{\mathrm{S_1}}(t)$ was constrained to fit the fluorescence UC, and the ^{1}(TT) basis spectrum corresponding to 15% $\mathrm{T_1}$ decay between 40 ps and 3 ns for the 1:0 sample was used.

Several reviews on SF by Michl, Smith, Monahan and others have emphasised that SF should not be considered to be complete unless individual separated triplets are produced.[21,29,66] We therefore do not call $\phi_{SF'}$ a singlet fission quantum yield. Instead, this quantity represents the amount of singlets that begin to undergo SF to form ^{1}(TT), i.e. the efficiency of the first step(s) of SF. The values of $\phi_{SF'}$ for low proportions of PMMA are much closer to 2 than ϕ_{SF}, as is expected for TIPS-Pn SF quantum yields. This suggests the low values of ϕ_{SF} are due to the failure of the ^{1}(TT) state separation, rather than processes such as (non-geminate) triplet-triplet annihilation. That is, for the samples with $\phi_{SF'}$ close to 2, most singlets begin to undergo SF as expected from past studies, but they do not all separate into T_1. No additional S_1 population is observed to form, so the decay of ^{1}(TT) is unlikely to be the reverse reaction of SF. Instead we suggest that ^{1}(TT) decays non-radiatively to the ground state.

As the proportion of PMMA and hence intermolecular TIPS-Pn separation increases, both quantum yields decrease. This indicates that there are losses other than the ^{1}(TT) state not separating for these samples. Additionally, the long lifetime of the S_1 and ^{1}(TT) states, and the slow formation of T_1 suggests the rate of SF is much slower in large TIPS-Pn separation samples. In order to explain these phenomena we fit the TA data to a kinetic model, as described in the next chapter.

4.4 Conclusions

Both the TA spectra and time-resolved fluorescence show evidence that the rate of SF decreases with increasing intermolecular separation. The fluorescence lifetime is much longer for large intermolecular separations, implying a slower depletion of the S_1 population, and the T_1 ESA in the TA has a slower formation time (though this is still fast enough to rule out triplet formation due to intersystem crossing). Because there is so much overlap and complexity in the TA data, it was necessary to deconvolute it using a linear combination of the basis spectra of the constituent species. It is evident that the TA spectra cannot be explained with a 2-component model. The ^{1}(TT) intermediate clearly shows some spectral contribution, and therefore must be accounted for. Fitting 3-components, S_1, ^{1}(TT) and T_1, shows that the decay of ^{1}(TT) is not correlated with the rise of T_1, and the yields are much lower than what has previously been reported in the literature. To explain the trend in SF rates and the significant losses of efficiency observed, we fit the TA data to a kinetic model, as described in Chapter 5.

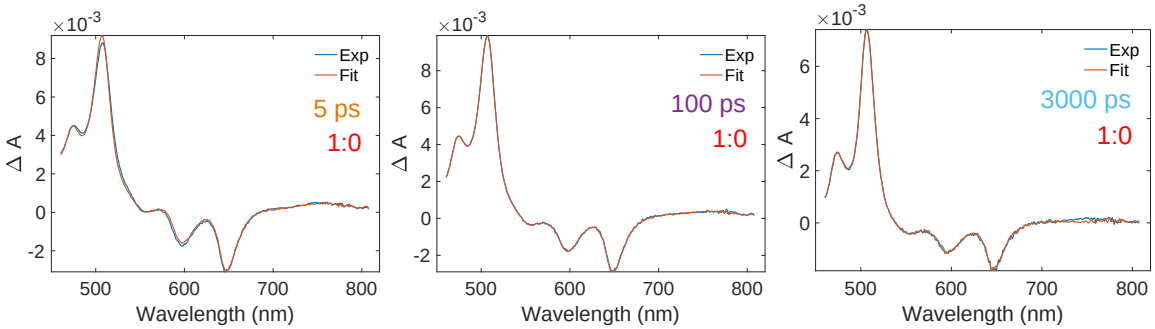

(a) 1:0

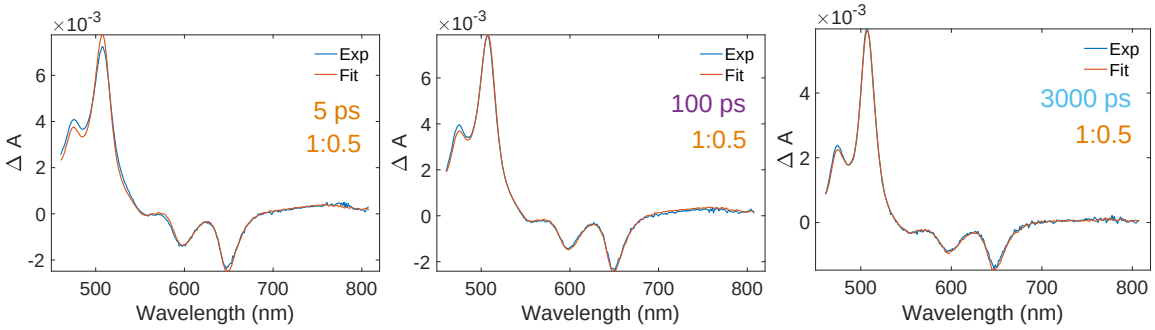

(b) 1:0.5

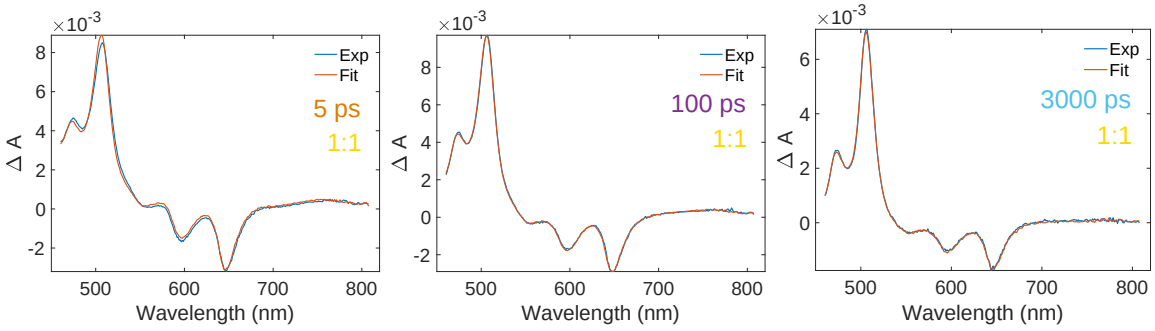

(c) 1:1

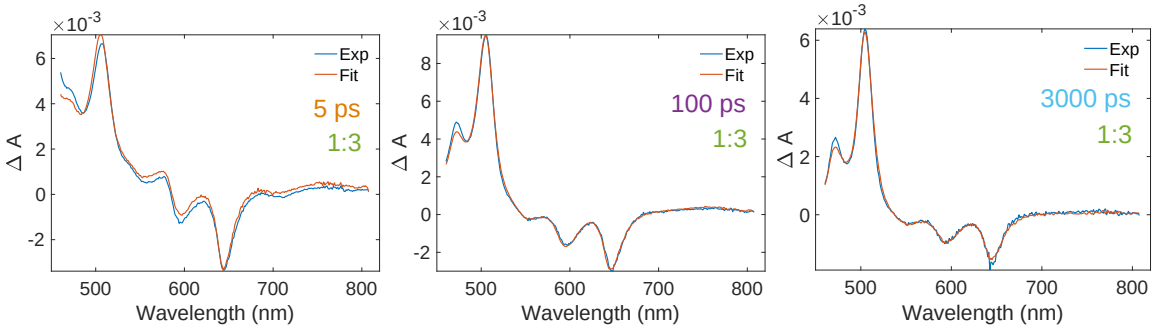

(d) 1:3

Figure 4.17: Three-component least squares fits of extracted basis spectra to the TA data at 5, 100 and 3000 ps for TIPS-Pn:PMMA ratios 1:0 to 1:3. The fits used ^{1}(TT) basis spectrum corresponding to 15% T_1 decay between 40 ps and 3 ns for the 1:0 sample.

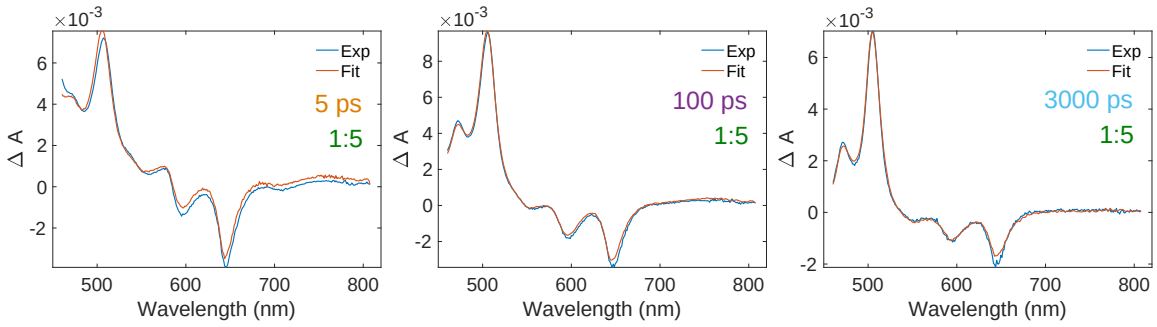

(a) 1:5

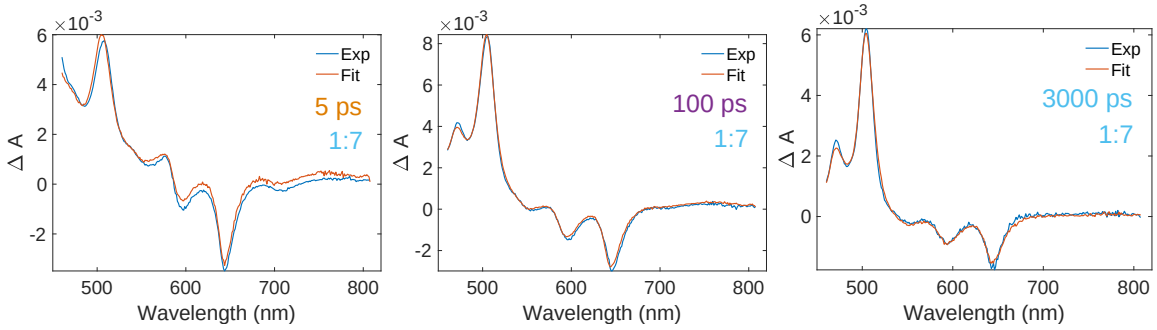

(b) 1:7

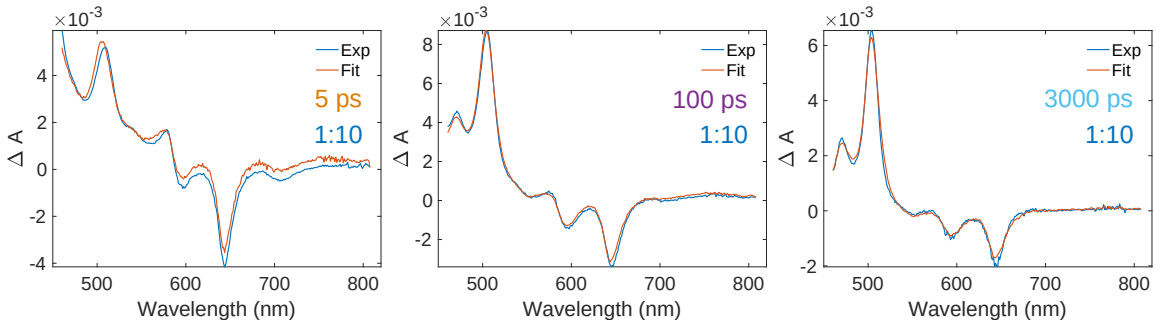

(c) 1:10

Figure 4.18: Three-component least squares fits of extracted basis spectra to the TA data at 5, 100 and 3000 ps for TIPS-Pn:PMMA ratios 1:5 to 1:10.

4.5 Appendix

4.5.1 Steady-state Absorption of 1:100 TIPS-Pn:PMMA

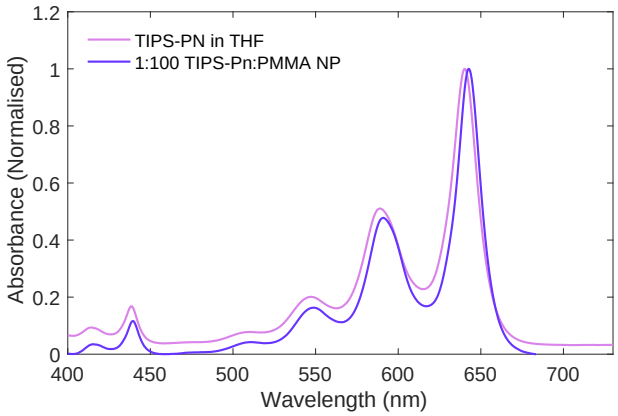

Figure 4.19: Steady-state absorption of 1:100 TIPS-Pn:PMMA NP sample. The 1:100 sample was measured in a 1 cm path length cuvette and corrected for scattering.

4.5.2 Transient Absorption Wavelength Dependence

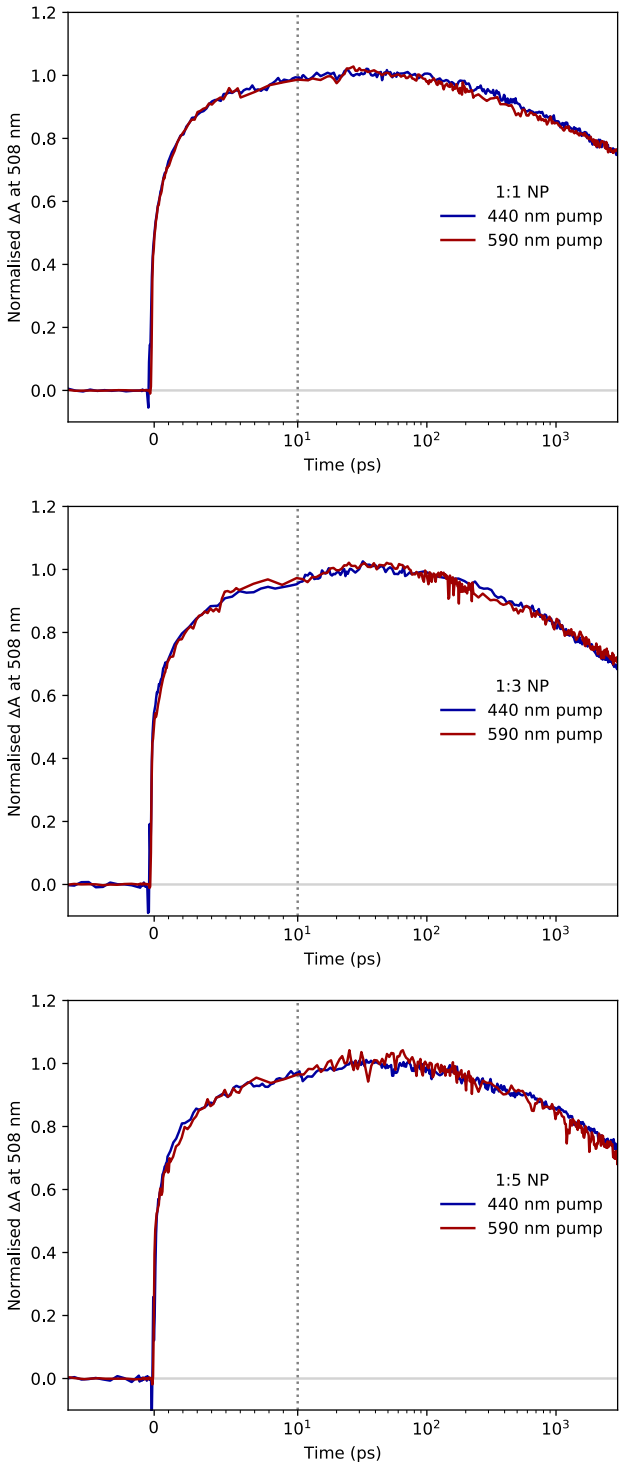

Figure 4.20: Pump wavelength dependence of the ESA feature at 508 nm for 1:1, 1:3 and 1:5 ratio TIPS-Pn:PMMA NPs. In all cases exciting the sample at 590 nm ($S_0 \rightarrow S_1$) had the same effect as exciting at 440 nm ($S_0 \rightarrow S_2$).

4.5.3 Transient Absorption Power Dependence

For pump powers of 0.1-2 mW, exciton dynamics showed no dependence on pump power, confirming no exciton-exciton annihilation in this regime. If singlet-singlet annihilation were present for example, the rate of singlet decay would increase with increasing exciton concentration, and therefore with increasing laser power.

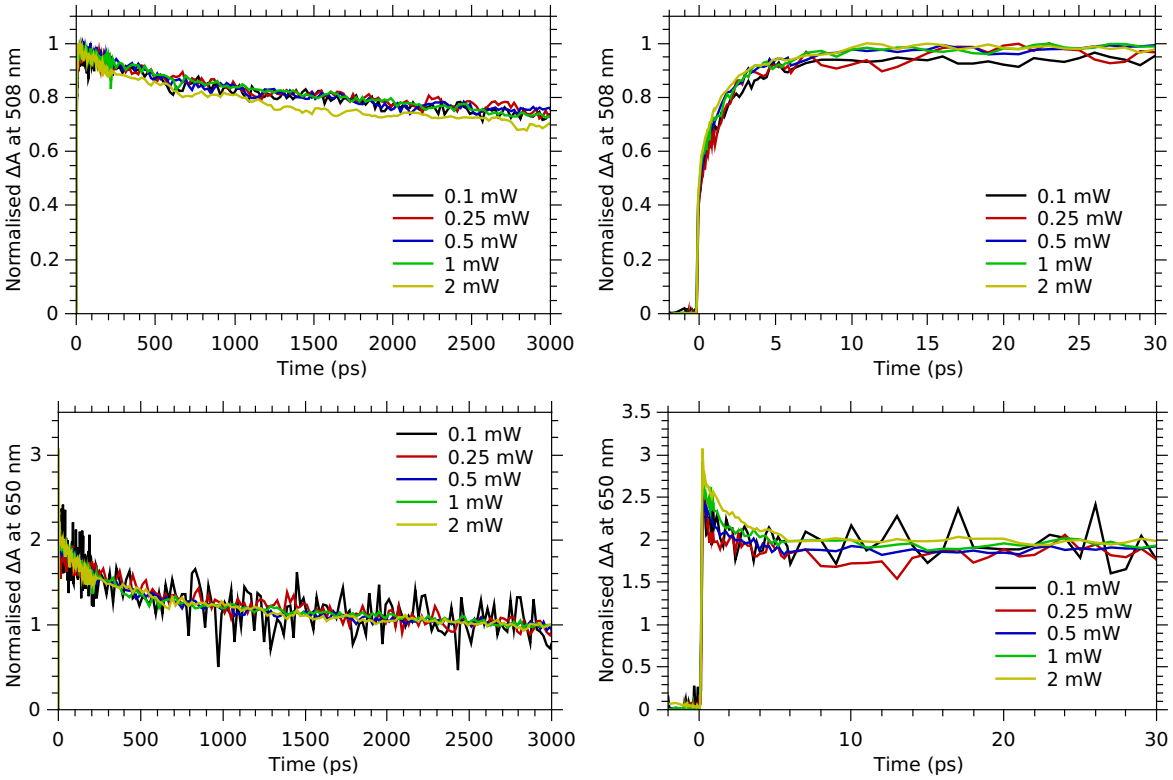

Figure 4.21: Pump power dependence of ESA and GSB features at 508 nm and 650 nm, respectively, for a 1:1 ratio TIPS-Pn:PMMA NPs.

4.5.4 Exciton Concentrations from Laser Power

The absorbance of the $0.1\,\mathrm{g\,L^{-1}}$ ($1.58 \times 10^{-4}\,\mathrm{M}$)1:0 TIPS-Pn:PMMA sample at 440 nm was A_{440}=0.098. Therefore, for pump pulse of 440 nm, with a 737 nm spot width ($4.26 \times 10^{-7}\,\mathrm{m^2}$ spot area) and 1.5 µJ energy, the initial concentration of excitons generated by the pump can be calculated as follows:

$$
\begin{aligned}
\text{photons absorbed per pulse} &= (1 - \text{transmission of pump}) \times \text{photons per pump pulse} \\
&= (1 - 10^{-\mathrm{A}_{440}}) \times \frac{\text{pulse energy}}{\text{photon energy}} \\
&= (1 - 10^{-0.098}) \times \frac{1.5 \times 10^{-6}\mathrm{J}}{4.51 \times 10^{-19}\mathrm{J}} \\
&= 6.72807 \times 10^{11} \\
&= \text{number of excitons per pulse} \\
\therefore \text{exciton concentration} &= \frac{6.72807 \times 10^{11}}{N_A \times \text{excitation volume}} \\
&= \frac{6.72807 \times 10^{11}}{N_A \times (0.002\mathrm{m} \times 4.26 \times 10^{-7}\mathrm{m^2})} \\
&= 1.30947 \times 10^{-6}\mathrm{molL^{-1}} \\
&\approx 1 \times 10^{-6}\mathrm{molL^{-1}}
\end{aligned}
$$

4.5.5 Three-component fits assuming 0% and 27% triplet decay

Note for the fits assuming 0% T_1 decay between 40 ps and 3 ns the T_1 curve still appears to decay slightly. This is because the T_1 concentration had not actually reached a max by 40 ps.

Table 4.5: Results of 3-component fits using ^{1}(TT) basis spectrum derived from assuming 0%, 15% and 27% T_1 between 40 ps and 3 ns for the 1:0 sample.

Sample	Residual sum of squares $\times 10^{-3}$			ϕ_{SF}			$\phi_{SF'}$		
	0%	15%	27%	0%	15%	27%	0%	15%	27%
1:0	1.9	2.0	2.0	0.96	1.07	1.25	1.61	1.66	1.68
1:0.5	2.0	2.0	2.0	0.82	0.94	1.13	1.53	1.60	1.64
1:1	2.6	2.6	2.6	0.90	1.02	1.19	1.54	1.59	1.62
1:3	3.3	3.3	3.3	0.66	0.74	0.84	1.09	1.11	1.13
1:5	4.2	4.2	4.2	0.69	0.75	0.85	1.06	1.09	1.10
1:7	3.4	3.5	3.5	0.67	0.72	0.78	0.96	0.97	0.98
1:10	5.0	5.0	5.0	0.60	0.63	0.68	0.79	0.80	0.80

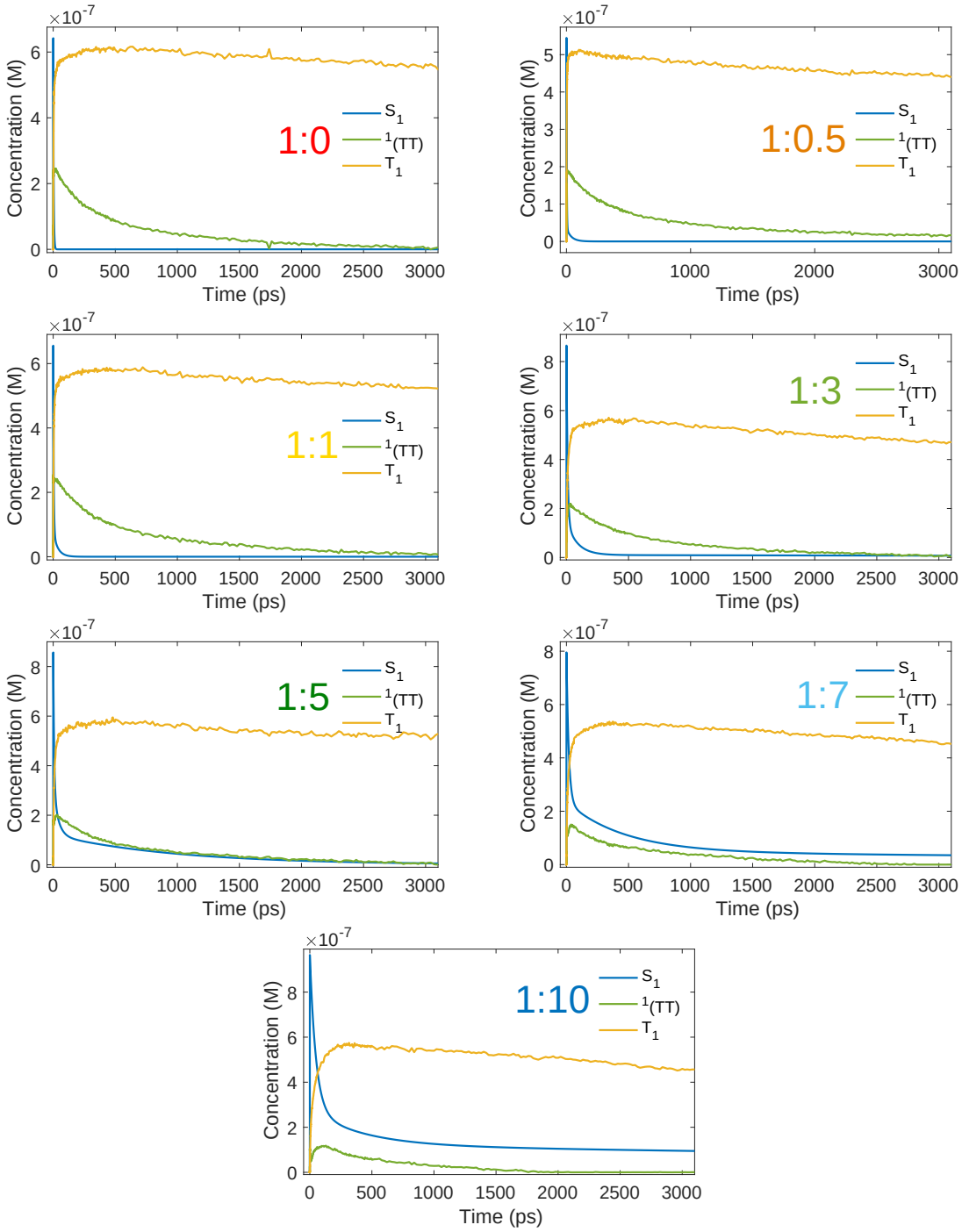

Figure 4.22: S_1, T_1 and ^{1}(TT) concentrations over time ($C_{T_1}(t)$, $C_{S_1}(t)$ and $C_{^1(TT)}$) fit to the TA data using a 3 component separation. $C_{S_1}(t)$ was constrained to fit the fluorescence UC, and the ^{1}(TT) basis spectrum corresponding to 0% T_1 decay between 40 ps and 3 ns was used.

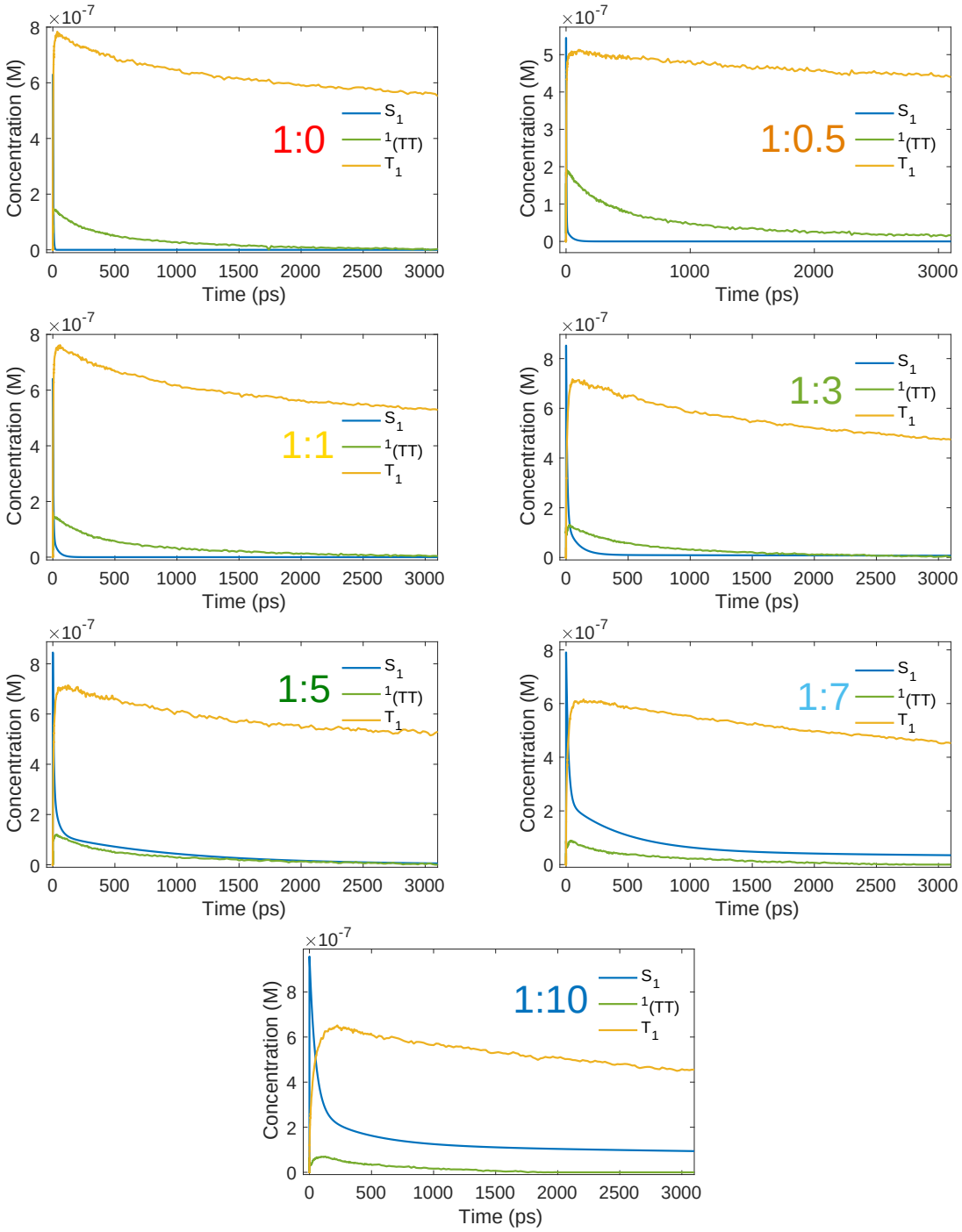

Figure 4.23: S_1, T_1 and ^{1}(TT) concentrations over time ($C_{T_1}(t)$, $C_{S_1}(t)$ and $C_{^1(TT)}$) fit to the TA data using a 3 component separation. $C_{S_1}(t)$ was constrained to fit the fluorescence UC, and the ^{1}(TT) basis spectrum corresponding to 27% T_1 decay between 40 ps and 3 ns was used.

CHAPTER 5
Kinetic Modelling of Singlet Fission in TIPS-Pn/PMMA Nanoparticles

In Chapter 4 it was established that the efficiency of SF in TIPS-Pn/PMMA nanoparticles decreased with increasing proportion of PMMA, or equivalently, increasing intermolecular separation of TIPS-Pn molecules. However, even the highest yields were only slightly over 1, half than what has previously been reported for TIPS-Pn.[47,56] Additionally the trends of the decay of the triplet pair intermediate, ^{1}(TT), and rise of separated triplets, T_1, were not apparently correlated. Potentially this implies a loss of efficiency through the non-radiative decay of the intermediate state, rather than its dissociation into separated triplets. To explain the observed behaviour we fit the time-resolved fluorescence and TA spectra described in Chapter 4 to a series of kinetic models outlined in this chapter. We begin with a simple model of SF, accounting for diffusion and the presence of the triplet pair intermediate, and show this is insufficient to fit the data. Two subsequent models are then proposed, of which only the final provides a reasonable fit of all seven TIPS-Pn:PMMA mass ratios studied. The underlying theory of each model and the methods of fitting are described in detail in Chapter 2. Here we only reiterate the main aspects, describe how the specific schemes are able or unable to explain the data and the implications of the final model.

5.1 Scheme 1

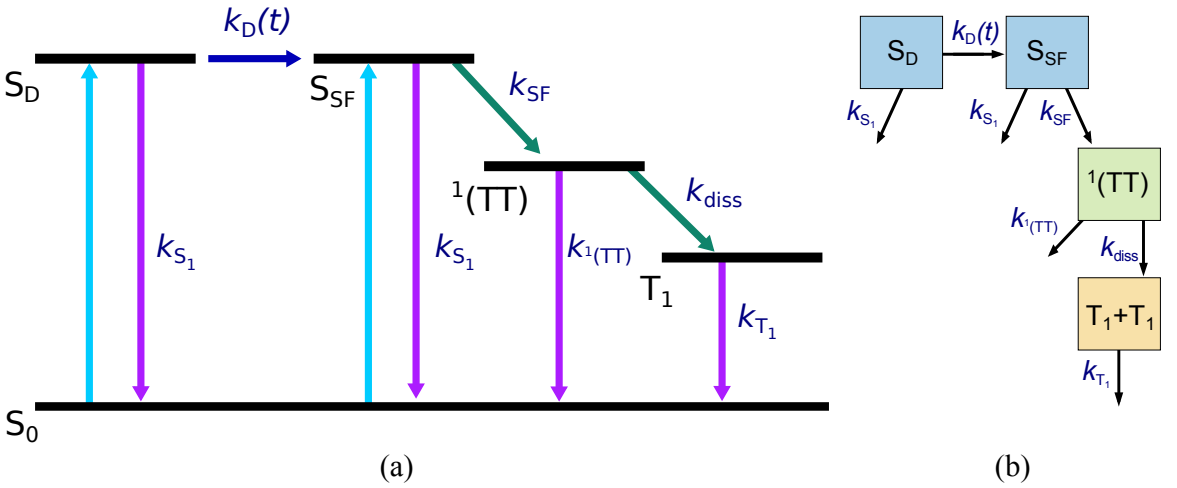

Figure 5.1: Kinetic Scheme 1. (a) Energy-level diagram of Kinetic Scheme 1, in which blue arrow represents the initial excitation of the S_1 state. (b) Flow diagram of Kinetic Scheme 1.

To describe SF in the TIPS-Pn/PMMA NPs, we initially fit the data with the relatively simple model in Figure 5.1. In Chapter 4, we showed that the decay of the time-resolved fluorescence, and hence the decay of the S_1 state of TIPS-Pn, was multi-exponential. We explain this phenomena here by modelling SF as diffusion limited. Because of the amorphous arrangement of TIPS-Pn in the NPs, it is likely that only a portion of neighbouring TIPS-Pn molecules will have a separation and orientation favourable for SF, which we call "SF sites".[50] Singlet excitons generated near SF sites undergo prompt SF, leading to the rapid decay of the fluorescence. Excitons located elsewhere in the NP have to first diffuse to reach SF sites, so SF from these is delayed, leading to the slower fluorescence decay. This behaviour was modelled by splitting the S_1 state into two sub-populations, S_{SF}, representing singlet excitons located on a SF site, and S_D, representing the diffusing population, such that

$$[S_1] = [S_D] + [S_{SF}].$$

S_D diffuses to S_{SF} with the time-dependent rate constant k_D, and S_{SF} undergoes fission with rate constant k_{SF}. Both singlet populations are also able to decay to the ground state with rate constant k_{S_1}. From the spectral fits in Chapter 4, we established the TA data could not be described with just the S_1 and T_1 populations, so the correlated triplet pair intermediate, $^1(TT)$, was also included in the model. This dissociates to give two triplets with the rate constant k_{diss}. To account for the low yields and lack of correlation between the decay of $^1(TT)$ and rise of T_1 seen in Chapter 4, $^1(TT)$ was also allowed to decay non-radiatively to the ground state with rate constant $k_{^1(TT)}$. Finally, given the lack of power dependence of the TA data, the decay of T_1 was modelled as unimolecular with rate constant k_{T_1}, resulting in a model described by the series of coupled differential equations below:

$$\frac{d[S_D]}{dt} = -k_{S_1}[S_D] - k_D(t)[S_D];$$
$$\frac{d[S_{SF}]}{dt} = -k_{S_1}[S_{SF}] + k_D(t)[S_D] - k_{SF}[S_{SF}];$$

$$\begin{aligned}\frac{\mathrm{d}[^1(\mathrm{TT})]}{\mathrm{d}t}&=k_{\mathrm{SF}}[\mathrm{S_{SF}}]-k_{\mathrm{diss}}[^1(\mathrm{TT})]-k_{1(\mathrm{TT})}[^1(\mathrm{TT})];\\ \frac{\mathrm{d}[\mathrm{T}]}{\mathrm{d}t}&=2\times k_{\mathrm{diss}}[^1(\mathrm{TT})]-k_{\mathrm{T}}[\mathrm{T_1}].\end{aligned} \tag{5.1}$$

The time-resolved fluorescence of the two samples that do not undergo SF, the dilute TIPS-Pn solution and the 1:100 TIPS-Pn:PMMA NPs, both fit to a single exponential with a 12 ns time constant. Given no SF occurs in these samples, this was attributed to the intrinsic lifetime of S_1, and so k_{S_1} was constrained to be $8.33\times10^{-5}\,\mathrm{ps}^{-1}$ (1/12 ns). The rate of diffusion of singlet excitons to SF sites was modelled by a Smoluchowski diffusion rate:

$$k_{\mathrm{D}}(t)=4\pi RDc_{\mathrm{SF}}\left(1+\frac{R}{\sqrt{\pi Dt}}\right), \tag{5.2}$$

where c_{SF} is the total number of singlet fission sites in a NP, R is the trapping radius of the SF site and D is the singlet exciton diffusion constant. For simplicity this expression was parametrised to

$$k_{\mathrm{D}}(t)=a+bt^{-0.5}, \tag{5.3}$$

such that $a=4\pi RDc_{\mathrm{SF}}$ and $b=4\pi^{-\frac{1}{2}}R^2D^{-\frac{1}{2}}c_{\mathrm{SF}}$. The time-resolved fluorescence of the 1:0 sample fits to a single exponential decay, with a time constant of 3.9 ps or rate constant of $0.256\,\mathrm{ps}^{-1}$, indicating SF in this sample is not diffusion limited (i.e. all neighbouring pairs of TIPS-Pn molecules act as SF sites). If the S_D population is zero, then all of the S_1 decay can be attributed to SF, so we can constrain k_{SF} to be $0.256\,\mathrm{ps}^{-1}$. We then assumed the difference in rates of formation of ^{1}(TT) and T_1 between the different samples is due to diffusion, and that the rate constant of SF does not change. In other words, the requirements or definition of what constitutes a SF site does not change from sample to sample; only the number of SF sites or the amount of diffusion required to reach them will vary. As such k_{SF} was constrained to be $0.256\,\mathrm{ps}^{-1}$ for every sample. Lastly, we also constrained k_{T_1} to be 6.67×10^{-5} ps^{-1}, as this value was found to fit well to the 1:0 data. It may be more valid to let this parameter vary between the samples to determine if T_1 decays faster for some intermolecular separations than others, but this decay is slow for all samples, at least over 10 ns, whereas the time window of our experiment was only 3 ns. We therefore could not fit this decay reliably enough to establish any trends. So for simplicity k_{T_1} was fixed to be the same as that in the 1:0 sample (note k_{S_1} was able to be determined reliably from TCSPC with a 50 ns time window, but no such equivalent was available for studying the T_1 decay). The parameters that were fit to the data were then a, b, $k_{1(\mathrm{TT})}$, k_{diss}, and the initial concentrations of S_{SF} and S_{D} after excitation, $S_{\mathrm{SF}}(0)$ and $S_{\mathrm{D}}(0)$.

As the spectrally extracted fits in Chapter 4 used the time-resolved fluorescence to constrain the rate of change of the S_1 state, we predominantly fit the kinetic model to the 3-component spectrally extracted concentrations of S_1, ^{1}(TT), and T_1, rather than the TA data itself. In this way both the behaviour from the TA and the time-resolved fluorescence was accounted for. When the models were instead fit directly to the TA spectra, slightly better residuals between the fitted and experimental TA were observed, but the fits were less physically meaningful in the sense that fitted S_1 concentration did not reflect time-resolved fluorescence. Fits directly to TA are only

reported here if the residuals were substantially better than fitting to the spectrally extracted concentrations, and the S_1 concentrations agreed reasonably well.

To test Scheme 1, only the 1:0 and 1:10 samples were fit, as these represent the two opposite extremes of the trends observed. The fit parameters are given in Table 5.1, and the fitted S_1, ^{1}(TT) and T_1 concentrations are shown alongside the spectrally extracted concentrations from Chapter 4 in Figure 5.2.

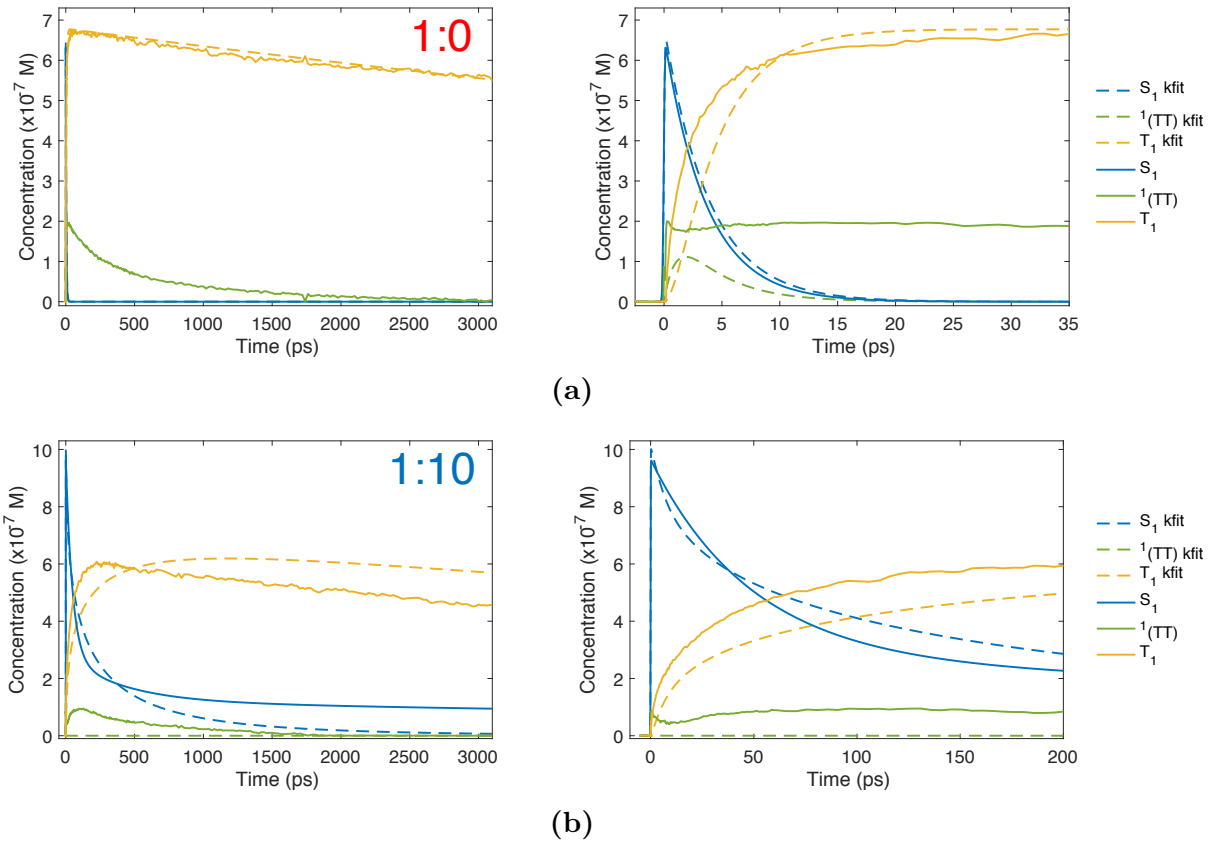

Figure 5.2: Fitted concentrations of Scheme 1 with the spectrally extracted concentrations from Chapter 4. Concentrations are shown for 1:0 TIPS:PMMA sample over 35 ps and 3000 ps in (a) and concentrations of the 1:10 sample are shown over 3000 ps and 200 ps in (b).

Table 5.1: Fit parameters for best fit of Scheme 1 to 1:0 and 1:10 TIPS-Pn:PMMA NPs. The rate of diffusion was given by $k_D = a + bt^{-0.5}$, and $k_{S_1} = 8.33 \times 10^{-5}$ ps^{-1}, $k_{T_1} = 6.67 \times 10^{-5}$ ps^{-1} and $k_{SF} = 0.256$ ps^{-1}. r_C is the residual sum of squares of the fitted concentrations with the spectrally extracted concentrations, and r_A is the residual sum of squares of the fitted TA data with the experimental TA data. Note that no diffusion occurs for the 1:0 sample, so the values of a and b are arbitrary.

TIPS-Pn:PMMA	a (ps^{-1})	b (ps$^{-\frac{1}{2}}$)	k_{diss} (ps^{-1})	$k_{^1(TT)}$ (ps^{-1})	$S_D(0)$ (10^{-7} M)	$S_{SF}(0)$ (10^{-7} M)	r_C (10^{-7} M)	r_A (10^{-3})
1:0	55†	9.05†	0.48	0.49	0.00	6.84	510	29
1:10	1×10^{-13}	0.04	28.17	52.01	9.36	0.72	496	23

† Does not affect the quality of the fit and has no physical significance.

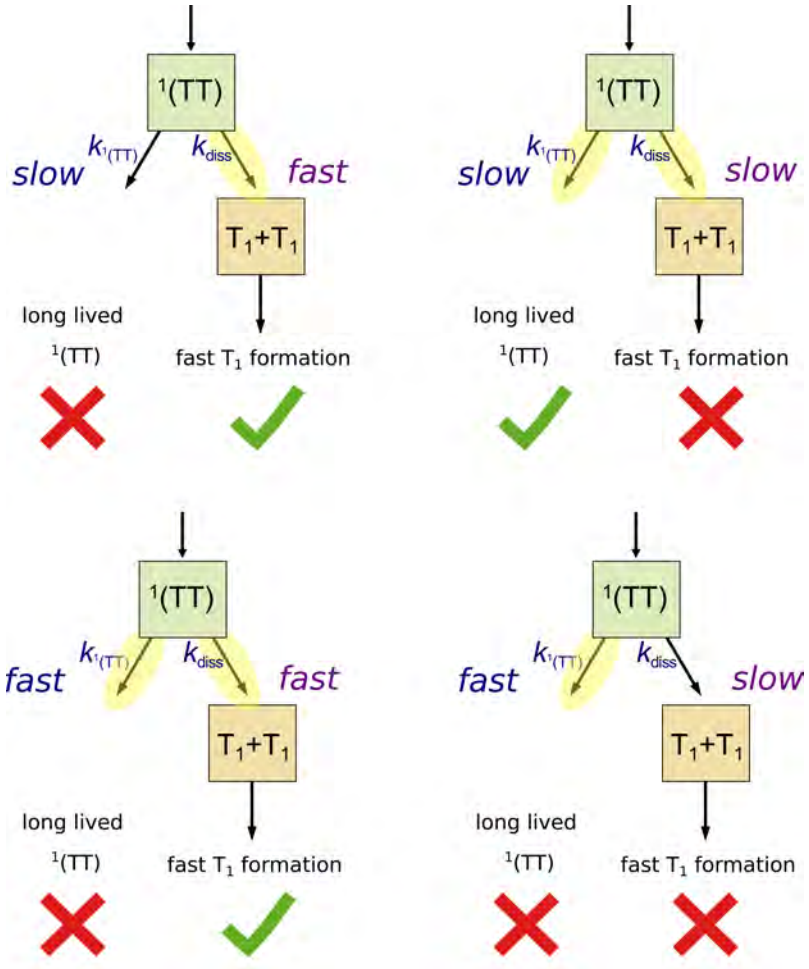

Figure 5.3: Deficiency of Scheme 1 in fitting the data. When dissociation of ^{1}(TT) is fast, no long-lived component is observed, but when dissociation is slow, no rapid triplet formation is observed. Major decay pathways are highlighted in yellow.

It is clear from the fits in Figure 5.2 that this model is unable to describe all the behaviour in the data. The residual sum of squares of the reconstructed TA and experimental TA (r_A) are 2.9×10^{-2} and 2.3×10^{-2} for the 1:0 and 1:10 TIPS-Pn:PMMA samples, respectively. Given the three component spectral fits in Chapter 4 had residuals 2.0×10^{-3} and 5.0×10^{-3} this is relatively high. In Figure 5.2 the fitted concentrations of S_1, ^{1}(TT) and T_1 (labelled "S_1 kfit", "^{1}(TT) kfit", and "T_1 kfit", respectively), can be seen to deviate from the spectral fit concentrations (labelled "S_1", "^{1}(TT)", and "T_1"). Whilst perfectly fitting the spectrally extracted concentrations is not strictly necessary for a good fit to the TA (as there is some error associated with the spectral fits, and a chance they are only local minima of the objective function of the fit, not global), the concentrations are still expected to be reasonably similar. Given the S_1 concentration comes from the time-resolved fluorescence, the kinetic fits should especially be able to reproduce this component. However, the fitted S_1 concentration for the 1:10 sample appears to decay too fast. Additionally, the fitted ^{1}(TT) concentration decays so fast that it appears non-existent, and the triplet population is overestimated at late times. The kinetic fit of the 1:0 sample is better, with good agreement between the S_1 and T_1 populations, but the triplet pair again decays too fast, lasting only 15 ps instead of around 2 ns. It appears that although the fit of the S_1 and T_1 populations for

the 1:0 sample are good, the model is unable to be extended to higher intermolecular separations, and cannot account for the long-lived ^{1}(TT) population observed.

We can rationalise the failure of this model to reproduce the data by looking at the possible pathways of the ^{1}(TT) population, as shown in Figure 5.3. As discussed in Chapter 4, the concentration of T_1 rises very rapidly, but ^{1}(TT) decays slowly. To account for the rapid rise of the triplets, k_{diss} must be fast. But to observe the long-lived component of ^{1}(TT), $k_{^1(\text{TT})}$ must be relatively slow. These two requirements are contradictory. If k_{diss} is fast and $k_{^1(\text{TT})}$ is slow, then dissociation will be the dominant pathway. In other words dissociation will deplete the ^{1}(TT) population before it has a chance to slowly decay with the rate constant $k_{^1(\text{TT})}$, so the long-lived portion of ^{1}(TT) is not observed. But if k_{diss} is slow enough that we do get a significant portion of the $k_{^1(\text{TT})}$ decay pathway, rapid triplet production will not be observed. Given the higher magnitude of $[T_1]$, it is more favourable to fit this component well rather than ^{1}(TT), thus k_{diss} is fit as fast, and no long lived ^{1}(TT) population is observed. With the shape of ^{1}(TT) already sacrificed, $k_{^1(\text{TT})}$ is then also fit as fast to modulate the magnitude of the triplets. Thus although both pathways are used, and a significant portion of triplet pairs decay to the ground state, this decay is too fast, and no long lived ^{1}(TT) is observed in the kinetic fit. Ultimately, this model is able to account for the loss of SF quantum yield or the low concentration of T_1 by including the ^{1}(TT) decay to ground state, but this is not sufficient to describe both the observed fast triplet formation and slow triplet pair decay.

5.2 Scheme 2

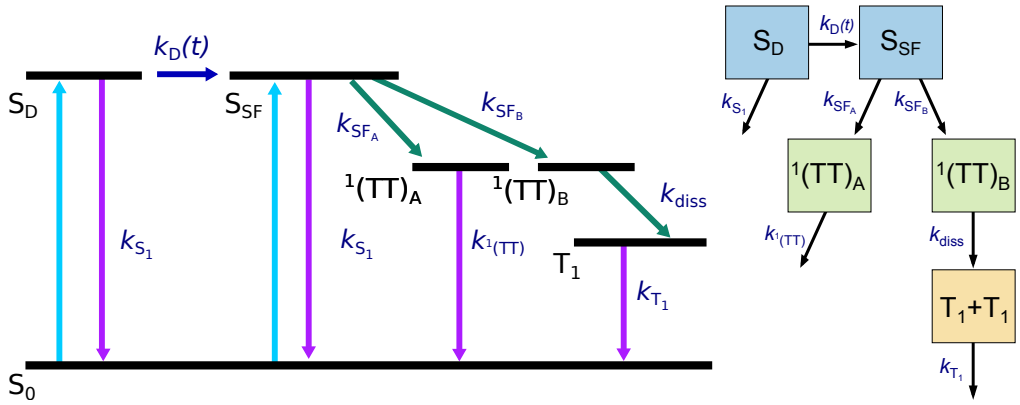

Figure 5.4: Kinetic Scheme 2. (a) Energy-level diagram. (b) Flow diagram

Given Scheme 1 was unable to describe all the observed behaviour for both the TA and time-resolved fluorescence, an alternative model was required. To account for the fast T_1 formation, but long-lived ^{1}(TT) population, the triplet pair was split into two subpopulations, $^1(\text{TT})_\text{A}$ and $^1(\text{TT})_\text{B}$, to give Scheme 2. This is represented in Figure 5.4, and by the system of differential equations below:

$$\frac{\text{d}[\text{S}_\text{D}]}{\text{d}t} = -k_{\text{S}_1}[\text{S}_\text{D}] - k_\text{D}(t)[\text{S}_\text{D}];$$
$$\frac{\text{d}[\text{S}_\text{SF}]}{\text{d}t} = k_\text{D}(t)[\text{S}_\text{D}] - (k_{\text{SF}_\text{A}} + k_{\text{SF}_\text{B}})[\text{S}_\text{SF}];$$

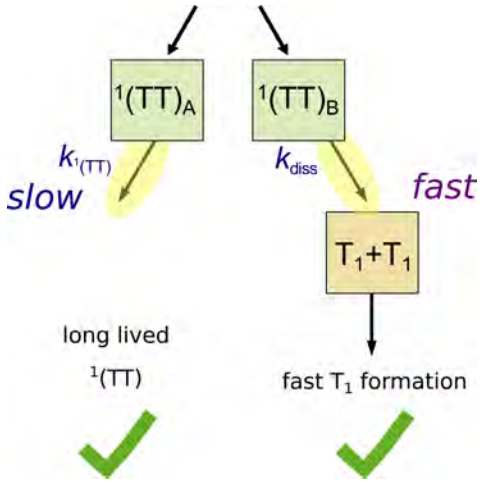

Figure 5.5: Treatment of $^1(TT)$ in Scheme 2. Splitting $^1(TT)$ into two subpopulations allows both rapid formation of T_1 and a long lived component of $^1(TT)$.

$$\begin{aligned}
\frac{d[^1(TT)_A]}{dt} &= k_{SF_A}[S_{SF}] - k_{^1(TT)}[^1(TT)_A];\\
\frac{d[^1(TT)_B]}{dt} &= k_{SF_B}[S_{SF}] - k_{diss}[^1(TT)_B];\\
\frac{d[T_1]}{dt} &= 2 \times k_{diss}[^1(TT)_B] - k_{T_1}[T_1];
\end{aligned} \tag{5.4}$$

where

$$[S_1] = [S_D] + [S_{SF}],$$

and

$$[^1(TT)] = [^1(TT)_A] + [^1(TT)_B].$$

In this model S_{SF} now undergoes SF to give either $^1(TT)_A$ with rate constant k_{SF_A} or $^1(TT)_B$ with rate constant k_{SF_B}. The $^1(TT)_B$ population is allowed to dissociate to give 2 separated triplets with rate constant k_{diss}, but $^1(TT)_A$ does not dissociate, and instead only decays to the ground state with rate constant $k_{^1(TT)}$. The rationale for this is explained in Figure 5.5. Whereas the single $^1(TT)$ population in Scheme 1 meant the fast T_1 formation could not be reconciled with slow $^1(TT)$ decay (Figure 5.3), two $^1(TT)$ populations isolates these decay pathways, making it possible for them to coexist. $^1(TT)_B$ can dissociate with a fast rate constant to give the rapid formation of T_1, without depleting all of the $^1(TT)$ population. $^1(TT)_A$ can then decay slowly, giving the long lived component of $^1(TT)$ observed in Chapter 4. Note that no delayed rise of either S_1 or T_1 was observed in the experiments, so this decay must be to the ground state rather than a slower dissociation to T_1, or recombination to give S_1. The proportion of decay versus dissociation is modulated by the rate constants k_{SF_A} and k_{SF_B}, rather than rates of dissociation and decay as in Scheme 1.

To reduce the complexity of fitting this model, k_{S_1} was taken to be 8.33×10^{-5} ps^{-1}, and k_{T_1} to be 6.67×10^{-5} ps^{-1}, as with Scheme 1. We again assumed the difference in rates of triplet pair formation comes from diffusion, and therefore constrained the *total* rate of singlet fission, $k_{SF} = k_{SF_A} + k_{SF_B}$, to be 0.256 ps^{-1} for every sample.

The fits of this model to the TA and time-resolved fluorescence are given in Figure 5.6, with fitted parameters in Table 5.2. The fits show a substantial improvement from Scheme 1, with consistently lower residuals. As expected, the long-lived $^1(TT)$

component is captured along with the rapid T_1 rise, and this is seen in all samples. For a few samples the decay of ^{1}(TT) is too fast, but is still significantly better than Scheme 1, validating the use of two ^{1}(TT) populations. The 1:0, 1:0.5 and 1:1 TIPS-Pn:PMMA samples in particular only show minor differences between the kinetically fitted and spectrally extracted concentrations, however the quality of the fits decreases somewhat from the 1:3 to 1:10 samples. The slow rise of the T_1 population is not observed in the experimental data, and for 1:7 and 1:10 the decay of S_1 is overestimated. This implies that, while the model is an improvement from Scheme 1, it fits too much diffusion at late times. Rather than k_D approaching zero and the decay of S_1 approaching the intrinsic singlet lifetime, singlets continue to diffuse and undergo SF, resulting in too much S_1 decay, and too much T_1 rise.

Table 5.2: Parameters from the fits of Scheme 2, with $k_{S_1} = 8.33 \times 10^{-5}$ ps^{-1}, $k_{T_1} = 6.67 \times 10^{-5}$ ps^{-1}, and $k_{SF_A} + k_{SF_B} = 0.256$. Note that no diffusion occurs for the 1:0 and 1:0.5 samples, so the values of a and b are arbitrary.

TIPS-Pn:PMMA	a (ps^{-1})	b (ps$^{-\frac{1}{2}}$)	k_{SF_A} (ps^{-1})	k_{SF_B} (ps^{-1})	k_{diss} (ps^{-1})	$k_{1(TT)}$ (10^{-3}ps^{-1})	$S_D(0)$ (10^{-7} M)	$S_{SF}(0)$ (10^{-7} M)	r_C (10^{-7} M)	r_A (10^{-3})
1:0	$1.6\times10^{7\dagger}$	$1.6\times10^{7\dagger}$	0.107	0.149	92.8	3.2	0.00	5.83	99	8.8
1:0.5	$1.5\times10^{8\dagger}$	$1.5\times10^{8\dagger}$	0.118	0.138	92.8	2.4	0.00	4.83	108	8.7
1:1	5.9	2.1×10^{1}	0.114	0.142	91.3	3.1	4.26	1.59	142	10.1
1:3	5.6×10^{-8}	9.6×10^{-2}	0.136	0.120	84.7	6.2	4.39	2.61	292	10.4
1:5	1.4×10^{-11}	4.0×10^{-2}	0.135	0.121	78.1	6.7	3.67	3.95	307	10.1
1:7	1.7×10^{-12}	4.0×10^{-2}	0.143	0.113	76.0	11.9	5.35	2.27	331	9.9
1:10	1.2×10^{-12}	4.7×10^{-2}	0.171	0.085	92.8	61.9	9.45	0.86	417	14.3

† Does not affect the quality of the fit and has no physical significance.

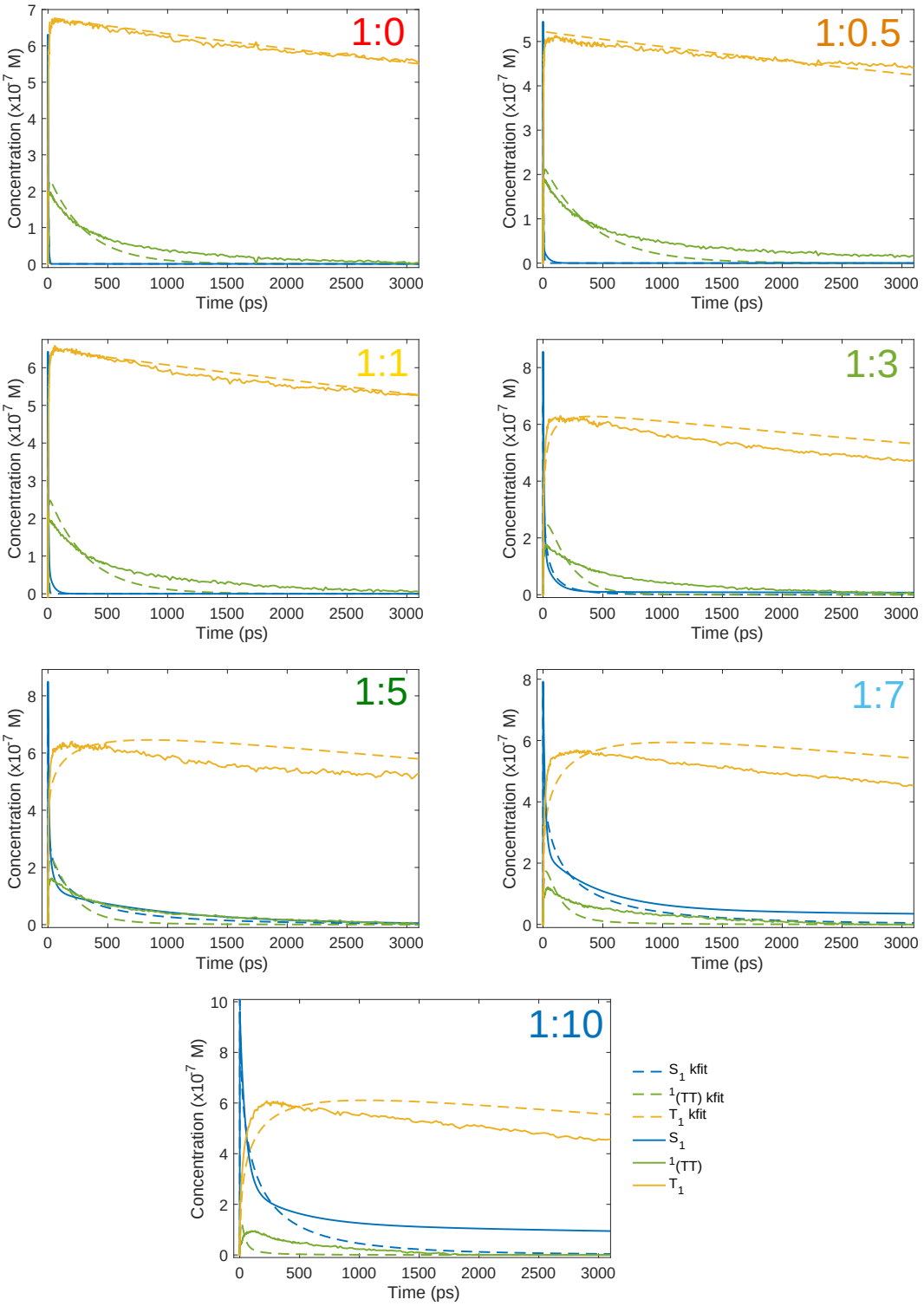

Figure 5.6: Fits of Scheme 2 to TIPS-Pn:PMMA nanoparticles. The kinetically fitted concentrations are plotted alongside the concentrations obtained from the spectral fits in Chapter 4.

5.2.1 Time-dependent Singlet-Fission Site Concentration

It is possible that diffusion given by the time-dependent Smoluchowski rate (Equation 5.2) is too fast at late times. The use of this rate relies on the assumption that the concentration of SF sites, c_{SF}, is much larger than the number of excitons in a NP, and can be treated as a constant. Given no power dependence is observed in the TA data this seems to be a fair assumption, but if the number of sites was small, diffusion to these sites would become slower as they become occupied, potentially accounting for the overestimation of S_1 decay in the fits in Figure 5.6. To test if this was the case we modified the rate of diffusion of S_D to S_{SF} to include a time-dependent concentration of SF sites, i.e.

$$k_{\mathrm{D}}(t) = 4\pi R D c_{\mathrm{SF}}(t)(1 + \frac{R}{\sqrt{\pi D t}}),$$

and parametrised this as

$$k_{\mathrm{D}}(t) = (1 - \frac{[\mathrm{S_{SF}}] + [^1(\mathrm{TT})_{\mathrm{A}}] + [^1(\mathrm{TT})_{\mathrm{B}}] + 0.5[\mathrm{T_1}]}{c_{\mathrm{SF_{max}}}})(a + bt^{-\frac{1}{2}}). \tag{5.5}$$

Then, as S_{SF}, $^1(TT)_A$, $^1(TT)_B$ and T_1 become populated, and the number of occupied SF sites approaches the maximum, $c_{\mathrm{SF_{max}}}$, k_D approaches zero faster than in Equation 5.2. To test if this improved the fit of Scheme 2, the 1:5 and 1:10 TIPS-Pn:PMMA samples were fit using Equation 5.5, now fitting $c_{\mathrm{SF_{max}}}$ in addition to the other parameters. The fits are given in Figure 5.7 and Table 5.3.

Table 5.3: Scheme 2 fits to 1:5 and 1:10 TIPS-Pn:PMMA samples with time-dependent $c_{\mathrm{SF}}(t)$. $k_{\mathrm{S_1}} = 8.33 \times 10^{-5}$ ps^{-1}, $k_{\mathrm{T_1}} = 6.67 \times 10^{-5}$ ps^{-1} and $k_{\mathrm{SF_A}} + k_{\mathrm{SF_B}} = 0.256$.

Ratio	$c_{\mathrm{SF_{max}}}$ (10^{-7} M)	a (ps^{-1})	b (ps$^{-\frac{1}{2}}$)	$k_{\mathrm{SF_A}}$ (ps^{-1})	$k_{\mathrm{SF_B}}$ (ps^{-1})	k_{diss} (ps^{-1})	$k_{^1(\mathrm{TT})}$ (ps^{-1})	$S_D(0)$ (10^{-7} M)	$S_{SF}(0)$ (10^{-7} M)	r_C (10^{-7} M)	r_A (10^{-3})
1:5	3.25×10^{7}	4.85×10^{-10}	0.056	0.158	0.098	92.8	0.027	4.41	4.65	281	12.6
1:10	2.71	3.78×10^{-9}	1.294	0.178	0.078	81.1	0.079	0.27	10.74	218	13.1

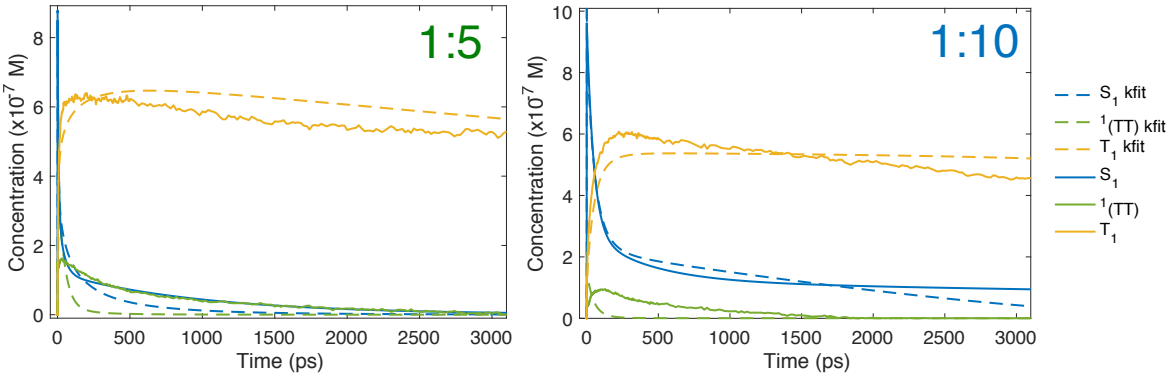

Figure 5.7: Fit of scheme 2 with time-dependent SF site concentration, $c_{\mathrm{SF}}(t)$, for 1:5 and 1:10 samples

The fitted value of $c_{\mathrm{SF_{max}}}$ for the 1:5 sample is significantly larger than the total concentration of excitons. Consequently c_{SF} is effectively constant and the fit is the same as in Table 5.2 and Figure 5.6. The residuals are improved for the 1:10 sample, but $c_{\mathrm{SF_{max}}}$ is now smaller than $S_{SF}(0)$, resulting in a negative diffusion rate. Constraining parameters to force a positive diffusion rate also did not improve the fit from Figure 5.6.

Since the fit of the 1:5 sample is the same as in Scheme 2, and the 1:10 sample is only improved for a negative diffusion rate, we conclude the inadequacies of Scheme 2 are not due to treating c_{SF} as a constant. Therefore, to fit the experimental data better an alternative model is needed.

5.3 Scheme 3

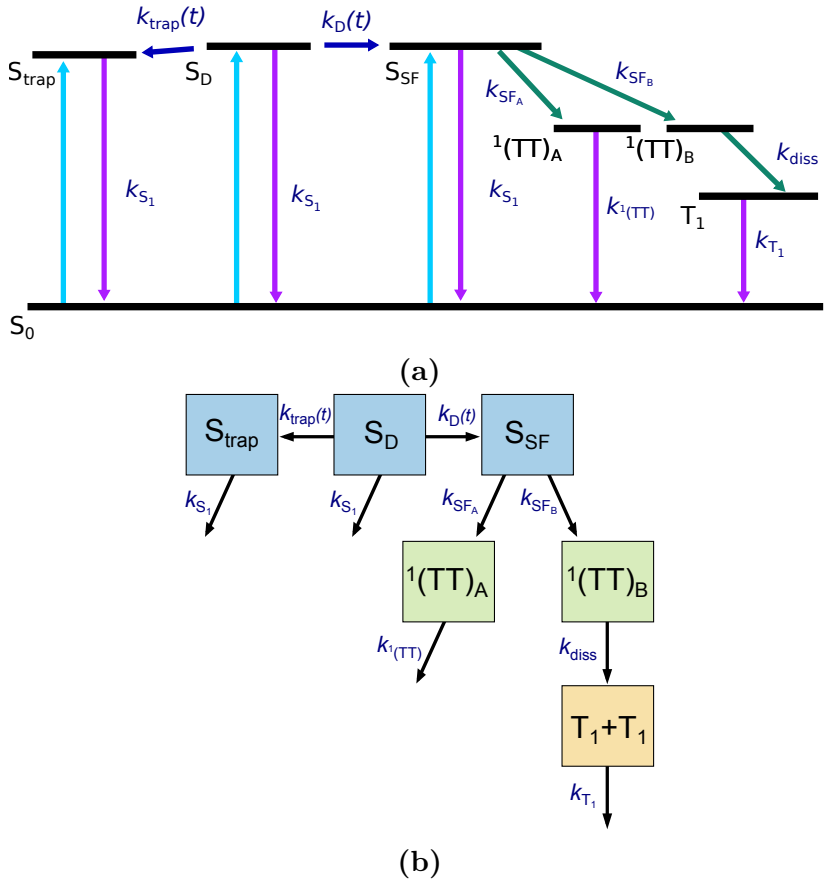

Figure 5.8: Kinetic Scheme 3 (a) Energy-level diagram. (b) Flow diagram

Scheme 2 gives too fast a decay of S_1 at late times, leading to a slow rise of T_1 that is not reflected in the experimental data. To understand this behaviour we refer back to the time-resolved fluorescence in Chapter 4. The fluorescence decay of each TIPS-Pn:PMMA ratio was fit with a combination of three time constants, one fast, τ_1, one of intermediate time, τ_2, and one slow, τ_3. As mentioned above, this implies that SF is diffusion limited, and splitting into two S_1 populations accounts for the rapid decay time, τ_1, and gives a distribution of intermediate decay times to account for τ_2. However, it is evident from Scheme 2 that diffusion is insufficient to explain the longest time component, τ_3. The presence of this component, and the fact that it fits well to the intrinsic 12 ns singlet lifetime for all samples, implies the existence of a population of singlet excitons that can neither undergo SF nor diffuse to eventually reach a site where they can. The only decay pathways available to this population are the intrinsic decay pathways to the ground state. In other words, the long-lived component of fluorescence that cannot be accounted for by diffusion must be due to the presence of singlet exciton trap sites.

In Scheme 3, we build on Scheme 2 by modelling singlet excitons located on trap sites as a third S_1 population such that

$$[S_1] = [S_D] + [S_{SF}] + [S_{trap}].$$

Once a singlet exciton diffuses into a trap site from S_D, or is excited into a trap site from the ground state, it is unable to diffuse away, and can only decay back to the ground-state with rate constant k_{S_1}. This model is represented in Figure 5.8 and can be expressed as a set of 6 coupled differential equations:

$$\begin{aligned}
\frac{d[S_D]}{dt} &= -k_{S_1}[S_D] - k_{trap}(t)[S_D] - k_D(t)[S_D];\\
\frac{d[S_{trap}]}{dt} &= -k_{S_1}[S_{trap}] + k_{trap}(t)[S_D];\\
\frac{d[S_{SF}]}{dt} &= -k_{S_1}[S_{SF}] + k_D(t)[S_D] - (k_{SF_A} + k_{SF_B})[S_{SF}];\\
\frac{d[^1(TT)_A]}{dt} &= k_{SF_A}[S_{SF}] - k_{1(TT)}[^1(TT)_A];\\
\frac{d[^1(TT)_B]}{dt} &= k_{SF_B}[S_{SF}] - k_{diss}[^1(TT)_B];\\
\frac{d[T_1]}{dt} &= 2 \times k_{diss}[^1(TT)_B] - k_T[T_1];
\end{aligned} \tag{5.6}$$

where $k_{trap}(t)$ is the rate of diffusion of S_D to trap sites, and all other rates are as previously defined. Assuming the number of traps sites is large compared with the number of excitons, $k_{trap}(t)$ is given by a Smoluchowski diffusion rate:

$$k_{trap}(t) = 4\pi R D c_{trap}\left(1 + \frac{R}{\sqrt{\pi D t}}\right), \tag{5.7}$$

where R and D are as defined previously, and c_{trap} is the total number of trap sites in a NP. $k_{SF}(t)$ is again given by Equation 5.2. To fit this model, we again took c_{SF} and c_{trap} as constant, but for Scheme 3 we forced additional constraints on these values. Assuming the trap sites and SF sites are randomly distributed in a NP,

$$\frac{\text{Total number of trap sites}}{\text{Total number of TIPS-Pn}} = \frac{\text{Number of initially excited trap sites}}{\text{Number of initially excited TIPS-Pn}},$$

i.e.

$$\begin{aligned}
\frac{c_{trap}}{c_{total}} &= \frac{S_{trap}(0)}{S_D(0) + 2 \times S_{SF}(0) + S_{trap}(0)},\\
c_{trap} &= \frac{S_{trap}(0) c_{total}}{S_D(0) + 2 \times S_{SF}(0) + S_{trap}(0)},
\end{aligned} \tag{5.8}$$

with the $2\times$ $S_{SF}(0)$ because a SF site is two TIPS-Pn molecules. Similarly

$$\frac{2 \times c_{SF}}{c_{total}} = \frac{2 \times S_{SF}(0)}{S_D(0) + 2 \times S_{SF}(0) + S_{trap}(0)},$$

therefore

$$c_{SF} = \frac{S_{SF}(0) c_{total}}{S_D(0) + 2 \times S_{SF}(0) + S_{trap}(0)}, \tag{5.9}$$

where c_{total} is the total concentration of TIPS-Pn in a NP, which was calculated in Chapter 2.

As with Scheme 2 we took k_{S_1} to be 8.33×10^{-5} ps^{-1}, k_{T_1} to be 6.67×10^{-5} ps^{-1} and $k_{SF_A} + k_{SF_B} = 0.256$ ps^{-1}. Then the only parameters we fit were R, D, $S_D(0)$, $S_{SF}(0)$, $S_{trap}(0)$, k_{SF_A}, k_{diss} and $k_{^1(TT)}$.

Initial fits to the data found that both R and D were not able to be fit independently. R could be fit to a range of values without affecting the residuals, as D could be varied to compensate, so the fitted values were not physically meaningful. To obtain meaningful values for D, R was fixed to 1.4 nm, which was obtained by relating the proportion of TIPS-Pn molecules in the NP that were SF sites ($2 \times c_{SF}/c_{\text{total}}$), to the probability that the separation between two molecules would be less than R. Details of this are given in Appendix 5.5.1.

Fitting the model with these constraints gives the concentrations in Figure 5.9 and parameters in Tables 5.4 and 5.5. The fits have around the same r_A values as in Scheme 2, but lower r_C values for most ratios. For the 1:1 sample r_C is slightly higher than in Scheme 2, as there is more discrepancy between the ^{1}(TT) and T_1 populations, however the fit of the singlet population is considerably improved. As explained in Chapter 2, the relative magnitudes of T_1 and ^{1}(TT) in the spectral fitting depend on the decay of T_1 estimated to extract the basis spectrum of ^{1}(TT). The difference in the maximum values of ^{1}(TT) and T_1 are within the error of this estimation, so we place less value on the respective magnitudes of T_1 and ^{1}(TT), and more on the ability of the model to capture the general shape, or lifetimes. Whereas for Scheme 2 the rise of T_1 was obviously delayed and the decay of S_1 overestimated at late times, for Scheme 3 the times are much more consistent. Significantly, the agreement of the fitted S_1 concentration with the spectrally extracted concentration taken from time-resolved fluorescence is much closer. As with Scheme 2, ^{1}(TT) shows less agreement between the fitted and spectrally extracted concentrations, but this is somewhat expected since, as explained in Chapter 4, the ^{1}(TT) spectrum contains artefacts from the change in shape of the T_1 spectrum. Hence the spectrally extracted concentration also contains these contributions. The fits are also still substantially better than Scheme 1.

Table 5.4: Fitted parameters of Scheme 3 to data with R=1.4 nm.

TIPS-Pn:PMMA	k_{SF_A} (ps^{-1})	k_{SF_B} (ps^{-1})	k_{diss} (ps^{-1})	$k_{^1(TT)}$ (10^{-3}ps^{-1})	$S_D(0)$ (%)	$S_{SF}(0)$ (%)	$S_{trap}(0)$ (%)	r_C (10^{-7}M)	r_A (10^{-3})	ϕ_{SF}	$\phi_{SF'}$
1:0	0.107	0.149	83.4	3.21	0.0	100.0	0.0	100	8.8	1.16	1.94
1:0.5	0.117	0.139	92.7	2.45	0.1	99.9	0.0	108	8.7	1.08	1.95
1:1	0.126	0.130	92.8	6.52	12.8	87.2	0.0	170	10.4	0.99	1.77
1:3	0.138	0.118	80.1	7.86	72.7	26.4	0.9	271	11.6	0.87	1.46
1:5	0.138	0.118	92.8	10.29	56.9	40.0	3.1	254	10.3	0.83	1.22
1:7	0.136	0.120	92.8	11.80	73.9	23.2	2.9	275	9.7	0.78	0.96
1:10	0.160	0.096	92.8	14.01	71.1	24.7	4.2	404	14.3	0.60	0.84

Given the quality of the fits is satisfactory, we can analyse the trends in the fitted parameters to explain the behaviour observed in Chapter 4. For the 1:0 and 1:0.5 samples the initial concentration of S_D is very close to 0, so for these samples little to no diffusion occurs. The value of D therefore has no physical relevance, that is, it could take any value and not impact the residuals, so this is omitted from Table 5.5. The average of D for the rest of the samples is $8\pm3\times10^{-5}$ cm^{2}s^{-1}, which is comparable

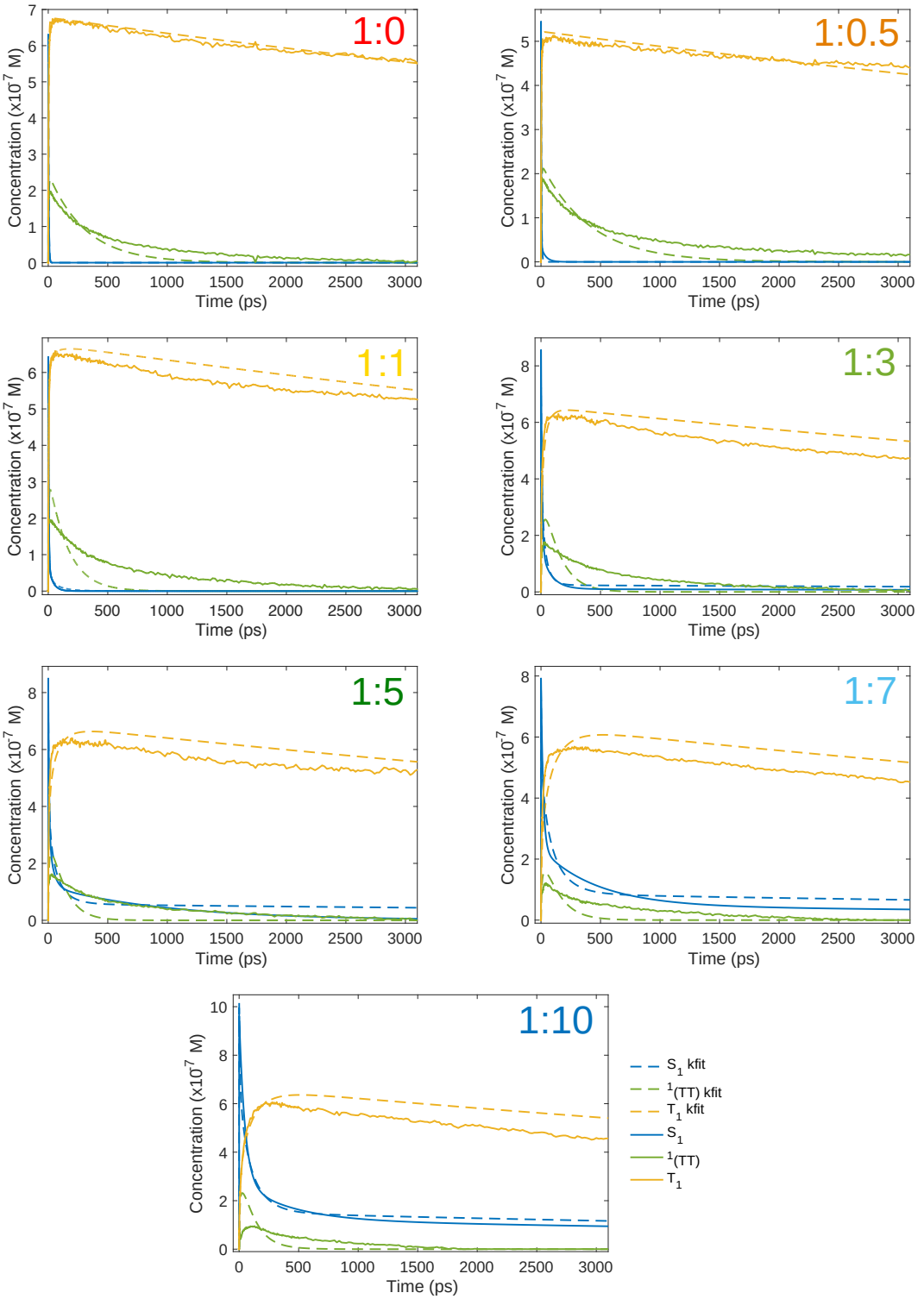

Figure 5.9: Fits of Scheme 3 to TIPS-Pn:PMMA nanoparticles with R=1.4 nm. The kinetically fitted concentrations are plotted alongside the concentrations obtained from the spectral fits in Chapter 4.

to the 1.5×10^{-5} cm^2s^{-1} diffusion constant observed in disordered films of diphenyl tetracence,[50] and the 5×10^{-4} cm^2s^{-1} diffusion constant in crystalline pentacene films.[38]

A summary of the fitted time constants is given in Figure 5.10. The rate constants of the first step of SF, k_{SF_A} and k_{SF_B} vary little between the different samples. On average

Table 5.5: Diffusion parameters from fits to Scheme 3 with R=1.4 nm, $k_{S_1} = 8.33 \times 10^{-5}$ ps^{-1}, $k_{T_1} = 6.67 \times 10^{-5}$ ps^{-1}, and $k_{SF_A} + k_{SF_B} = 0.256$.

TIPS-Pn:PMMA	D (cm^2 s^{-1})	c_{SF} (M)	c_{trap} (10^{-3} M)	c_{total} (M)
1:0	-†	0.864	0.00	1.73
1:0.5	-†	0.589	0.00	1.18
1:1	6.7×10^{-6}	0.417	0.00	0.90
1:3	1.2×10^{-4}	0.095	3.21	0.46
1:5	5.9×10^{-5}	0.087	6.72	0.31
1:7	9.4×10^{-5}	0.043	5.47	0.23
1:10	1.3×10^{-4}	0.033	5.67	0.17

† Does not affect the quality of the fit and has no physical significance.

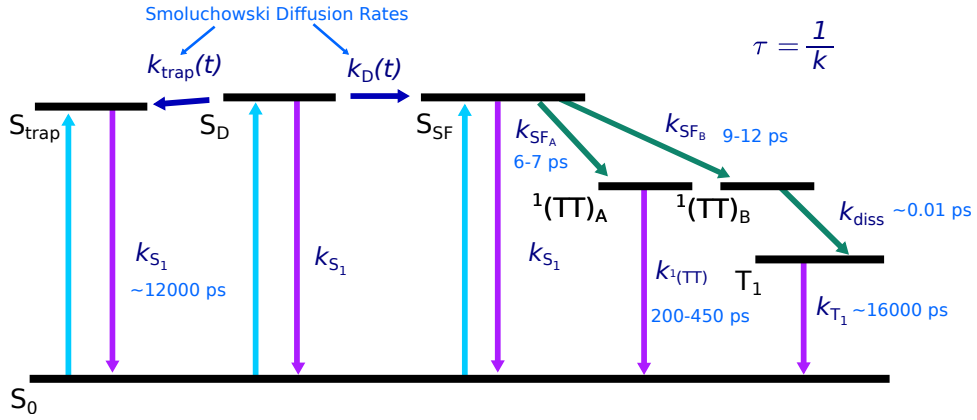

Figure 5.10: Summary of time constants fit using Scheme 3.

k_{SF_A} is the slightly faster rate constant of the two, averaging around 0.13±0.01 ps^{-1}, compared with 0.12±0.01 ps^{-1} for k_{SF_B}. This is equivalent to time constants of 7.6 ps and 8.1 ps respectively, and corresponds to approximately 52% of the S_{SF} population forming $^1(TT)_A$, and 48% $^1(TT)_B$. The prevalence of the $^1(TT)_A$ pathway accounts for the low quantum yields of SF observed in Chapter 4, as on average 52% of the singlet excitons that begin to undergo SF decay as a triplet pair intermediate instead of dissociating to give T_1. These rates are slower than what is generally observed in the literature for TIPS-Pn films and NPs, which can be rationalised by the disordered arrangement. SF sites might not be arranged as favourably as in crystalline form, such that though they are able to undergo SF, it is slower.

There is is a weak trend in the singlet fission rate constants as the average intermolecular separation is increased. k_{SF_A} becomes faster with increasing separation, and k_{SF_B} becomes slower, implying more SF to triplet pair intermediates that decay rather than dissociate. The proportion of decay through the $^1(TT)_A$ pathway increases from 42 to 62% as the average intermolecular separation increases. This implies that the formation of triplet pairs that do not dissociate is facilitated by larger intermolecular separations. Given we assume that the nature of SF sites does not change significantly with average intermolecular separation, we hypothesise that this is due to the neighbouring TIPS-Pn molecules of the SF sites being further away. A possible interpretation of this result is that $^1(TT)$ dissociation and T_1 formation is promoted by

hopping away from SF sites. Then, if $^1(TT)_B$ represents triplet pairs on SF sites that are close to neighbouring TIPS-Pn, hopping from these sites is easy and the triplet pair can dissociate. As intermolecular separation is increased, the number SF sites that are more isolated from their neighbours and do not dissociate, $^1(TT)_A$, will also increase, explaining the increase in k_{SF_A}. A similar conclusion was made in a study on intramolecular SF in covalently linked alkynyltetracene dimers.[60] This study also identified a $^1(TT)$ intermediate, and found that $^1(TT)$ decayed radiationlessly in isolated dimers. There are other plausible explanations for having two populations of triplet pair intermediates; for example there may be particular relative geometries of TIPS-Pn molecules that facilitate separation, and others that do not.

The rate constant of dissociation of $^1(TT)_B$, k_{diss} is practically the same for all samples (Table 5.4). This is relatively fast compared to the SF rates, with a time constant of only 0.01 ps. The first step of forming the triplet-pair intermediate thus appears to be the rate-limiting step in the formation of T_1. The rate constant for the decay of $^1(TT)_A$, $k_{^1(TT)}$, on the other hand, varies significantly between the samples. With the exception of 1:0 and 1:0.5, this appears to increase with average intermolecular separation. Why $^1(TT)_A$ would decay at different rates for different samples is unclear, but we note that in all cases that $k_{^1(TT)}$ is much smaller than k_{diss}, accounting for the the long-lived component of the triplet pair intermediate.

The fitted initial concentrations of each S_1 population are also given in Table 5.4, as a percentage of the total number of singlet excitons. The variation of $S_{trap}(0)$ is plotted against average intermolecular separation in Figure 5.11a and $S_{SF}(0)$ in Figure 5.11b.

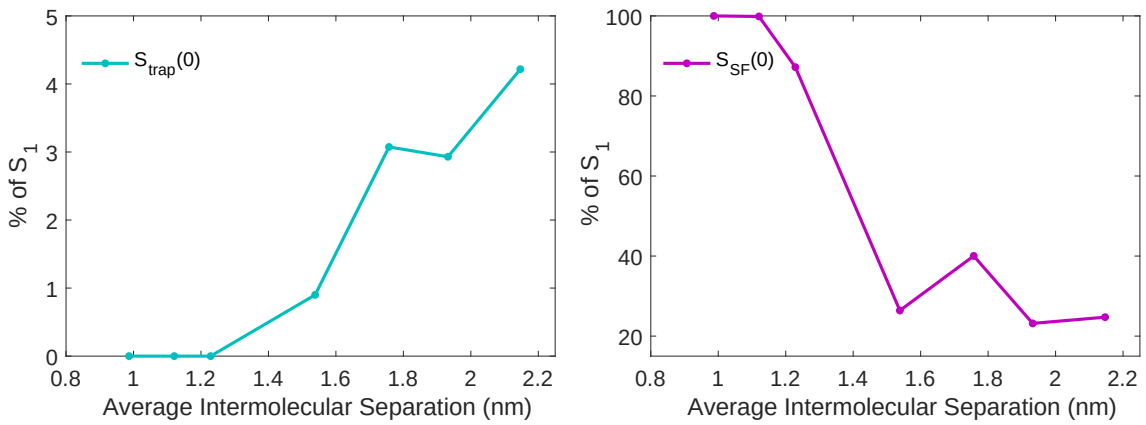

(a) **(b)**

Figure 5.11: Variation of the initial concentration of S_{trap} and S_{SF} with average intermolecular separation. The proportion of singlet excitons excited onto S_{trap} or S_{SF} represents the total proportion of TIPS-Pn molecules in the NP that are trap or SF sites (Equations 5.8 and 5.9).

Figure 5.11a shows the proportion of excitons initially excited onto singlet exciton trap sites increases with average intermolecular separation, indicating that the total number of trap sites in a NP, c_{trap}, also increases (Equation 5.8). This can be rationalised by considering the nature of trap sites. In crystalline morphologies, traps are generally caused by deformations or imperfections in the crystalline structure, but in amorphous systems such as the TIPS-Pn:PMMA NPs, a different interpretation is required. We propose that, in the NPs, traps are caused by a combination of geometry

and intermolecular separation. Certain TIPS-Pn molecules will have configurations leading to more stable S_1 states than others. Additionally, as the separation of these molecules from their neighbours increases, the likelihood for the exciton to hop away will decrease. Thus if a molecule is both stable and isolated, the chance that an exciton will hop away from it is low, and the molecule can be considered a trap site. As the average intermolecular separation is increased, the number of particularly isolated molecules would increase, and so more trap sites are observed.

The number of SF sites, on the other hand, decreases with average intermolecular separation (Figure 5.11b). The explanation for this trend is similar to trap sites: SF sites presumably need to consist of pairs of TIPS-Pn molecules that are relatively close together, and that have a specific orientation, but as the average intermolecular separation increases, less molecules have the necessary separation and so the total number of SF sites decreases.

Finally, we can use the fitted concentrations of S_1 and T_1 to determine a quantum yield of singlet fission, ϕ_{SF}, for each sample. These yields are given in Table 5.4 and plotted against the average intermolecular separation in Figure 5.12a.

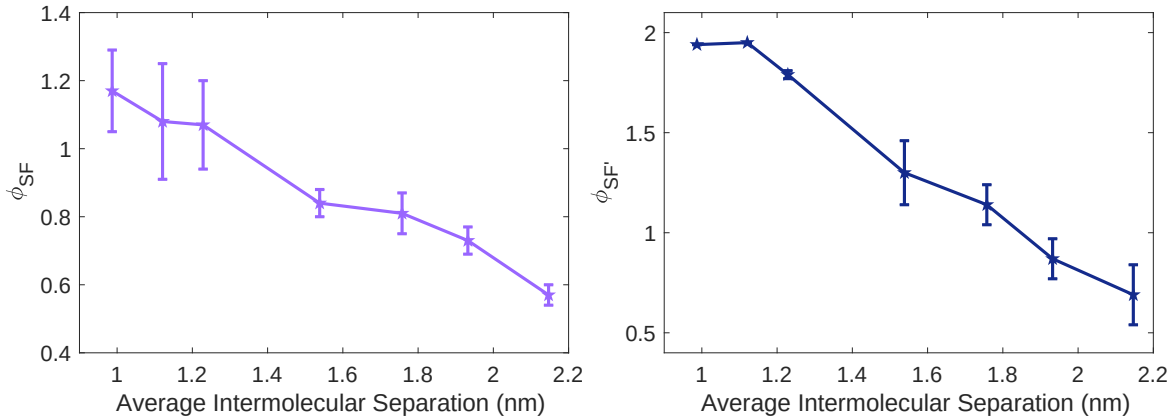

Figure 5.12: Variation of (a) quantum yield of SF, ϕ_{SF}, and (b) yield of the first step of SF, $\phi_{SF'}$, with average intermolecular TIPS-Pn separation. The upper and lower limits of the yields are given by assuming 27% and 0% decay of T_1 between 40 ps and 3 ns, respectively.

The quantum yields are fairly consistent with those determined in Chapter 4, mostly slightly higher due to the higher maximum T_1 and $^1(TT)$ concentrations fitted. The decrease in yields with average intermolecular separation can be explained by the proportions of trap sites and SF sites. As the average intermolecular separation increases, the number of trap sites increases, meaning more singlet excitons become trapped and therefore cannot undergo SF. At the same time, the number of SF sites decreases, so singlet excitons have to diffuse further before they can reach a SF site and undergo SF. This allows more time for competing processes, such as dissociation into trap states and decay of S_1, so less triplets formed, resulting in a lower ϕ_{SF}.

As observed in Chapter 4, even the highest yield, for the 1:0 sample, which we now know has no trap sites and comprises of entirely SF sites, is around 1 instead of 2. This can now be explained by the decay of the triplet pair intermediate, $^1(TT)_A$. Around 42% of singlets undergoing SF form $^1(TT)_A$, meaning only 58% actually form triplets. This gives a yield of $2 \times 0.58 = 1.16$, which is exactly what is observed. All

of the samples have between 42 and 62% of S_{SF} decaying through $^1(TT)_A$ instead of dissociating, so the yields for all the samples are significantly less than 2. To further illustrate this point, we calculated the modified SF quantum yield, $\phi_{SF'}$ as in Chapter 4 (Figure 5.12b). As this yield includes T_1 and $^1(TT)$, $\phi_{SF'}$ accounts for all of the S_1 population for the 1:0 sample, so the observed value is close to 2 (slightly below because some of $^1(TT)$ has already began to decay by the time it reaches a maximum). This means all singlets begin to undergo SF, but only a portion actually complete the process to dissociate to T_1. The trend of $\phi_{SF'}$ with intermolecular separation thus indicates the proportion of losses that are solely due to diffusion and trap sites.

All of the analysis so far in this chapter has been done by assuming 15% T_1 decay to extract the $^1(TT)$ basis spectrum. However as discussed in Chapter 2, this estimation affects the relative proportions of T_1 and $^1(TT)$, and therefore ϕ_{SF}. Therefore we also performed fits using the two extremes of the possibilities of T_1 decay to determine the $^1(TT)$ spectrum, 0% and 27%. The fits and fitting parameters for these are given in Section 5.5.2. The fits do not change substantially for the different decays, with the only significant difference being the proportions of k_{SF_A} and k_{SF_B}. For the 0% sample an average of 56% of the S_{SF} population leads to $^1(TT)_A$, compared with 48% for 27% decay. The increase for the 0% triplet decay is to be expected, as more of the spectra is attributed to $^1(TT)$, and hence the fitted concentration of $^1(TT)$ is higher and T_1 is lower. Given the amount of T_1 formed depends on the proportion of T_1 decay, the ϕ_{SF} in Figure 5.12 is shown as a range using the 27% decay as an upper bound, and 0% decay as a lower.

With respect to previous studies of TIPS-Pn that have reported SF quantum yields of around 2, it maybe the case that the failure of $^1(TT)$ to dissociate to T_1 is unique to our system (as it is more amorphous compared to previous), however previous studies have not made an attempt to identify and model $^1(TT)$ as was done here. Potentially this means that any $^1(TT)$ features present in the TA spectra were attributed to T_1, resulting in an overestimate of the amount of triplet produced. Essentially this would imply previous yields reported were $\phi_{SF'}$, rather ϕ_{SF}. A very recent study by Pensack and coworkers comparing crystalline and amorphous TIPS-Pn NPs reached the same conclusion for the amorphous NPs, finding the dissociation of $^1(TT)$ was frustrated in these, but did not observe this in the crystalline NPs.[86] In light of this result, the yields of TIPS-Pn in crystalline films are potentially not as low as for the NPs presented here, but it would nevertheless be interesting to re-examine the results of previous studies taking $^1(TT)$ into consideration, particularly for TIPS-Pn in solution.

5.3.1 Sensitivity of Results to Model Assumptions

The conclusions drawn from the fits of Scheme 3 are partially dependent on the validity of the assumptions made when fitting. For example, to extract the $^1(TT)$ and T_1 spectra we assumed that no $^1(TT)$ was present in the 1:0 sample at 3 ns, when the T_1 spectrum was extracted. However if this was not the case, the spectra of T_1 would be slightly different, and more of the T_1 shape would be attributed to $^1(TT)$. This could cause a decrease in the amount of T_1 observed, as well as causing it to decay less and rise slower. For example if the TA signal at 3 ns was 10% $^1(TT)$ and 90% T_1, the triplet basis spectra would be 10% lower at 505 nm, and $^1(TT)$ 10% higher. Taking this into account would decrease the lower bounds on ϕ_{SF}, but should not have an impact on $\phi_{SF'}$.

We also assumed that the 1:0 sample was not diffusion limited, and as such constrained k_{SF} to match the rate decay of the fluorescence for this sample. But previous studies of neat TIPS-Pn NPs did observe diffusion limited SF.[56] Whilst the morphology of our NPs is different, and the 1:0 fluorescence does not need to be fit with 2 exponentials, it might be a better physical representation of the system to still treat it as diffusion limited. If this was in fact the case, this would mean k_{SF} would fit much faster, which may improve the quality of the fits to the other samples.

Lastly, we have assumed $^1(TT)_A$ and $^1(TT)_B$ are different populations of the same species; that is, that the spectral identity of them is the same. However, the fits show $^1(TT)_B$ dissociates to form T_1 extremely rapidly, on the order of 0.01 ps, hence this population does not actually contribute to the TA spectra. The $^1(TT)$ component observed in the TA is only due to the $^1(TT)_A$ population, meaning that these two populations do not necessarily have to have the same spectrum, or in other words, actually be the same species. $^1(TT)_A$ could alternatively be described as some sort of trap state that is distinct from $^1(TT)$. For example, previous studies of SF have identified excimer trap states.[64,65] We can rule out the possibility of excimers in our case, since no emission is observed due to the decay of $^1(TT)_A$, but there may alternatively be some form non-emissive trap. On the other hand, a few other studies have also concluded that a large portion of the $^1(TT)$ state decays rather than dissociates, including a recent study of amorphous TIPS-Pn NPs.[60,73] The results of these studies support the conclusions made here.

Future work requires further testing the assumptions made in fitting these models, or trying to fit the data in their absence to account for the deficiencies of the model.

5.4 Conclusions

Out of the models studied here Scheme 3 gives the best fit to both the TA and time-resolved fluorescence of all the samples. Scheme 1, which assumed diffusion limited SF with a single $^1(TT)$ population, could not account for the long-lived component of $^1(TT)$. Scheme 2 improved this by assuming two $^1(TT)$ populations, but overestimated the diffusion of singlet excitons, and hence amounts of SF occurring at late times. Scheme 3 was able to account for both of these things by both splitting $^1(TT)$ into two sub-populations, and including the existence of singlet exciton traps.

Ultimately our results explain the observed decrease in the quantum yield of SF, by attributing losses to more diffusion and the greater presence of trap sites as average intermolecular separation is increased. Additionally, a major loss pathway across all average intermolecular separations is identified, due to the failure of over half of all formed triplet pair intermediates to dissociate into two separated triplets.

5.5 Appendices

5.5.1 Dependence of Scheme 3 on the Trapping Radius

It was initially found when fitting Scheme 3 that R and D could not be fit independently. To demonstrate this, Figure 5.13 and Tables 5.7 and 5.8 show the results of fitting Scheme 3 with both R and D unconstrained.

For 1:10, D is on the order of 10^{-4} cm^2s^{-1}, which is comparable to what is observed in similar systems,[50] however for 1:5 and 1:7 this is significantly lower, on the order of 10^{-9} cm^2s^{-1}. Similarly, R varies from 0.003 nm to 30 nm, with no apparent trend. These results are inconsistent with the assumption that the nature of SF sites does not change between the samples, as then the trapping radius should not change.

It appears that there is too much freedom in fitting the diffusion rates, and R and D are not independent parameters. As a result, R can be fit to a wide range of values without affecting the residuals or any of the other parameters, as D will just be varied to compensate. This means the fitted values of R and D lose their physical significance. To confirm this we refit the data fixing R to a few initial guesses, 0.5 nm, 1.0 nm, and 2.0 nm, as shown below. This resulted in fits of identical quality, and no significant difference between rates, confirming this is the case (Tables 5.9 to 5.14).

To obtain reasonable values for R and D one of the parameters had to be fixed. R can also be determined from the fitted values of c_{SF} and calculated values of c_{total} to give a "theoretical" trapping radius, R_t (see Chapter 2, Section 2.9.3). Briefly, we defined a SF site as a sphere of radius R, and solved for R by relating the probability of finding two TIPS-Pn molecules with that separation to the total proportion of SF sites, $2 \times c_{SF}/c_{total}$. Ideally, the fitted, or constrained value of R and the value determined from c_{SF}, R_t, should be identical.

The average R_t over the different samples for each of the fixed values of R are given in Table 5.6. Interestingly, R_t is very consistent between the different samples (average only has ∼7% error), and the average R_t identical between the different constrained values of R, with a value of 1.4±0.1 nm. This is a reasonable number for the trapping radius, as it is larger than the average intermolecular separation of the 1:0.5 NPs (1.1 nm), which is fit as comprising of mostly SF sites, but smaller than the separation in the 1:3 sample (1.5 nm), in which diffusion is more significant. We therefore proposed that 1.4 nm is a reasonable estimate for R, and fit the data using this value to obtain the corresponding D. Fixing R to 1.4 nm resulted in an identical R_t, as desired.

Table 5.6: Variation of diffusion constant D and the theoretical trapping radius R_t calculated using a Poisson distribution (Chapter 2, Section 2.9.3) with the value of R constrained for fitting. Note that since 1:0, 1:0.5 and 1:1 have no diffusion (i.e. all neighbouring TIPS-Pn molecules are SF sites), the parameters from these fits were excluded from the average.

Constrained R (nm)	Average Fitted D ($\times 10^{-5}$ cm^2 s^{-1})	Average Calculated R_t (nm)
0.5	51± 18	1.4 ± 0.1
1.0	19± 7	1.4 ± 0.1
2.0	4 ± 2	1.4 ± 0.1
1.4	8 ± 3	1.4 ± 0.1

5.5.1.1 Fits to Scheme 3 for various values of *R*

All fits used $k_{S_1} = 8.33 \times 10^{-5}$ ps^{-1}, $k_{T_1} = 6.67 \times 10^{-5}$ ps^{-1}, and $k_{SF_A} + k_{SF_B} = 0.256$.

Table 5.7: Fitted parameters to Scheme 3 with R unconstrained.

TIPS-Pn:PMMA	k_{SF_A} (ps^{-1})	k_{SF_B} (ps^{-1})	k_{diss} (ps^{-1})	$k_{1(TT)}$ (10^{-3}ps^{-1})	$S_D(0)$ (%)	$S_{SF}(0)$ (%)	$S_{trap}(0)$ (%)	r_C (10^{-7}M)	r_A (10^{-3})	ϕ_{SF}	$\phi_{SF'}$
1:0	0.107	0.149	83.4	3.21	0.0	100.0	0.0	100	8.8	1.16	1.94
1:0.5	0.117	0.139	92.7	2.45	0.1	99.9	0.0	108	8.7	1.08	1.95
1:1	0.116	0.140	92.8	3.54	10.3	89.1	0.6	133	9.7	1.07	1.78
1:3	0.145	0.111	92.8	14.39	89.1	10.7	0.2	276	12.4	0.83	1.35
1:5	0.143	0.113	92.8	15.48	64.0	34.0	2.0	252	10.9	0.79	1.17
1:7	0.149	0.107	92.8	24.27	83.8	14.8	1.4	214	9.5	0.71	0.87
1:10	0.160	0.096	92.8	39.54	92.8	6.1	1.1	229	11.6	0.61	0.62

Table 5.8: Fitted parameters to Scheme 3 with R unconstrained.

TIPS-Pn:PMMA	D (cm^2 s^{-1})	R (nm)	c_{SF} (M)	c_{trap} (M)	c_{total} (M)
1:0	-	-	0.864	0.00	*1.728*
1:0.5	-	-	0.589	0.00	*1.179*
1:1	1.5×10^{-2}	3.23×10^{-3}	0.422	2.81	*0.895*
1:3	5.8×10^{-8}	18.30	0.044	0.88	*0.456*
1:5	1.6×10^{-9}	25.47	0.078	4.51	*0.306*
1:7	3.4×10^{-9}	31.22	0.030	2.89	*0.230*
1:10	7.1×10^{-4}	1.42	0.010	1.69	*0.168*

Table 5.9: Fit parameters of Scheme 3 with R=0.5 nm.

TIPS-Pn:PMMA	k_{SF_A} (ps^{-1})	k_{SF_B} (ps^{-1})	k_{diss} (ps^{-1})	$k_{1(TT)}$ (10^{-3}ps^{-1})	$S_D(0)$ (%)	$S_{SF}(0)$ (%)	$S_{trap}(0)$ (%)	r_C (10^{-7} M)	r_A (10^{-3})	ϕ_{SF}	$\phi_{SF'}$
1:0	0.107	0.149	83.4	3.21	0.0	100.0	0.0	100	8.8	1.16	1.94
1:0.5	0.117	0.139	92.7	2.45	0.1	99.9	0.0	108	8.7	1.08	1.95
1:1	0.116	0.140	92.8	3.52	11.5	88.0	0.5	134	9.8	1.06	1.78
1:3	0.138	0.118	80.1	7.86	67.6	31.4	1.0	292	12.5	0.88	1.52
1:5	0.131	0.125	92.8	7.63	53.0	43.4	3.6	303	11.1	0.88	1.29
1:7	0.147	0.109	92.8	26.40	71.3	25.4	3.3	226	8.9	0.73	0.87
1:10	0.160	0.096	92.8	14.01	71.1	24.7	4.2	317	10.7	0.59	0.73

Table 5.10: Diffusion parameters from fits to Scheme 3 with R=0.5 nm.

TIPS-Pn:PMMA	D (cm^2 s^{-1})	c_{SF} (M)	c_{trap} ($\times10^{-3}$ M)	(c_{total} M)
1:0	-	0.864	0.00	*1.728*
1:0.5	-	0.589	0.00	*1.179*
1:1	5.4×10^{-5}	0.419	2.47	*0.895*
1:3	8.0×10^{-4}	0.109	3.58	*0.456*
1:5	3.6×10^{-4}	0.093	7.59	*0.306*
1:7	8.6×10^{-4}	0.047	6.08	*0.230*
1:10	4.7×10^{-4}	0.033	5.67	*0.168*

Table 5.11: Fit parameters of Scheme 3 with R=1.0 nm.

TIPS-Pn:PMMA	$k_{\mathrm{SF_A}}$ (ps^{-1})	$k_{\mathrm{SF_B}}$ (ps^{-1})	k_{diss} (ps^{-1})	$k_{1(\mathrm{TT})}$ ($\times 10^{-3}\mathrm{ps}^{-1}$)	$\mathrm{S_D}(0)$ (%)	$\mathrm{S_{SF}}(0)$ (%)	$\mathrm{S_{trap}}(0)$ (%)	r_C (10^{-7} M)	r_A (10^{-3})	ϕ_{SF}	$\phi_{\mathrm{SF'}}$
1:0	0.107	0.149	83.4	3.21	0.0	100.0	0.0	100	8.8	1.16	1.94
1:0.5	0.117	0.139	92.7	2.45	0.1	99.9	0.0	108	8.7	1.08	1.95
1:1	0.116	0.140	92.8	3.50	12.6	87.0	0.4	134	9.8	1.06	1.79
1:3	0.133	0.123	92.8	7.23	75.0	24.3	0.7	330	13.5	0.92	1.52
1:5	0.146	0.110	92.8	20.20	55.9	41.1	2.9	246	10.6	0.79	1.12
1:7	0.150	0.106	92.8	28.22	73.0	24.0	3.0	209	8.7	0.72	0.84
1:10	0.160	0.096	92.8	14.01	71.1	24.7	4.2	340	11.4	0.57	0.72

Table 5.12: Diffusion parameters from fits to Scheme 3 with R=1.0 nm.

TIPS-Pn:PMMA	D ($\mathrm{cm}^2\ \mathrm{s}^{-1}$)	$\mathrm{c_{SF}}$ (M)	c_{trap} (10^{-3} M)	c_{total} (M)
1:0	-	0.864	0.00	*1.728*
1:0.5	-	0.589	0.00	*1.179*
1:1	1.1×10^{-5}	0.416	2.08	*0.895*
1:3	3.1×10^{-4}	0.089	2.62	*0.456*
1:5	1.7×10^{-4}	0.089	6.33	*0.306*
1:7	3.1×10^{-4}	0.045	5.56	*0.230*
1:10	1.5×10^{-4}	0.033	5.67	*0.168*

Table 5.13: Fitted parameters of Scheme 3 with R=2.0 nm.

TIPS-Pn:PMMA	$k_{\mathrm{SF_A}}$ (ps^{-1})	$k_{\mathrm{SF_B}}$ (ps^{-1})	k_{diss} (ps^{-1})	$k_{1(\mathrm{TT})}$ ($\times 10^{-3}\mathrm{ps}^{-1}$)	$\mathrm{S_D}(0)$ (%)	$\mathrm{S_{SF}}(0)$ (%)	$\mathrm{S_{trap}}(0)$ (%)	r_C (10^{-7} M)	r_A (10^{-3})	ϕ_{SF}	$\phi_{\mathrm{SF'}}$
1:0	0.107	0.149	83.4	3.21	0.0	100.0	0.0	100	8.8	1.16	1.94
1:0.5	0.117	0.139	92.7	2.45	0.1	99.9	0.0	108	8.7	1.08	1.95
1:1	0.116	0.140	92.8	3.48	13.3	86.4	0.3	135	9.9	1.06	1.79
1:3	0.133	0.123	92.8	6.98	83.5	16.0	0.4	329	13.7	0.92	1.51
1:5	0.144	0.112	92.8	17.02	60.5	37.1	2.4	250	10.7	0.79	1.15
1:7	0.150	0.106	81.4	25.55	77.0	20.7	2.3	213	8.9	0.71	0.85
1:10	0.160	0.096	92.8	14.01	71.1	24.7	4.2	397	12.6	0.55	0.75

Table 5.14: Diffusion parameters from fits to Scheme 3 with R=2.0 nm.

TIPS-Pn:PMMA	(D $\mathrm{cm}^2\ \mathrm{s}^{-1}$)	$\mathrm{c_{SF}}$ (M)	c_{trap} (10^{-3} M)	c_{total} (M)
1:0	-	0.864	0.00	*1.728*
1:0.5	-	0.589	0.00	*1.179*
1:1	1.0×10^{-6}	0.415	1.62	*0.895*
1:3	1.0×10^{-4}	0.063	1.70	*0.456*
1:5	2.7×10^{-5}	0.083	5.32	*0.306*
1:7	6.3×10^{-5}	0.040	4.39	*0.230*
1:10	2.8×10^{-5}	0.033	5.67	*0.168*

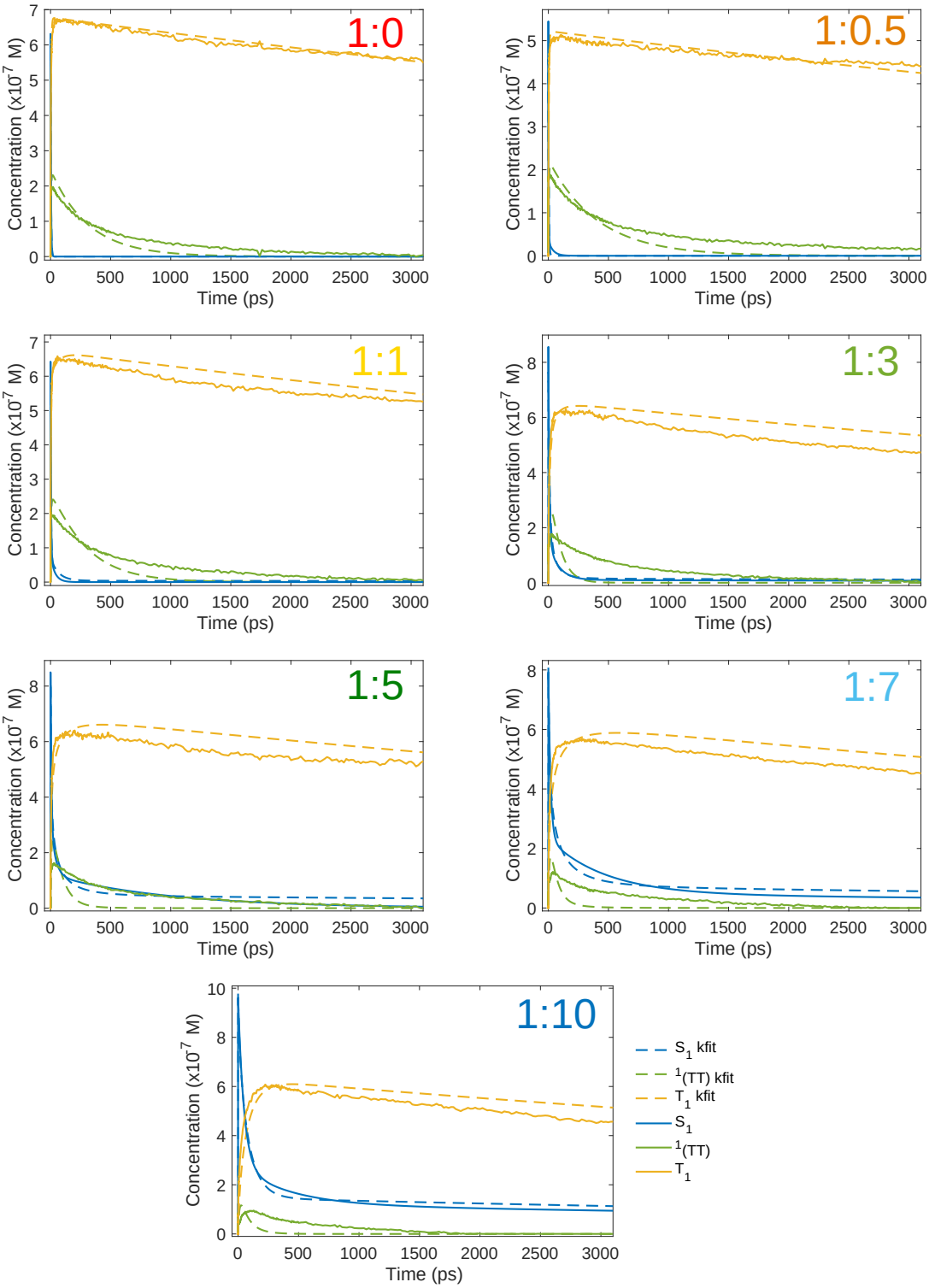

Figure 5.13: Fits of Scheme 3 to TIPS-Pn:PMMA nanoparticles with R unconstrained. The kinetically fitted concentrations are plotted alongside the concentrations obtained from the spectral fits in Chapter 4.

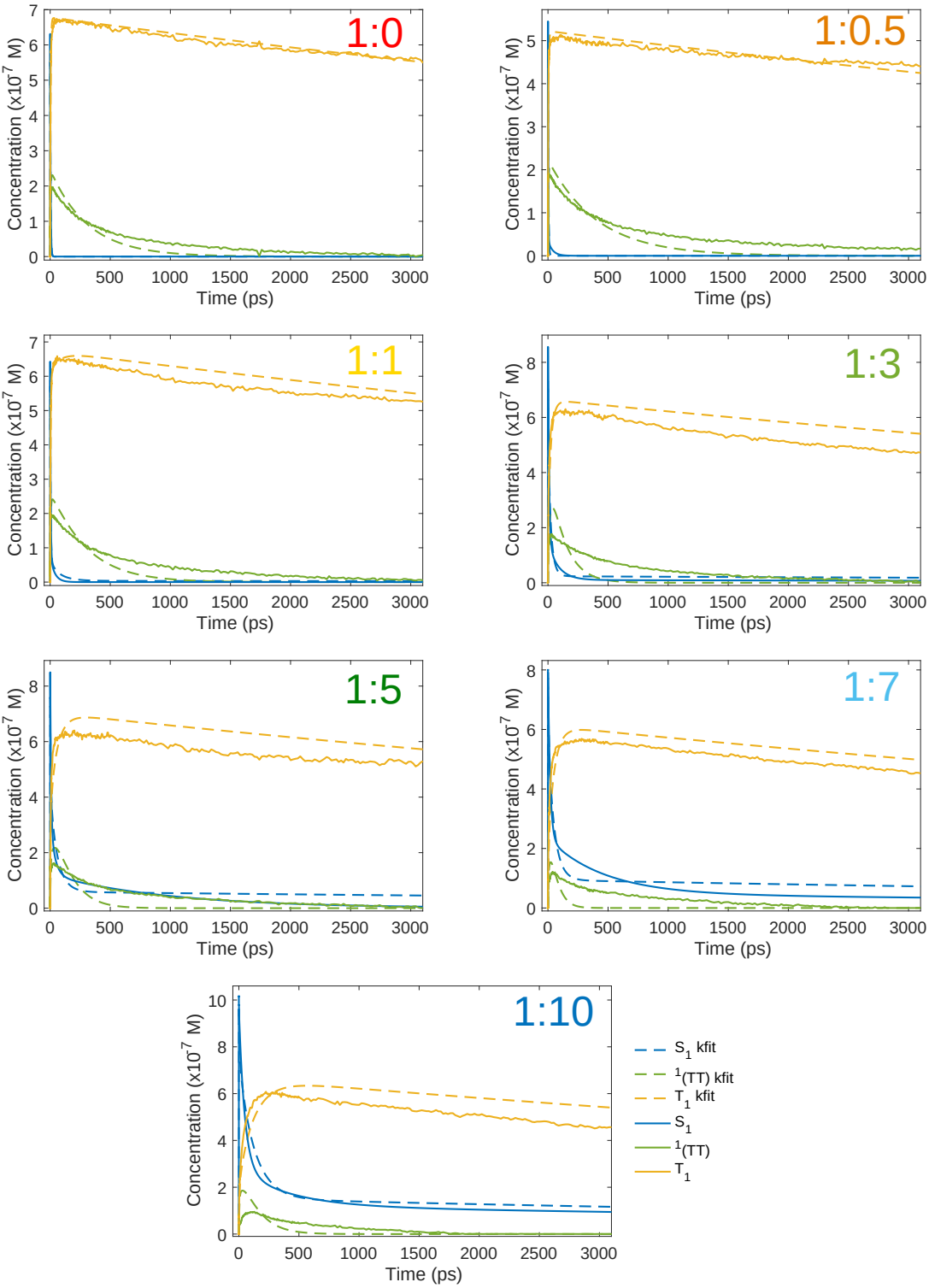

Figure 5.14: Fits of Scheme 3 to TIPS-Pn:PMMA nanoparticles with R=0.5 nm.

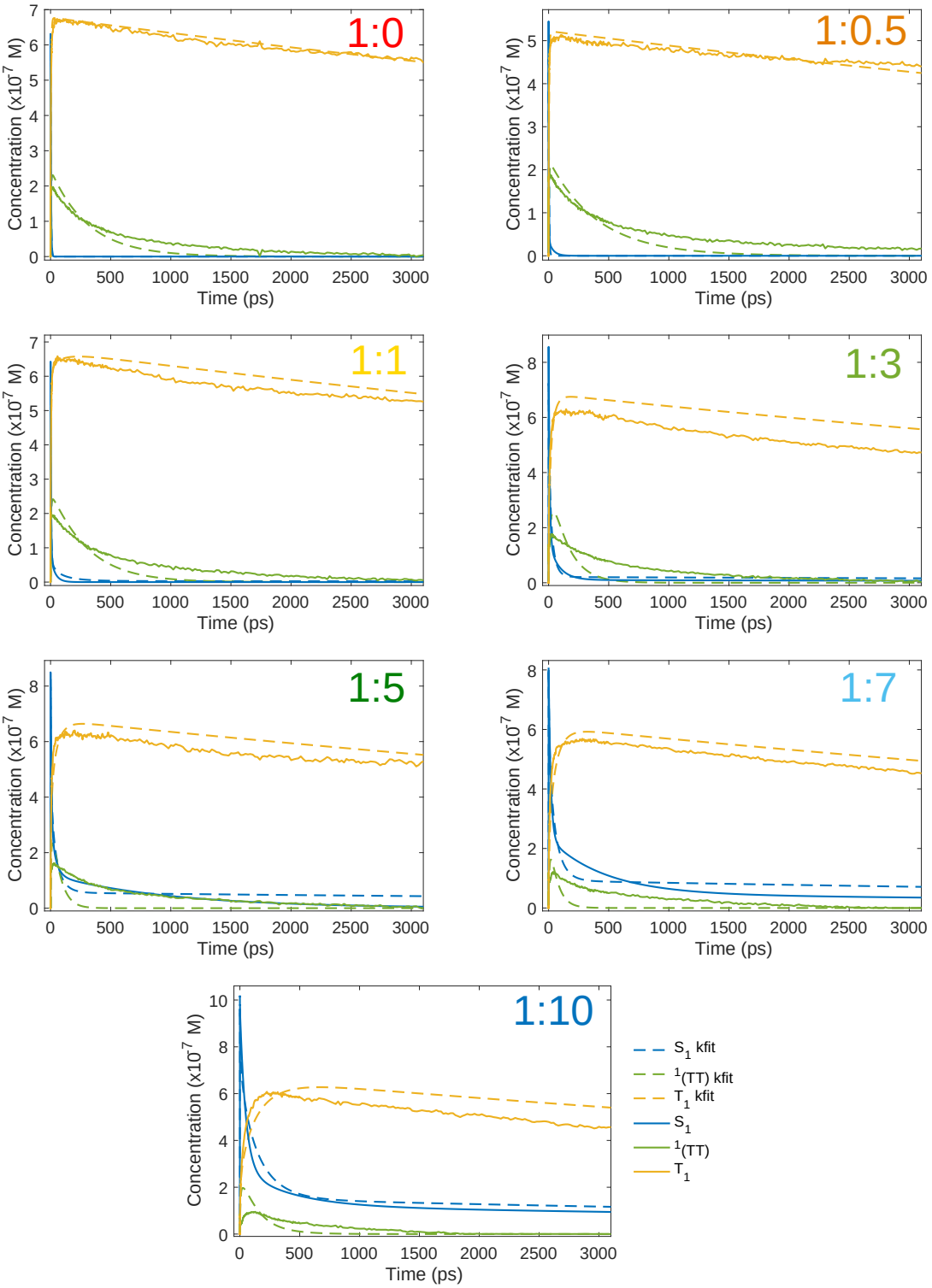

Figure 5.15: Fits of Scheme 3 to TIPS-Pn:PMMA nanoparticles with R=1.0 nm.

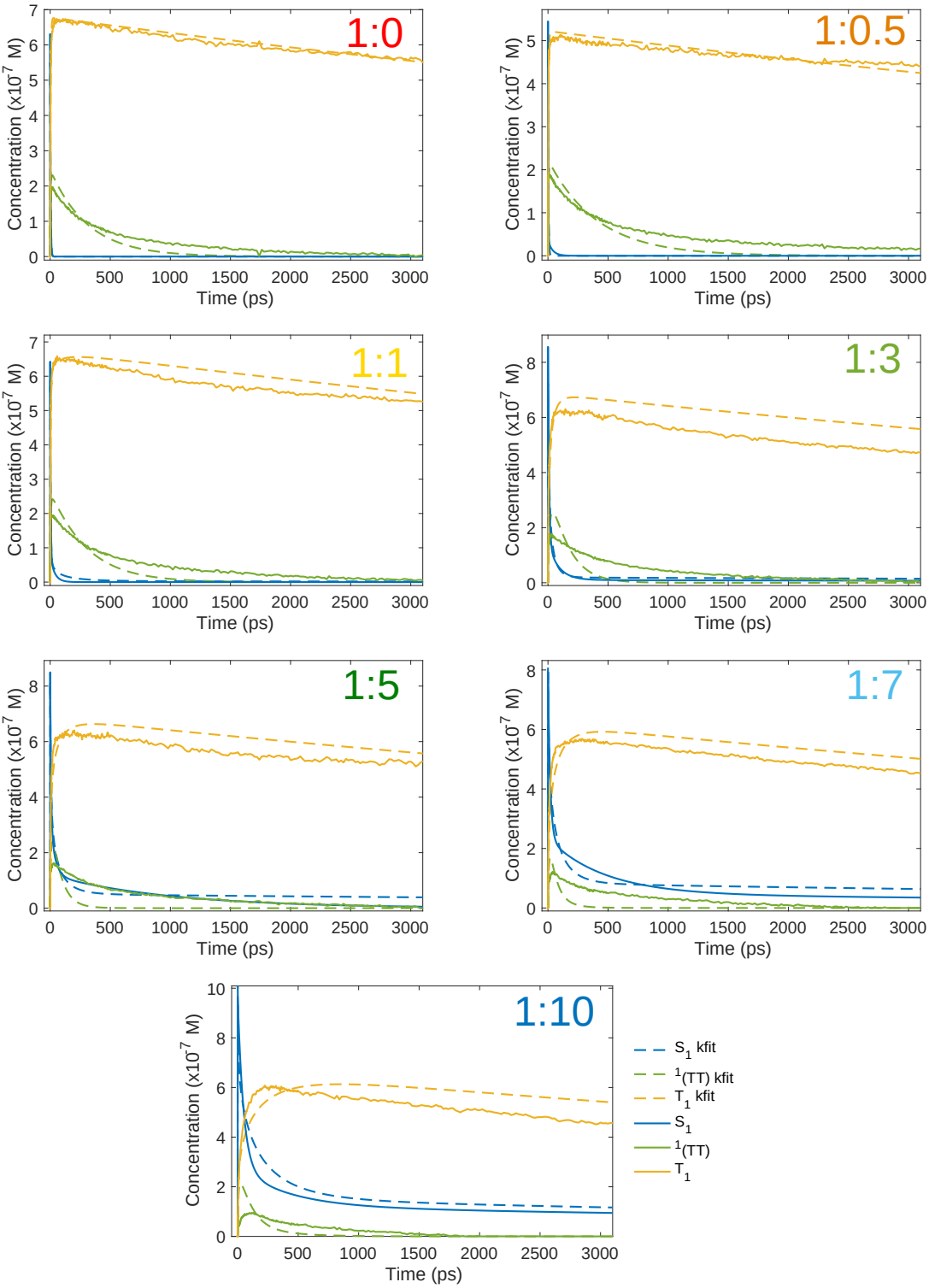

Figure 5.16: Fits of Scheme 3 to TIPS-Pn:PMMA nanoparticles with R=2.0 nm.

5.5.2 Scheme 3 Fits with R=1.4 nm assuming 0% and 27% triplet decay

All fits with $k_{S_1} = 8.33 \times 10^{-5}$ ps^{-1}, $k_{T_1} = 6.67 \times 10^{-5}$ ps^{-1}, and $k_{SF_A} + k_{SF_B} = 0.256$.

Table 5.15: Fitted parameters of Scheme 3 for 0% triplet decay between 40 ps and 3 ns.

TIPS-Pn:PMMA	k_{SF_A} (ps^{-1})	k_{SF_B} (ps^{-1})	k_{diss} (ps^{-1})	$k_{1(TT)}$ (10^{-3}ps^{-1})	$S_D(0)$ (%)	$S_{SF}(0)$ (%)	$S_{trap}(0)$ (%)	r_C (10^{-7}M)	r_A ($\times 10^{-3}$)	ϕ_{SF}	$\phi_{SF'}$
1:0	0.121	0.135	90.0	2.64	0.0	100.0	0.0	148	10.5	1.05	1.95
1:0.5	0.139	0.117	90.0	2.40	0.0	99.8	0.2	150	11.0	0.91	1.94
1:1	0.131	0.125	90.0	2.96	13.5	86.5	0.0	136	10.7	0.94	1.77
1:3	0.145	0.111	92.8	4.61	58.6	39.9	1.5	205	9.5	0.81	1.43
1:5	0.147	0.109	91.3	6.25	51.5	45.2	3.3	178	9.3	0.75	1.24
1:7	0.153	0.103	92.8	12.28	74.3	23.1	2.6	165	7.6	0.69	0.97
1:10	0.168	0.088	92.8	53.62	75.9	20.0	4.1	197	10.5	0.53	0.54

Table 5.16: Diffusion parameters for Scheme 3 fits with 0% triplet decay between 40 ps and 3 ns.

TIPS-Pn:PMMA	D (cm^2 s^{-1})	c_{SF} (M)	c_{trap} (10^{-3} M)	c_{total} (M)
1:0	-	0.864	0.00	*1.728*
1:0.5	-	0.589	0.96	*1.180*
1:1	2.2×10^{-6}	0.415	0.00	*0.895*
1:3	3.5×10^{-5}	0.130	4.73	*0.456*
1:5	3.2×10^{-5}	0.095	6.85	*0.306*
1:7	1.2×10^{-4}	0.043	4.83	*0.230*
1:10	1.6×10^{-4}	0.028	5.71	*0.168*

Table 5.17: Fitted parameters of Scheme 3 for 27% triplet decay between 40 ps and 3 ns.

TIPS-Pn:PMMA	k_{SF_A} (ps^{-1})	k_{SF_B} (ps$^{-\frac{1}{2}}$)	k_{diss} (ps^{-1})	$k_{1(TT)}$ (ps^{-1})	$S_D(0)$ (ps^{-1})	$S_{SF}(0)$ (10^{-3}ps^{-1})	$S_{trap}(0)$ (%)	r_C (%)	(%)	ϕ_{SF} (10^{-7} M)	$\phi_{SF'}$ (10^{-3})
1:0	0.091	0.165	92.8	4.03	0.0	100.0	0.0	201	10.1	1.29	1.94
1:0.5	0.095	0.161	92.8	2.71	0.0	99.4	0.6	189	9.5	1.25	1.94
1:1	0.097	0.159	92.8	4.33	11.7	86.7	1.5	272	12.5	1.20	1.81
1:3	0.139	0.117	92.8	40.14	78.6	20.9	0.5	413	15.5	0.88	1.14
1:5	0.134	0.122	92.8	36.26	62.2	35.1	2.7	397	15.3	0.87	1.04
1:7	0.143	0.113	92.8	49.69	77.7	19.9	2.5	331	12.6	0.76	0.77
1:10	0.161	0.095	74.6	307.53	71.1	24.7	4.2	283	13.8	0.58	0.58

Table 5.18: Diffusion parameters for Scheme 3 fit with 27% triplet decay between 40 ps and 3 ns.

TIPS-Pn:PMMA	D (cm^2 s^{-1})	c_{SF} (M)	c_{trap} (10^{-3} M)	c_{total} (M)
1:0	-	0.864	0.00	*1.728*
1:0.5	-	0.588	3.50	*1.180*
1:1	8.3×10^{-6}	0.416	7.32	*0.895*
1:3	2.4×10^{-4}	0.079	1.86	*0.456*
1:5	1.1×10^{-4}	0.079	6.20	*0.306*
1:7	2.1×10^{-4}	0.038	4.79	*0.230*
1:10	9.8×10^{-5}	0.033	5.67	*0.168*

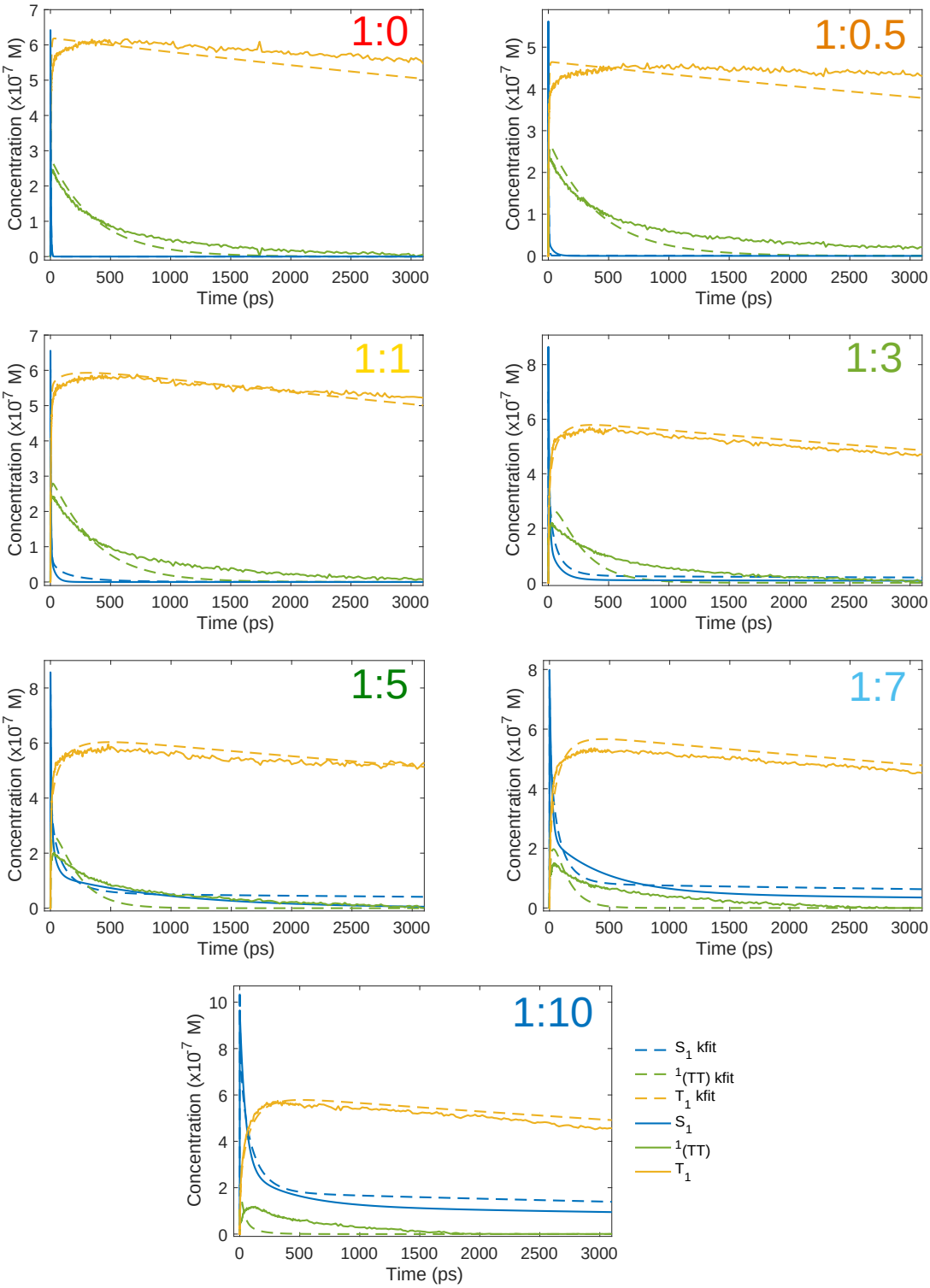

Figure 5.17: Fits of Scheme 3 to TIPS-Pn:PMMA nanoparticles with R=1.4 nm and 0% triplet decay.

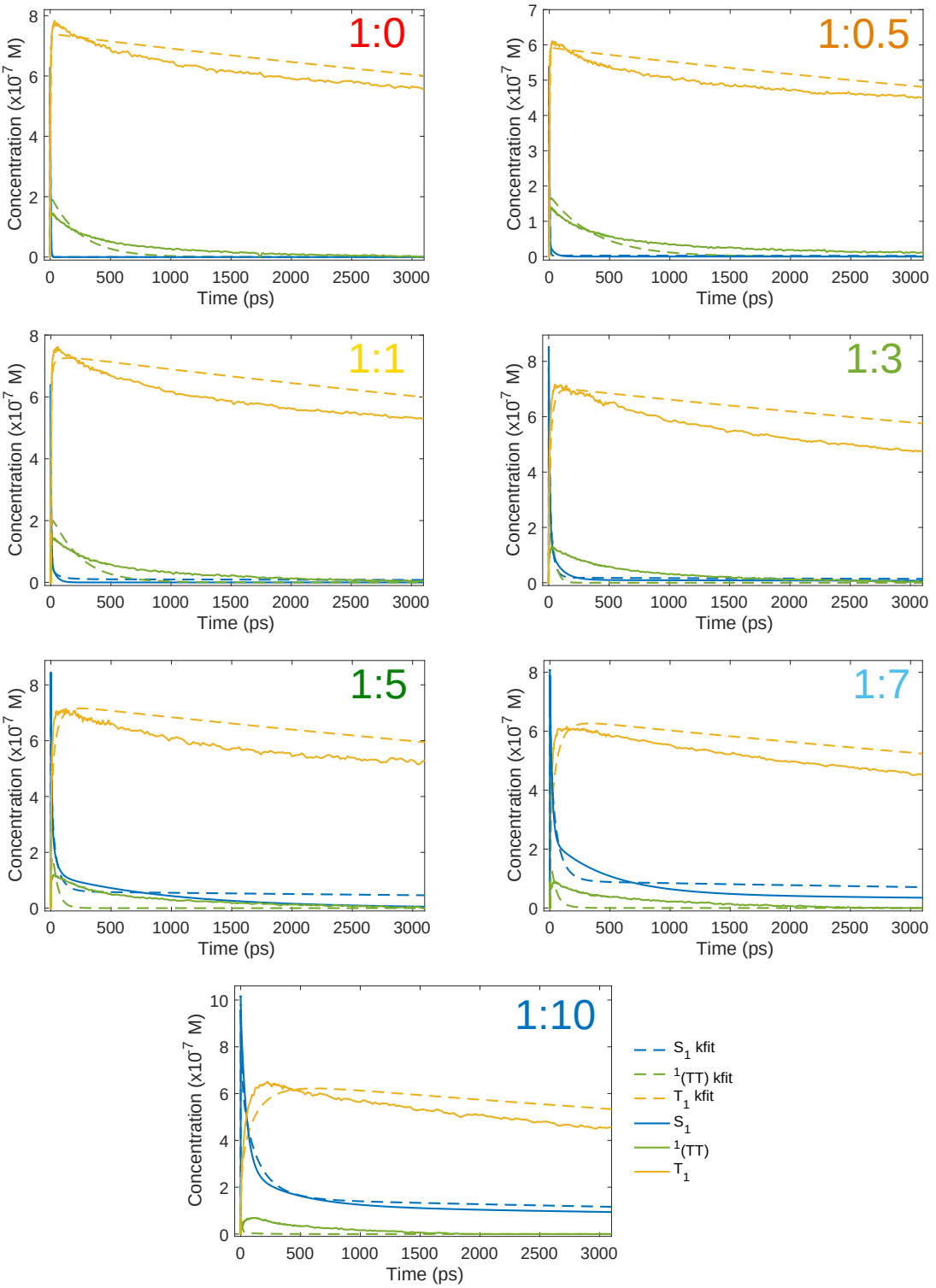

Figure 5.18: Fits of Scheme 3 to TIPS-Pn:PMMA nanoparticles with R=1.4 nm for 27% triplet decay.

CHAPTER 6
Conclusion

To investigate the effect of intermolecular distance on singlet fission (SF), aqueous dispersions of TIPS-Pn/PMMA nanoparticles (NPs) were prepared with various TIPS-Pn:PMMA mass ratios. In Chapter 3, the arrangement of TIPS-Pn in the NPs was shown to be random, with no formation of crystalline domains, indicating the average intermolecular separation increased with proportion of PMMA. Using the densities of TIPS-Pn and PMMA we estimated the average intermolecular separation varied from 0.99 nm for the neat (1:0) TIPS-Pn NPs to 2.15 nm for the 1:10 TIPS-Pn:PMMA sample.

In Chapter 4, time-resolved spectroscopy was used to show SF was present in all NPs to some extent. Time-resolved fluorescence demonstrated that the fluorescence lifetime, and hence the lifetime of the singlet excitons was significantly shorter than in dilute solution, due to the presence of SF. TA spectroscopy also showed the rise of a T_1 excited state absorption within 100 ps, indicative of triplet formation by SF. The rate of triplet formation was comparable with the fast rates of SF reported in the literature for TIPS-Pn, and appeared to decrease as intermolecular separation was increased.[39,53,56]

Significant overlap was present in the visible transient absorption spectra of TIPS-Pn, with features due to the ground state bleach, stimulated emission, and excited state absorption of three different species all occurring in the same regions. The complexity of the spectra meant to quantify the amount of SF occurring in each sample, the transient absorption had to be deconvoluted using a linear combination of the spectra of the constituent species. It was found that the transient absorption spectra could not be fit with two components, that is, with just the S_1 and T_1 excited states. The triplet pair intermediate, ^{1}(TT), also showed a spectral contribution, and therefore it must be included to reliably fit the data. SF quantum yields determined from three-component fits (S_1, T_1 and ^{1}(TT)) showed the yields decreased as intermolecular separation increased, and that all yields were considerably lower than what has previously been reported. Additionally the decay of the ^{1}(TT) population obtained from the three-component fit was not correlated with the rise of T_1; observations that were explained in the kinetic fitting in Chapter 5.

The final kinetic model proposed in Chapter 5 was able to fit both the transient absorption and time-resolved fluorescence. The observed trends were explained by splitting the S_1 population into three sub-populations to account for diffusion and the presence of exciton trap sites, and the triplet pair intermediate into two populations to account for both the slow decay of ^{1}(TT), but fast rise of T_1.

Similar to studies of amorphous substituted tetracene films, this model invoked diffusion-limited SF to explain the multi-exponential decay kinetics of the time-resolved fluorescence.[50] Only certain pairs of TIPS-Pn molecules in the NP would have had orientations and separations that were favourable for SF. SF from these "SF sites" was found to be rapid, with τ_{SF} ranging from 6 to 12 ps. Excitons generated elsewhere in the NPs had to diffuse to a SF site. Hence SF from these was delayed, leading to a

distribution of intermediate decay times. As the average intermolecular separation was increased, the number of TIPS-Pn molecules with a small enough separation to act as SF sites decreased, so the excitons had to diffuse further and the formation of triplets was slower.

The longer 12 ns component of the fluorescence decay that could not be described with diffusion was explained due to the presence of singlet-exciton traps. Molecules that were particularly isolated or more energetically stable than their surroundings trapped singlet excitons such that they were neither able to undergo singlet fission, nor diffuse to a SF site. The proportion of sites that were particularly isolated, and thus acted as traps, increased with average intermolecular separation, rationalising the increase in the amplitude of the 12 ns decay. An increase in both the number of trap sites and the amount of diffusion required to undergo SF led to a decrease in SF quantum yields with intermolecular separation.

Ultimately, it is apparent that the efficiency of SF is highest for the shortest intermolecular separations in amorphous NPs of TIPS-Pn. There did not appear to be any significant trends in the decay of T_1 or the rate of triplet-triplet annihilation, or at least not enough to affect the trends in the quantum yield of SF, as was originally hypothesised. However, the decay of the triplets occurred on a significantly longer time scale than the time window of the experiments studied here, so we cannot make any conclusions about the trends in TTA with confidence. It would be interesting to study these NPs over a larger time window, to determine if separation does have an effect on the triplet decay. However, ultimately any loss in efficiency due to the slow decay of T_1 will be negligible compared to the loss from the failure of ^{1}(TT) to dissociate into individual triplet pairs.

Approximately half of all ^{1}(TT) formed decayed to the ground state rather than dissociating. Thus, even in the 1:0 sample, in which there were no trap sites and SF was not diffusion limited, the quantum yield of singlet fission was 1 instead of the theoretical maximum of 2. The proportion of ^{1}(TT) that decayed decreased slightly with average intermolecular separation, suggesting the formation of triplets may be facilitated by the ability to hop away from the SF site, as has previously been suggested in studies of tetracene dimers.[60]

The loss of efficiency due to the decay of ^{1}(TT) is likely not unique to this system. As mentioned, the phenomena has also been observed in tetracene dimers,[60] and in an independent study on amorphous TIPS-Pn NPs.[73] Many spectroscopic studies on SF do not consider ^{1}(TT) in their analysis, so it is possible that what has previously been attributed to a triplet may in fact be a combination of the triplet and triplet pair, and SF may not be as efficient in these systems as initially thought. Future work could involve applying the method of analysis here to other systems, to determine if the same effect occurs. Tetracene in particular would be an insightful system to study, as SF in this system is endothermic and thus the reverse triplet-triplet annihilation reaction may play more of a role in the distance dependence than was observed here.

The findings in this study highlight the importance of careful analysis of transient absorption spectra, and also demonstrate that the rate of SF should not necessarily be equated with efficiency; here the rate of triplet production was fast, but the yield was still low.

Further investigation is needed to clarify the nature of the ^{1}(TT) intermediate and how it is formed. The involvement of an excimer-like state is unlikely, as no emission was observed after the decay of S_1. It may be possible to elucidate the role of charge-

transfer states by studying this system with a host polymer of different polarities. A polymer with a higher dielectric constant than PMMA, for example, could have the effect of stabilising any CT intermediates as has been documented for substituted pentacene dimers,[67] resulting in significantly different kinetics than what was observed here.

The substantial loss in efficiency due to ^{1}(TT) decay has significant implications for the application of SF in solar cells. Triplets are needed to generate charge, so if fewer triplets are produced, the efficiency of the solar cells will not approach the 45% limit that should be achievable for a single-junction solar cell with SF. Fortunately, the decay of ^{1}(TT) observed here was slow, so it may yet be possible to stimulate them into dissociating. It would also be interesting to use quantum-mechanical calculations to explore the geometry dependence of triplet-pair decay versus separation to T_1, and investigate whether the decay can be circumvented.

The TIPS-Pn/polymer NPs presented in this thesis are a useful system in which to study SF. Ultimately, fine control over the intermolecular separation, and by extension the kinetics of SF, was achieved, allowing insight into the efficiency of SF in TIPS-Pn. Unless a way to promote full ^{1}(TT) dissociation can be established, these NPs are not ideal for application in solar cells (though the ease of solution processing NP suspensions would have been beneficial). However, the system in this study can be modified in a number of ways, and there is potential to use the control demonstrated here to elucidate further aspects of mechanism of SF and competing processes.

References

[1] International Energy Agency, Key World Energy Statistics 2017. 2017; https://www.iea.org/publications/freepublications/publication/KeyWorld2017.pdf.

[2] Department of Industry Innovation and Science, Australian Energy Update 2016. 2016.

[3] Cook, J.; Nuccitelli, D.; Green, S. A.; Richardson, M.; Winkler, B.; Painting, R.; Way, R.; Jacobs, P.; Skuce, A. *Environ. Res. Lett.* **2013**, *8*, 024024.

[4] Cook, J. et al. *Environ. Res. Lett.* **2016**, *11*, 048002.

[5] Shafiee, S.; Topal, E. *Energy Policy* **2009**, *37*, 181–189.

[6] Grätzel, M. *Inorg. Chem.* **2005**, *44*, 6841–6851.

[7] Lewis, N. S. *Science* **2007**, *315*, 798–801.

[8] Kamat, P. V. *J. Phys. Chem. C* **2007**, *111*, 2834–2860.

[9] Perez, R.; Perez, M. *The International Energy Agency SHC Programme Solar Update* **2015**, *62*, 4–6.

[10] Jean, J.; Brown, P. R.; Jaffe, R. L.; Buonassisi, T.; Bulovic, V. *Energy Environ. Sci.* **2015**, *8*, 1200–1219.

[11] Shockley, W.; Queisser, H. J. *J. Appl. Phys.* **1961**, *32*, 510–519.

[12] Bremner, S. P.; Levy, M. Y.; Honsberg, C. B. *Prog. Photovoltaics Res. Appl.* **2008**, *16*, 225–233.

[13] Archer, M. D.; Bolton, J. R. *J. Phys. Chem.* **1990**, *94*, 8028–8036.

[14] Nozik, A.; Ellingson, R.; Micic, O.; Blackburn, J.; Yu, P.; Murphy, J.; Beard, M.; Rumbles, G. *Proc. 27th DOE Solar Photochem. Res. Conf.* **2004**, 63–66, Washginton, DC: US Dep. Energy.

[15] Tayebjee, M. J. Y.; Gray-Weale, A. A.; Schmidt, T. W. *J. Phys. Chem. Lett.* **2012**, *3*, 2749–2754.

[16] Tayebjee, M. J. Y.; McCamey, D. R.; Schmidt, T. W. *J. Phys. Chem. Lett.* **2015**, *6*, 2367–2378.

[17] Perlin, J. The Silicon Solar Cell Turns 50. 2004; https://www.nrel.gov/docs/fy04osti/33947.pdf.

[18] Green, M. A. *Prog. Photovoltaics Res. Appl.* **2009**, *17*, 183–189.

[19] National Renewable Energy Laboratory, Best Research-Cell Efficiencies. 2016; https://www.nrel.gov/pv/assets/images/efficiency-chart.png.

[20] Green, M. A. In *Third Generation Photovoltaics*; Kamiya, T., Venghaus, H., Monemar, B., Yamamoto, Y., Eds.; Springer, 2003.

[21] Smith, M.; Michl, J. *Chem. Rev.* **2010**, *110*, 6891–6936.

[22] Singh, S.; Jones, W. J.; Siebrand, W.; Stoicheff, B. P.; Schneider, W. G. *J. Chem.*

Phys. **1965**, *42*, 330–342.

[23] Parker, C. A. *Proc. Royal. Soc. A* **1963**, *276*, 125–135.

[24] Singh-Rachford, T. N.; Castellano, F. N. *Coord. Chem. Rev.* **2010**, *254*, 2560–2573.

[25] Trupke, T.; Green, M. A.; Würfel, P. *J. Appl. Phys.* **2002**, *92*, 4117–4122.

[26] Keivanidis, P.; Baluschev, S.; Miteva, T.; Nelles, G.; Scherf, U.; Yasuda, A.; Wegner, G. *Adv. Mater.* **2003**, *15*, 2095–2098.

[27] Schmidt, T. W.; Castellano, F. N. *J. Phys. Chem. Lett.* **2014**, *5*, 4062–4072.

[28] Gray, V.; Dzebo, D.; Abrahamsson, M.; Albinsson, B.; Moth-Poulsen, K. *Phys. Chem. Chem. Phys.* **2014**, *16*, 10345–10352.

[29] Smith, M. B.; Michl, J. *Annu. Rev. Phys. Chem.* **2013**, *64*, 361–386.

[30] Dexter, D. *J. Lumin.* **1979**, *18*, 779–784.

[31] Lee, J.; Jadhav, P.; Reusswig, P. D.; Yost, S. R.; Thompson, N. J.; Congreve, D. N.; Hontz, E.; Van Voorhis, T.; Baldo, M. A. *Acc. Chem. Res.* **2013**, *46*, 1300–1311.

[32] Jadhav, P. J.; Brown, P. R.; Thompson, N.; Wunsch, B.; Mohanty, A.; Yost, S. R.; Hontz, E.; Van Voorhis, T.; Bawendi, M. G.; Bulović, V.; Baldo, M. A. *Adv. Mater.* **2012**, *24*, 6169–6174.

[33] Hanna, M. C.; Nozik, A. J. *J. Appl. Phys.* **2006**, *100*, 074510.

[34] Pazos-Outón, L. M.; Lee, J. M.; Futscher, M. H.; Kirch, A.; Tabachnyk, M.; Friend, R. H.; Ehrler, B. *ACS Energy Lett.* **2017**, *2*, 476–480.

[35] Yang, L.; Tabachnyk, M.; Bayliss, S. L.; Böhm, M. L.; Broch, K.; Greenham, N. C.; Friend, R. H.; Ehrler, B. *Nano Lett.* **2015**, *15*, 354–358.

[36] Ehrler, B.; Walker, B. J.; Böhm, M. L.; Wilson, M. W. B.; Vaynzof, Y.; Friend, R. H.; Greenham, N. C. *Nat. Commun.* **2012**, *3*, 1019.

[37] Wilson, M. W. B.; Rao, A.; Ehrler, B.; Friend, R. H. *Acc. Chem. Res.* **2013**, *46*, 1330–1338.

[38] Marciniak, H.; Pugliesi, I.; Nickel, B.; Lochbrunner, S. *Phys. Rev. B* **2009**, *79*, 235318.

[39] Ramanan, C.; Smeigh, A. L.; Anthony, J. E.; Marks, T. J.; Wasielewski, M. R. *J. Am. Chem. Soc.* **2012**, *134*, 386–397.

[40] Burdett, J. J.; Müller, A. M.; Gosztola, D.; Bardeen, C. J. *J. Chem. Phys.* **2010**, *133*, 144506.

[41] Musser, A. J.; Liebel, M.; Schnedermann, C.; Wende, T.; Kehoe, T. B.; Rao, A.; Kukura, P. *Nat. Phys.* **2015**, *11*, 352–357.

[42] Wang, C.; Tauber, M. J. *J. Am. Chem. Soc.* **2010**, *132*, 13988–13991.

[43] Johnson, J. C.; Nozik, A. J.; Michl, J. *J. Am. Chem. Soc.* **2010**, *132*, 16302–16303.

[44] Eaton, S. W.; Shoer, L. E.; Karlen, S. D.; Dyar, S. M.; Margulies, E. A.; Veldkamp, B. S.; Ramanan, C.; Hartzler, D. A.; Savikhin, S.; Marks, T. J.;

Wasielewski, M. R. *J. Am. Chem. Soc.* **2013**, *135*, 14701–14712.

[45] Mauck, C. M.; Hartnett, P. E.; Wu, Y.-L.; Miller, C. E.; Marks, T. J.; Wasielewski, M. R. *Chem. Mater.* **2017**,

[46] Hartnett, P. E.; Margulies, E. A.; Mauck, C. M.; Miller, S. A.; Wu, Y.; Wu, Y.-L.; Marks, T. J.; Wasielewski, M. R. *J. Phys. Chem. B* **2016**, *120*, 1357–1366.

[47] Walker, B. J.; Musser, A. J.; Beljonne, D.; Friend, R. H. *Nat. Chem.* **2013**, *5*, 1019–1024.

[48] Wang, L.; Olivier, Y.; Prezhdo, O. V.; Beljonne, D. *J. Phys. Chem. Lett.* **2014**, *5*, 3345–3353.

[49] Renaud, N.; Sherratt, P. A.; Ratner, M. A. *J. Phys. Chem. Lett.* **2013**, *4*, 1065–1069.

[50] Roberts, S. T.; McAnally, R. E.; Mastron, J. N.; Webber, D. H.; Whited, M. T.; Brutchey, R. L.; Thompson, M. E.; Bradforth, S. E. *J. Am. Chem. Soc.* **2012**, *134*, 6388–6400.

[51] Mou, W.; Hattori, S.; Rajak, P.; Shimojo, F.; Nakano, A. *Appl. Phys. Lett.* **2013**, *102*, 173301.

[52] Sutton, C.; Tummala, N. R.; Beljonne, D.; Brédas, J.-L. *Chem. Mater.* **2017**, *29*, 2777–2787.

[53] Pensack, R. D.; Tilley, A. J.; Parkin, S. R.; Lee, T. S.; Payne, M. M.; Gao, D.; Jahnke, A. A.; Oblinsky, D. G.; Li, P.-F.; Anthony, J. E.; Seferos, D. S.; Scholes, G. D. *J. Am. Chem. Soc.* **2015**, *137*, 6790–6803.

[54] Yost, S. R. et al. *Nat. Chem.* **2014**, *6*, 492–497.

[55] Thorsmølle, V. K.; Averitt, R. D.; Demsar, J.; Smith, D. L.; Tretiak, S.; Martin, R. L.; Chi, X.; Crone, B. K.; Ramirez, A. P.; Taylor, A. J. *Phys. Rev. Lett.* **2009**, *102*, 017401.

[56] Tayebjee, M. J. Y.; Schwarz, K. N.; MacQueen, R. W.; Dvorak, M.; Lam, A. W. C.; Ghiggino, K. P.; McCamey, D. R.; Schmidt, T. W.; Conibeer, G. J. *J. Phys. Chem. C* **2016**, *120*, 157–165.

[57] Chan, W.-L.; Ligges, M.; Jailaubekov, A.; Kaake, L.; Miaja-Avila, L.; Zhu, X.-Y. *Science* **2011**, *334*, 1541–1545.

[58] Chan, W.-L.; Berkelbach, T. C.; Provorse, M. R.; Monahan, N. R.; Tritsch, J. R.; Hybertsen, M. S.; Reichman, D. R.; Gao, J.; Zhu, X.-Y. *Acc. Chem. Res.* **2013**, *46*, 1321–1329.

[59] Margulies, E. A.; Logsdon, J. L.; Miller, C. E.; Ma, L.; Simonoff, E.; Young, R. M.; Schatz, G. C.; Wasielewski, M. R. *J. Am. Chem. Soc.* **2017**, *139*, 663–671.

[60] Korovina, N. V.; Das, S.; Nett, Z.; Feng, X.; Joy, J.; Haiges, R.; Krylov, A. I.; Bradforth, S. E.; Thompson, M. E. *J. Am. Chem. Soc.* **2016**, *138*, 617–627.

[61] Stern, H. L.; Musser, A. J.; Gelinas, S.; Parkinson, P.; Herz, L. M.; Bruzek, M. J.; Anthony, J.; Friend, R. H.; Walker, B. J. *Proc. Natl. Acad. Sci. U.S.A.* **2015**, *112*, 7656–7661.

[62] Eaton, S. W.; Miller, S. A.; Margulies, E. A.; Shoer, L. E.; Schaller, R. D.; Wasielewski, M. R. *J. Phys. Chem. A* **2015**, *119*, 4151–4161.

[63] Ma, L.; Tan, K. J.; Jiang, H.; Kloc, C.; Michel-Beyerle, M.-E.; Gurzadyan, G. G. *J. Phys. Chem. A* **2014**, *118*, 838–843.

[64] Schrauben, J. N.; Ryerson, J. L.; Michl, J.; Johnson, J. C. *J. Am. Chem. Soc.* **2014**, *136*, 7363–7373.

[65] Liu, H.; Nichols, V. M.; Shen, L.; Jahansouz, S.; Chen, Y.; Hanson, K. M.; Bardeen, C. J.; Li, X. *Phys. Chem. Chem. Phys.* **2015**, *17*, 6523–6531.

[66] Monahan, N.; Zhu, X.-Y. *Annu. Rev. Phys. Chem.* **2015**, *66*, 601–618.

[67] Lukman, S.; Chen, K.; Hodgkiss, J. M.; Turban, D. H. P.; Hine, N. D. M.; Dong, S.; Wu, J.; Greenham, N. C.; Musser, A. J. *Nat. Commun.* **2016**, *7*, 13622.

[68] Johnson, J. C.; Nozik, A. J.; Michl, J. *Acc. Chem. Res.* **2013**, *46*, 1290–1299.

[69] Mastron, J. N.; Roberts, S. T.; McAnally, R. E.; Thompson, M. E.; Bradforth, S. E. *J. Phys. Chem. B* **2013**, *117*, 15519–15526.

[70] Fuemmeler, E. G.; Sanders, S. N.; Pun, A. B.; Kumarasamy, E.; Zeng, T.; Miyata, K.; Steigerwald, M. L.; Zhu, X.-Y.; Sfeir, M. Y.; Campos, L. M.; Ananth, N. *ACS Cent. Sci.* **2016**, *2*, 316–324.

[71] Zimmerman, P. M.; Zhang, Z.; Musgrave, C. B. *Nat. Chem.* **2010**, *2*, 648–652.

[72] Zimmerman, P. M.; Bell, F.; Casanova, D.; Head-Gordon, M. *J. Am. Chem. Soc.* **2011**, *133*, 19944–19952.

[73] Pensack, R. D.; Grieco, C.; Purdum, G. E.; Mazza, S. M.; Tilley, A. J.; Ostroumov, E. E.; Seferos, D. S.; Loo, Y.-L.; Asbury, J. B.; Anthony, J. E.; Scholes, G. D. *Mater. Horiz.* **2017**, *4*, 915–923.

[74] Wu, Y.; Liu, K.; Liu, H.; Zhang, Y.; Zhang, H.; Yao, J.; Fu, H. *J. Phys. Chem. Lett* **2014**, *5*, 3451–3455.

[75] Izadnia, S.; Schonleber, D. W.; Eisfeld, A.; Ruf, A.; LaForge, A. C.; Stienkemeier, F. *J. Phys. Chem. Lett* **2017**, *8*, 2068–2073.

[76] Kasai, H.; Nalwa, H. S.; Oikawa, H.; Okada, S.; Matsuda, H.; Minami, N.; Kakuta, A.; Ono, K.; Mukoh, A.; Nakanishi, H. *Jpn. J. Appl. Phys.* **1992**, *31*, L1132.

[77] Kasai, H.; Oikawa, H.; Okada, S.; Nakanishi, H. *Bull. Chem. Soc. Jpn.* **1998**, *71*, 2597–2601.

[78] Wu, C.; Szymanski, C.; McNeill, J. *Langmuir* **2006**, *22*, 2956–2960.

[79] Kurokawa, N.; Yoshikawa, H.; Hirota, N.; Hyodo, K.; Masuhara, H. *ChemPhysChem* **2004**, *5*, 1609–1615.

[80] Tuncel, D.; Demir, H. V. *Nanoscale* **2010**, *2*, 484–494.

[81] Clafton, S. N.; Beattie, D. A.; Mierczynska-Vasilev, A.; Acres, R. G.; Morgan, A. C.; Kee, T. W. *Langmuir* **2010**, *26*, 17785–17789.

[82] Wang, H.; Tao, X.; Newton, E. *Polym. Int.* **2004**, *53*, 20–26.

[83] Grieco, C.; Doucette, G. S.; Pensack, R. D.; Payne, M. M.; Rimshaw, A.; Scholes, G. D.; Anthony, J. E.; Asbury, J. B. *J. Am. Chem. Soc.* **2016**, *138*, 16069–16080.

[84] Sanders, S. N.; Kumarasamy, E.; Pun, A. B.; Trinh, M. T.; Choi, B.; Xia, J.; Taffet, E. J.; Low, J. Z.; Miller, J. R.; Roy, X.; Zhu, X.-Y.; Steigerwald, M. L.; Sfeir, M. Y.; Campos, L. M. *J. Am. Chem. Soc.* **2015**, *137*, 8965–8972.

[85] Sanders, S. N.; Kumarasamy, E.; Pun, A. B.; Appavoo, K.; Steigerwald, M. L.; Campos, L. M.; Sfeir, M. Y. *J. Am. Chem. Soc.* **2016**, *138*, 7289–7297.

[86] Pensack, R. D.; Ostroumov, E. E.; Tilley, A. J.; Mazza, S.; Grieco, C.; Thorley, K. J.; Asbury, J. B.; Seferos, D. S.; Anthony, J. E.; Scholes, G. D. *J. Phys. Chem. Lett.* **2016**, *7*, 2370–2375.

[87] Margulies, E. A.; Wu, Y.-L.; Gawel, P.; Miller, S. A.; Shoer, L. E.; Schaller, R. D.; Diederich, F.; Wasielewski, M. R. *Angew. Chem. Int. Ed.* **2015**, *54*, 8679–8683.

[88] Snellenburg, J. J.; Laptenok, S. P.; Seger, R.; Mullen, K. M.; van Stokkum, I. H. M. *J. Stat. Softw.* **2012**, *49*, 1–22.

[89] Zhang, Y.-D.; Wu, Y.; Xu, Y.; Wang, Q.; Liu, K.; Chen, J.-W.; Cao, J.-J.; Zhang, C.; Fu, H.; Zhang, H.-L. *J. Am. Chem. Soc.* **2016**, *138*, 6739–6745.

[90] Powell, R. C.; Soos, Z. G. *J. Lumin.* **1975**, *11*, 1–45.

[91] Chandrasekhar, S. *Rev. Mod. Phys.* **1943**, *15*, 1–89.

[92] Campillo, A.; Hyer, R.; Shapiro, S.; Swenberg, C. *Chem. Phys. Lett.* **1977**, *48*, 495–500.

[93] Marciniak, H.; Fiebig, M.; Huth, M.; Schiefer, S.; Nickel, B.; Selmaier, F.; Lochbrunner, S. *Phys. Rev. Lett.* **2007**, *99*, 176402.

[94] Fischer, D.; Naundorf, G.; Kloepffer, W. *Z. Naturforsch. Teil A* **1973**, *28*, 973–9.

[95] Kutta, M. W. *Z. Math. Phys.* **1901**, *46*, 435–453.

[96] Butcher, J. *Appl. Numer. Math.* **1996**, *20*, 247–260.

[97] Aragó, J.; Viruela, P. M.; Ortí, E.; Malavé Osuna, R.; Hernández, V.; López Navarrete, J. T.; Swartz, C. R.; Anthony, J. E. *Theor. Chem. Acc.* **2011**, *128*, 521–530.

[98] Abu-Sen, L.; Morrison, J. J.; Horn, A. B.; Yeates, S. G. *Adv. Opt. Mater.* **2014**, *2*, 636–640.

[99] Fudickar, W.; Linker, T. *J. Am. Chem. Soc.* **2012**, *134*, 15071–15082.

[100] Coppo, P.; Yeates, S. *Adv. Mater.* **2005**, *17*, 3001–3005.

[101] Andersson, P. O.; Gillbro, T. *J. Chem. Phys.* **1995**, *103*, 2509–2519.

[102] Gadermaier, C.; Cerullo, G.; Sansone, G.; Leising, G.; Scherf, U.; Lanzani, G. *Phys. Rev. Lett.* **2002**, *89*, 117402.

[103] Trinh, M. T.; Pinkard, A.; Pun, A. B.; Sanders, S. N.; Kumarasamy, E.; Sfeir, M. Y.; Campos, L. M.; Roy, X.; Zhu, X.-Y. *Sci. Adv.* **2017**, *3*.

[104] Stuart, A. N.; Tapping, P. C.; Kee, T. W.; Huang, D. M. **2017**, In preparation.